POLITECNICO DI TORINO

MASTER's Degree in AEROSPACE ENGINEERING

MASTER's Degree Thesis

Preliminary design of a total pressure acquisition system for a 10 kW scale ORC turbine: from numerical investigation of the flow field to integration within the ORCHID setup

Supervisors

Prof. Emanuele MARTELLI

Prof. Piero COLONNA

Dr. Matteo MAJER

Candidate

Alice MAIELLO

MARCH 2026

Preliminary design of a total pressure acquisition system for a 10 kW scale ORC turbine: from numerical investigation of the flow field to integration within the ORCHID setup

Alice Maiello

Abstract

In order to experimentally evaluate the performance of turbomachinery, accurate measurements of the flow properties downstream of the turbine rotor are necessary. A key indicator of the efficiency of such equipment is undoubtedly the total pressure, a parameter that is quite challenging to measure when dealing with non-uniform, swirling and potentially non-ideal flows.

The measurement of this quantity is intended to be performed on the radial inflow turbine of the TU Delft ORCHID facility, an experimental plant designed to study the performance of Organic Rankine Cycles (ORC). These thermodynamic cycles employ organic working fluids under non-ideal flow conditions and adopt radial inflow turbines for small-scale applications.

The aim of this work is to evaluate the technical feasibility for the integration of a total pressure measurement system within the ORCHID turbine by means of 3D numerical simulations. The analysis of the flow field downstream of the turbine wheel was carried out with a focus on the evolution and spatial distribution of flow properties such as the total pressure, the entropy, the Mach number, the flow angles and their spatial uniformity along the axial, radial and circumferential directions.

To ensure the validity and consistency of the results obtained, a mesh sensitivity study was carried out, while the suitability of the numerical setup was further analyzed by checking the effect of boundary conditions on the solution, and that of different interface models, such as the mixing plane and the frozen rotor interface.

The results show that non-uniformities in total pressure and entropy decay rapidly downstream of the rotor, at a rate that depends on the operating conditions.

These findings are taken as a guide for the probe selection and its orientation. Since the flow presents an uniform total pressure in the circumferential direction and an angle that varies along the radial direction, a pneumatic pressure probe with low sensitivity to flow direction is required. This solution was identified in a Kiel pressure probe.

Finally, the design of all components in the measurement system is proposed, in compliance with the technical and regulatory constraints of the facility.

Table of Contents

1 Introduction **1**

2 Background and Research Scope **3**

2.1 Organic Rankine Cycle Systems 3

2.2 Radial Inflow Turbines 6

2.3 The ORCHID Facility at TU Delft 7

2.4 Research Scope and Objectives 13

3 Methodology **14**

3.1 CFD Setup 14

3.1.1 Selection of the interface model 16

3.1.2 Simulation with Outlet Channel 22

3.2 Solution dependence to different outlet boundary models 27

3.3 Mesh Sensitivity Study 31

3.3.1 Richardson Extrapolation Method 31

3.3.2 Mesh Refinement 33

3.3.3 Results of the Mesh Sensitivity Study 33

4 Results **36**

4.1 Flow Non-Uniformity Analysis 36

4.1.1 Axial Non-Uniformity 37

4.1.2 Radial Non-Uniformity 38

4.2 Flow Angle Analysis 40

4.3 Off-Design Operating Points Analysis 41

4.3.1 CFD simulations of OP4, OP8 and OP12 42

4.3.2 Flow Angle Analysis for Off-Design Operating Points 44

5 Measurement System Design **47**

5.1 Description of the Measurement Section 47

5.2 Probe Selection 49

5.2.1 Remote Probes 49

5.2.2 Fast Response Aerodynamic Pressure Probes 52

5.2.3 Probe Selection Criteria 54

5.2.4 Selected Probe 57

5.3 Pressure Transducer 63

5.4 Traversing System 63
5.4.1 Traversing Requirements 65
5.4.2 Selected Design Solution 66
5.4.3 Traversing Strategy 74
5.5 Sealing System 80
5.5.1 Selected Sealing Solution 80
5.5.2 Integration of the sealing into the process connection 81

6 Conclusions and Outlook **83**
6.1 Limitations and Recommendations for Future Work 84
6.2 Outlook and Future Directions 85

A Fast-Response Aerodynamic Pressure Probes **87**
A.1 Introduction and Scope 87
A.2 Cylindrical Virtual-Mode FRAP (Politecnico di Milano) 88
A.2.1 Virtual Mode Operation: Phase-Locked Averaging and flow reconstruction 89
A.3 High-Temperature FRAP (ETH Zurich) 90
A.3.1 Virtual four-sensor (4VS) operating principle 91
A.4 Virtual Four Sensor FRAP (ETH Zurich) 92
A.5 Virtual Five Sensor FRAP (ETH Zurich) 93

B CFD Analysis of Kiel Probes in Non-Uniform Flow Conditions **95**
B.1 Motivation and Problem Definition 95
B.2 RANS Modeling of Kiel Probes 95
B.2.1 Geometrical Modeling and Mesh Requirements 95
B.2.2 Turbulence Modeling and Corrections 96
B.3 CFD Studies on Realistic Kiel Probe Geometries 97
B.4 Implications for the ORCHID Application and Future Work 97

C Traversing System: Alternative Solution **99**
C.1 Electric Motor and Servo-Drive 99
C.2 Motor-Driven Linear Slide Actuator 100

Bibliography **102**

Acknowledgments **108**

List of Figures

2.1 Comparison between Q–T diagrams of the evaporator of a ORC system and of the boiler of a steam power plant, assuming a heat source at 300°C. From Colonna et al. [3]. 4
2.2 Organic Rankine Cycle layout and thermodynamic cycle representation. From Colonna et al. [3]. 5
2.3 Balje $N_s - D_s$ efficiency chart for turbines. Adapted from [13] 8
2.4 CAD isomeric view of the ORCHID turbine test bed. Adapted from [15]. 10
2.5 Simplified flow diagram of the ORCHID facility, illustrating the closed-loop Organic Rankine Cycle followed by the working fluid. The main components include the pump, regenerator, evaporator, turbine test section, bypass line, and condenser. Adapted from [15]. 10
2.6 Meridional view of the ORCHID turbine stage and reference flow sections. Adapted from Majer [2]. 12
2.7 Three-dimensional view of the ORCHID radial inflow turbine developed at TU Delft. The turbine is designed for experimental investigations of high-temperature ORC systems. Image adapted from [2]. 12

3.1 Overall research workflow adopted in this work, highlighting the CFD-driven approach used to support the design of the experimental measurement system. 15
3.2 Convergence history of the frozen-rotor simulation during the initialization phase. 18
3.3 Comparison of entropy contours at the stator–rotor interface obtained using the mixing-plane and frozen-rotor approaches. The frozen-rotor solution preserves stator wake structures that are circumferentially averaged in the mixing-plane case. 19
3.4 Axial comparison of entropy contours obtained using the mixing-plane and frozen-rotor approaches. The frozen-rotor simulation highlights the downstream persistence of entropy wakes towards the outlet region. 20
3.5 Total pressure contours obtained from the frozen-rotor simulation. . 21
3.6 Mach number distribution obtained from the frozen-rotor simulation. 21
3.7 Static pressure field obtained from the frozen-rotor simulation. . . . 22

3.8 Computational domain including stator, rotor and extended cylindrical outlet channel. 23
3.9 Mach number contours on a constant-span plane for the frozen-rotor simulation including the outlet channel. The arrow points towards the rotor wakes. 24
3.10 The streamlines in the outlet channel highlights the strong residual swirl downstream of the rotor. The three-dimensional flow angle (α) is represented in a plane perpendicular to the axial direction. 25
3.11 Entropy contours on a constant-radius plane. The contours are referred to the local range considering only the outlet domain. 26
3.12 Total pressure contours on a constant-radius plane. The contours are referred to the local range considering only the outlet domain. 26
3.13 Flow field obtained with opening boundary condition at the outlet. The persistence and spatial extent of wakes and circumferential non-uniformities are comparable to the pressure outlet case. 28
3.14 Flow field obtained with elongated outlet channel. The persistence and spatial extent of wakes and circumferential non-uniformities are comparable to the pressure outlet case. 30
3.15 Radial profiles of total pressure at the candidate measurement section obtained with the coarse, medium, and fine meshes. 35

4.1 Axial non-uniformity analysis for total pressure at mid-radius. 37
4.2 Axial non-uniformity analysis for entropy at mid-radius. 37
4.3 Radial non-uniformity analysis for total pressure close to the rotor outlet. 38
4.4 Radial non-uniformity analysis for total pressure at the candidate measurement section. 39
4.5 Representation of pitch and yaw angles with respect to the probe axis and to the local reference planes of the cylindrical outlet channel. . . 40
4.6 Radial variation of pitch and yaw flow angles at the measurement section. 41
4.7 Outlet total pressure contours for operating points OP4, OP8, and OP12. 43
4.8 Axial and radial distributions of the total-pressure non-uniformity for OP7, OP4, OP8, and OP12. 45
4.9 Pitch and yaw angle distributions at the measurement section for OP4, OP8, and OP12. 46

5.1 Section view of the ORCHID turbine highlighting the rotor outlet measurement section diameter and location. Adapted from [2] . . . 47

5.2 Reduced temperature–entropy diagram of Siloxane MM showing expansion precesses A, B, C and D. The reduced temperature and entropy are defined as $T_r = T/T_{cr}$ and $s_r = s/s_{cr}$, where the reference condition is the vapor liquid critical point. The red dashed line indicates the critical isobar. Adapted from [2] 48
5.3 Yaw insensitivity range for various head geometries, showing the variation of total pressure error with flow angle. Adapted from [28]. 50
5.4 Total pressure decrease as a function of yaw angle for different probe geometries, highlighting the higher yaw insensitivity of Kiel probes. Adapted from [26]. 51
5.5 Magnitude of probe blockage effects as a function of Mach number and probe-to-duct diameter ratio d/D. For $M \approx 0.6$, acceptable losses are obtained for $d/D \lesssim 0.05$. Adapted from [27] 54
5.6 Effect of probe head diameter on wake resolution. When the probe diameter becomes comparable to the wake thickness, spatial averaging leads to a distortion of the measured wake profile. Adapted by [39] . 55
5.7 Radial distribution of the maximum total-pressure deviation from the mean at the candidate measurement section for OP8. The dashed line indicates the sensitivity threshold of a high-accuracy pressure sensor (35 Pa). 56
5.8 Technical drawing of the selected miniaturized Kiel probe [40], showing the probe head geometry and stem dimensions. 59
5.9 Absolute yaw angle seen by the probe after reorienting the probe head by approximately 9°. The flow angles remain well below the insensitivity limits of the Kiel probe over the entire radial range. . . 62
5.10 Effective yaw angle seen by the probe assuming a fixed orientation of 9° for OP4, OP8, and OP12. 62
5.11 Selected pressure transducer for total pressure measurements [41]. . 64
5.12 Effect of radial traversing step size on the reconstruction total pressure profiles at the test section. 65
5.13 Pneumatic linear actuator DGCI with integrated displacement encoder and recirculating ball bearing guide (numbers refer to the main functional components) [42]. 67
5.14 Proportional directional control valve VPWP (numbers refer to the main functional components) [42]. 69
5.15 Exemplary configuration of the CPX modular electrical terminal with integrated position controller [42]. 70
5.16 Overview of the pneumatic and electrical connections of the traversing system. Configuration with CompactRIO-based control architecture. 73
5.17 CAD integration of the pneumatic traversing system with the turbine test rig, showing the overall footprint. 74

5.18 Schematic representation of the multi-pass traversing strategy. Five traverses with a 5 mm step and 1 mm relative offset are interleaved to achieve an effective spatial resolution of 1 mm along the radial direction. 75
5.19 Hydraulic–electrical analogy for a pneumatic tubing system, where viscous losses in the tube are modeled as a series resistance and the transducer compliant volume as a capacitance. Adapted from [46]. . 78
5.20 Schematic cross-section of a Turcon® Varilip® PDR radial shaft seal [47]. 80
5.21 Exploded sectional view of the sealing assembly integrated into the process connection. 81

A.1 Cylindrical virtual-mode FRAP (CYL–2b) developed at the Politecnico di Milano. Drawing (left) adapted from [48] and picture (right) adapted from [49] 88
A.2 Calibration curves for the CYL–2b FRAP showing K_{yaw}, K_{P_T}, and K_{P_S} coefficients. Adapted from [36]. 90
A.3 High-temperature FRAP developed at ETH Zurich [34]. 91
A.4 FRAP-HT Virtual four-sensor operating strategy: rotation at 0°, +42° and −42° [34]. 91
A.5 a) pitch angle sensitive probe and b) yaw angle sensitive probe forming the Virtual Four Sensor (V4S) configuration developed at ETH Zurich [37]. 92
A.6 Single pressure transducer probe operating in Virtual Five-Sensor (V5S) mode developed at ETH Zurich. Adapted from [38]. 93
A.7 Interpolation procedure used to estimate the peak pressure from five angularly distributed measurements. Adapted from [38]. 93

B.1 Example of near-wall mesh refinement for a Kiel probe, adapted from [50]. 96
B.2 Mesh example for a Kiel probe head, adapted from [51]. 97

C.1 ATEX-certified electric motor Wittenstein MRSH064A-105 100
C.2 Schematic overview of the HepcoMotion PSD80 screw-driven linear actuator, highlighting the main components and integrated features [56]. 101

List of Tables

2.1 Main thermodynamic design parameters of the ORCHID turbine. . . 11
2.2 Main geometric parameters of the ORCHID turbine stage. 11

3.1 Summary of the mesh family adopted for the mesh sensitivity study. 33
3.2 Results of the Richardson extrapolation applied to the selected quantity of interest. 34

4.1 Operating points considered in the off-design analysis, following the nomenclature of Majer [2]. 41
4.2 Maximum axial non-uniformity at mid-span for each operating point expressed as a percentage. The nomenclature refers to Majer [2]. . . 42

5.1 Main specifications and coding of the selected pneumatic actuator DGCI-18-100-KF-QD-EX2 [42]. 68
5.2 Main specifications and coding of the selected proportional directional control valve VPWP-4-L-5-Q6-10-E-F-EX1 [42]. 70
5.3 Main specifications and coding of the selected controller configuration [42]. 71
5.4 Estimated time constant and dwell time of the pneumatic measurement chain for different assumed values of the transducer compliant volume. 79

Chapter 1

Introduction

Organic Rankine cycle (ORC) systems are a key technology for converting thermal energy from low- and medium-temperature sources (from 100°C to 600°C) into mechanical or electrical energy [1]. These systems find various applications in industry, a sector increasingly focused on reducing consumption and recovering energy. Some of these industrial applications are the thermal energy extraction and conversion from geothermal reservoirs, industrial waste heat, exhaust gases of engines and biomass combustion. The ORC concept is also applied to mobile engines such as those of long-haul trucks and vessels, which can become ultra-efficient when adopting mini-ORC for waste heat recovery [1, 2].

For small-capacity ORC plants (few kW up to tens MW [3]), radial inflow turbines are an ideal candidate for flow expansion. Despite axial turbines are more common and have been used in a plethora of applications and configurations, radial-inflow turbines (RITs) are a more compact and robust alternative for high expansion ratios within a single stage. Several studies on the design and efficiency of RITs have been carried out, such as those reported in [4, 5], and, more recently, the research also focused on small-scale RITs for ORC applications [6, 7]. However, the numerical modeling and experimental characterization of radial inflow turbines is still complex and partially unexplored.

This thesis was carried out in this context, within the ORCHID Facility (Organic Rankine Cycle Hybrid Integrated Device) at Delft University of Technology. This facility is an experimental test bench for analyzing the performance of small-scale radial inflow turbines dedicated to ORC cycles, with particular attention to the behavior of organic fluids used in them. In order to predict accurately the performance of this turbine, the flow downstream of the rotor needs to be further investigated, not only in terms of static quantities but also of total ones.

Since at this station the flow is potentially non-uniform, non-ideal and with a high residual swirl, measuring the total pressure could be inherently complex. Conventional probes could be significantly affected by the flow angle, local instability, or spatial gradients. For this reason, in order to design and integrate a measurement system, a detailed understanding of the outlet flow field through numerical analysis is first required.

In this work, this objective was achieved adopting a CFD-based approach, where numerical simulations are used to analyze the characteristics of the average flow with the aim of quantifying the persistence of non-uniformities, vortex and flow angle variations at the candidate measurement section. This targeted analysis provides the information needed to guide the design of a total pressure measurement system tailored to the ORCHID turbine.

In particular, it ensures that the selected probe, its positioning, orientation and movement are appropriate for the flow characteristics predicted by the numerical analysis and comply with the operational constraints imposed by the plant.

To better understand the workflow followed in this thesis, the main structure of the work is shown below:

- Chapter 2 introduces the background and research context, with an overview of what Organic Rankine Cycle systems are. In this chapter the ORCHID experimental facility is also presented.
- Chapter 3 explains the methodology adopted, presenting in detail the CFD analysis of the flow field downstream of the turbine rotor, with the steps taken to collect all the relevant flow features.
- Chapter 4 presents the post-processed results obtained from CFD analyses, giving information useful to guide the system design. It contains the analysis of flow non-uniformities, flow angles and off-design operating points.
- Chapter 5 describes the preliminary design of the pressure measurement system for the ORCHID turbine.
- Chapter 6 summarizes the main conclusions of the work and outlines possible directions for future developments.

Chapter 2

Background and Research Scope

This section provides the basic concepts necessary to contextualize the research objectives and understand the methodological choices. An overview of the Organic Rankine Cycle is provided, focusing subsequently on the specific characteristics of the ORCHID turbine.

2.1 Organic Rankine Cycle Systems

Organic Rankine cycle (ORC) systems are a technology used to convert thermal energy from low- and medium-temperature sources into electrical or mechanical energy. ORCs are a widespread technology employed for numerous sectors, including the recovery of residual heat from industrial processes, the conversion of geothermal energy and the production of electricity from biomass. More recently, it aroused the attention of the aerospace industry, which is increasingly interested in residual heat recovery practices, also with the goal of reducing consumption and achieving climate neutrality. As discussed by Majer [2], the properties of ORC-based systems, such as the small size of radial inflow turbines and the flexibility resulting from the use of organic working fluids, make them particularly attractive to sectors where reliability, efficiency and weight reduction are key requirements.

As discussed in [3, 8], at low source temperatures, steam Rankine cycles face a poor thermal matching in the heat exchanger due to the high latent heat of water. As shown in Figure 2.1, during the heat exchange, water undergoes a nearly isothermal phase change, while the heat source temperature decreases linearly. In contrast, organic fluids feature a more gradual temperature rise, resulting in a reduced temperature difference and lower second-law losses.

An other issue represented by the steam is the low pressures of the cycle, imposed by the low temperature heat source. This limits the enthalpy drop across the turbine and, as a consequence, the work extracted.

Furthermore, the use of water vapor causes condensation and lubrication problems, as water is unable to lubricate the contact surfaces inside the expander [3, 8].

These issues are overcome in the Organic Rankine Cycle, where water is replaced by an organic working fluid characterised by a lower boiling point and greater

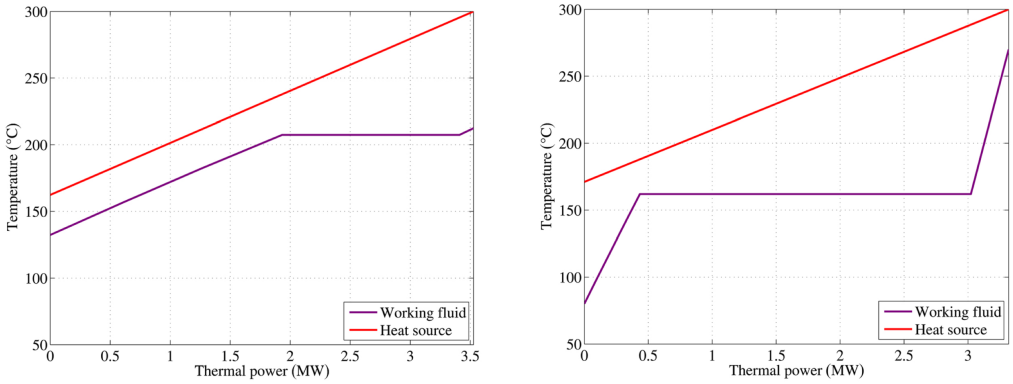

(a) Q–T diagram of the evaporator of the ORC system

(b) Q–T diagram of the boiler of a steam power plant

Figure 2.1: Comparison between Q–T diagrams of the evaporator of a ORC system and of the boiler of a steam power plant, assuming a heat source at 300°C. From Colonna et al. [3].

molecular complexity. As discussed by Colonna et al. [3], this choice allows the use of compact turbomachinery and the consequent achievement of reduced rotational speeds and greater efficiencies.

Typical Layout of an ORC System

Similarly to the steam Rankine cycle, the organic Rankine cycle is operated through four main components: a feed pump, an evaporator, an expander (in this case a turbine), and a condenser. The liquid working fluid pressure is increased in the pump, heat is supplied in the evaporator via heat exchange with an heat source, and useful work is extracted in the turbine before the vapor is finally condensed back to the liquid phase in a second heat exchanger.

A schematic representation of a typical ORC system and the corresponding thermodynamic cycle are shown in Figure 2.2.

Compared to steam-based cycles, Organic Rankine Cycles typically operate with smaller isentropic enthalpy drops and higher volumetric flow. This allows for turbines with a limited number of stages, a lower rotational speed and comparatively large flow passages. Moreover, several ORC working fluids are also lubricant and with a completely dry expansion process, which solves the lubrication and blade erosion issues. However, the low sound speed of organic vapors causes the flow to become supersonic even at moderate pressure ratios, often leading to highly supersonic stator flows that require careful aerodynamic design.

Non-ideal compressible fluid-dynamics

ORC systems employ organic working fluids that, at some stages of the cycle, are in a non-ideal thermodynamic regime. When the fluid is in a state close to the critical point, significant deviations from ideal-gas behavior can occur, affecting both the

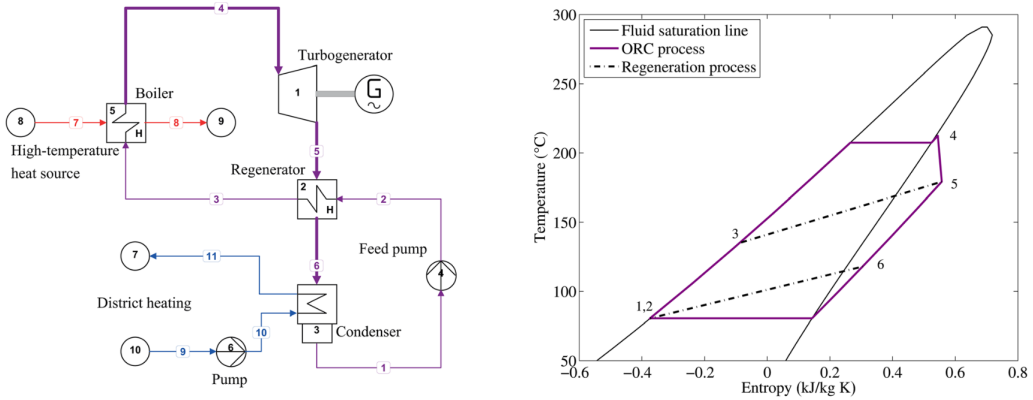

(a) Schematic layout of a generic Organic Rankine Cycle system, including pump, evaporator, turbine, and condenser.

(b) Representation of the Organic Rankine Cycle in the temperature–entropy plane.

Figure 2.2: Organic Rankine Cycle layout and thermodynamic cycle representation. From Colonna et al. [3].

thermodynamic performance of the cycle and the aerodynamic characteristics of the turbine. A more detailed discussion of these phenomena is provided by Guardone et al. [9]. This study emphasize the significant influence that the effects of a real fluid have on the analysis of ORC turbomachinery.

A feature belonging to non-ideal fluids is the intimate coupling between gas dynamics and thermodynamics, and the discrepancy from the ideal-gas behavior is governed by the fundamental derivative of gas dynamics [10],

$$\Gamma = 1 + \frac{v}{c}\left(\frac{\partial c}{\partial v}\right)_s \tag{2.1}$$

where v is the specific volume, c is the speed of sound in the fluid and $(\partial c/\partial v)_s$ represents the partial derivative of the speed of sound with respect to the specific volume at constant entropy. The fundamental derivative is a non-dimensional parameter that represents the speed of sound variation with pressure along an isentropic transformation.

If $\Gamma > 1$, the speed of sound increases with isentropic compressions following the typical behavior of ideal gases where

$$\Gamma = \frac{\gamma + 1}{2} \tag{2.2}$$

and $\gamma > 1$ is the specific heats ratio. Conversely, in a non-ideal-gas the speed of sound decreases in isentropic compressions showing a $\Gamma < 1$. This condition includes fluid dynamic effects that influence several aspects of ORC turbine flows, including shock-wave topology, non monotonic variation of Mach number along isentropic expansions and its discontinuous increase across oblique shocks [9]. Consequently, an accurate representation of non-ideal compressible flow effects is essential for a reliable CFD analysis of ORC turbomachinery, for the interpretation of experimental

measurements and for the definition of suitable measurement strategies.

Another parameter used to quantify the departure from the ideal gas model is the compressibility factor,

$$Z = \frac{P\,v}{R\,T}, \tag{2.3}$$

where P is the pressure, v is the specific volume, R is the specific gas constant and T is the temperature.

A fluid in the ideal gas state features $Z \approx 1$ [9]. In dilute-gas conditions, with lower pressure and higher temperature than the critical values, the ideal-gas behavior is recovered so $Z = 1$. By progressively increasing the pressure, the attractive intermolecular forces lead to a specific volume lower than the ideal one so Z values are below the unit. This state is found close to the vapour-liquid saturation curve, where the ideal gas model is no longer accurate. At extremely high pressure, the repulsive intermolecular forces become predominant and Z exceeds the unity.

Non-ideal effects are more pronounced for molecularly complex fluids, such as compounds used as working fluids in organic Rankine cycle [9]. Molecular complexity is related to the number of active molecular degrees of freedom N, which depends on the number of atoms, molecular arrangement and temperature.

2.2 Radial Inflow Turbines

The analysis and description of radial inflow turbines presented in this section are primarily based on the classical design framework outlined by Whitfield and Baines [11] and on the comprehensive overview of radial turbomachinery design challenges provided by Casey [12].

Radial-inflow turbines are used in small- and medium-scale power applications, such as turbochargers or ORC cycles, where the main requirements are compactness, robustness, and the ability to handle high pressure ratios in a single stage.

A radial inflow turbine stage is made up of four main components: volute, stator, rotor, and diffuser. The volute distributes the incoming flow in a circumferential direction, giving it the right angular momentum. Downstream of the volute, the flow encounters the stator, where it is further accelerated and deflected by the blades. The flow is then conveyed in a predominantly radial direction into the rotor and gradually deflected inward. At the rotor exit, the flow, with a predominantly axial direction, is guided towards the diffuser. In this last component, the flow is decelerated, recovering part of the residual kinetic energy and thus improving the turbine's overall efficiency.

If compared to axial turbines, radial ones are generally more compact and require less stages to achieve the same total enthalpy drop. This simplifies their design by reducing manufacturing complexity. Moreover, thanks to their smaller diameters, their inertia is lower, leading to faster dynamic responses.

From an aerodynamic point of view, radial turbines are capable of achieving higher efficiencies at lower specific work and speed, which represent a fundamental feature for ORC applications. In contrast, axial turbines are more suitable for large

scale applications with high mass flow rates, where multiple stages with cooling strategies can be employed.

The suitability of different families of turbines under different working conditions can be visualized in the Balje N_s–D_s graph in Figure 2.3, which shows the efficiency of turbines related to the specific speed N_s and the specific diameter D_s. The definitions of these two parameters is

$$N_s = \frac{N\sqrt{\dot{V}_3}}{H_{ad}^{3/4}}, \qquad D_s = \frac{D\,H_{ad}^{1/4}}{\sqrt{\dot{V}_3}}, \tag{2.4}$$

where N is the rotational speed, $\dot{V}_3$ is the volumetric flow rate at turbine outlet, H_{ad} is the isentropic enthalpy drop and D is the rotor inlet diameter.

Using the ORCHID turbine design data as representative operating conditions of RIT ($N = 98{,}100$ rpm, $\dot{V}_3 = 7.87 \times 10^{-2}$ m^3 s^{-1}, $H_{ad} = 91.3$ kJ kg^{-1}, $D = 40$ mm), the resulting similarity parameters are

$$N_s \approx 70.8, \qquad D_s \approx 1.04. \tag{2.5}$$

Referring to Figure 2.3 it can be observed that the point corresponding to the coordinates found lies within the region of maximum efficiency associated with radial turbines. This confirms that at relatively low specific work and rotational speeds radial turbines allows to reach an higher efficiency than axial ones.

Another advantage of the radial inflow turbines is their ability to withstand non-uniform and unsteady flow conditions, which further supports their use in ORC installations, where this kind of flow is expected. For these reasons, the ORCHID facility adopts a single-stage radial inflow turbine architecture, which is well aligned with the operating conditions.

2.3 The ORCHID Facility at TU Delft

The ORCHID (Organic Rankine Cycle Hybrid Integrated Device) facility is an experimental test rig developed at the Propulsion and Power Laboratory of the Faculty of Aerospace Engineering at Delft University of Technology. The aim of the future experimental campaing on this facility is to investigate the fluid-dynamic performance of radial inflow turbines operating with organic working fluids under non-ideal compressible flow conditions. The facility has been conceived to provide high-quality experimental data for the validation of numerical tools and design methodologies for Organic Rankine Cycle (ORC) applications, with a particular focus on dense vapor expansions and supersonic flow regimes.

The design of the ORCHID turbine test bed is described in depth in the works of De Servi et al. [6, 14] and in the PhD dissertation of Majer [2], which are taken as primary references for this work.

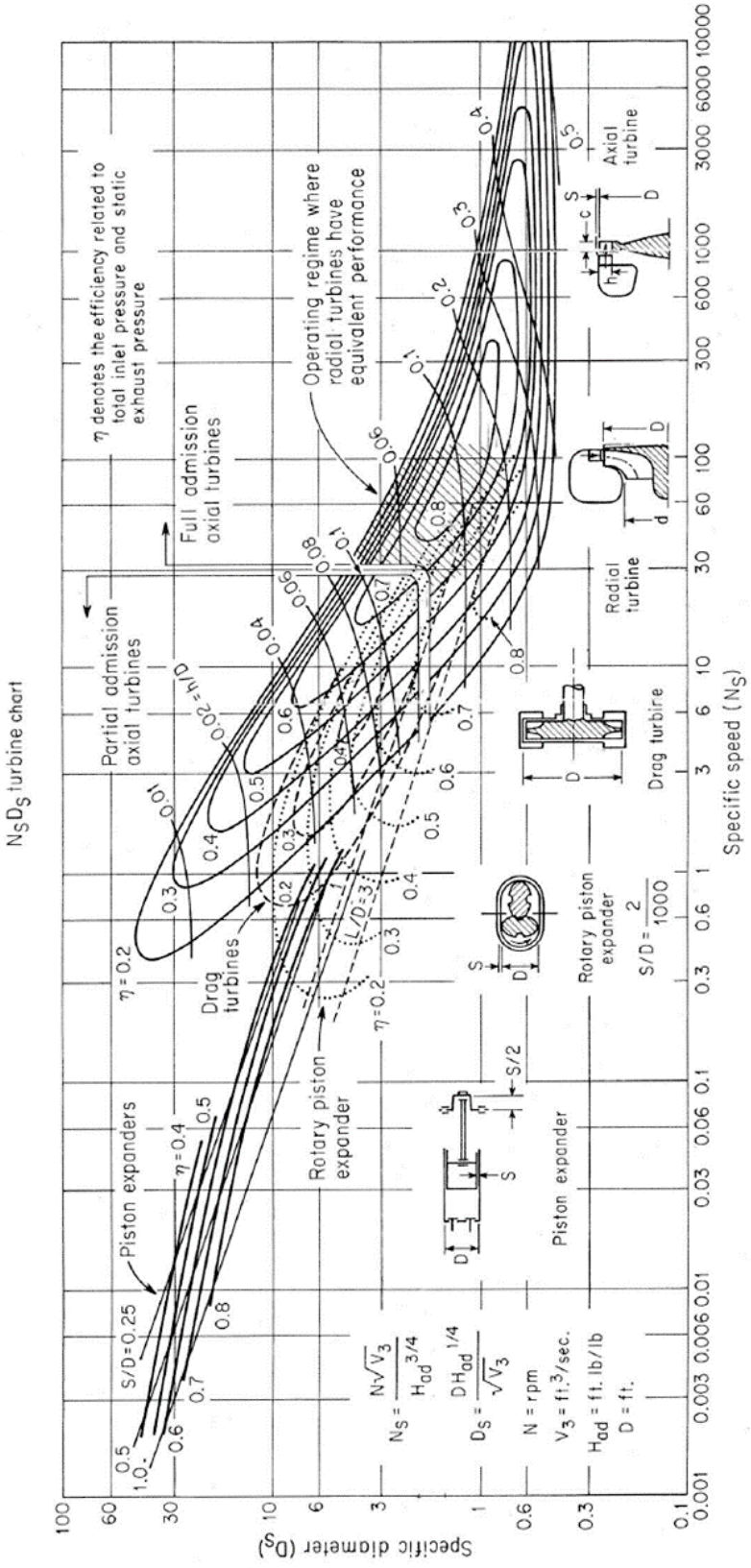

Figure 2.3: Balje $N_s - D_s$ efficiency chart for turbines. Adapted from [13]

ORCHID Turbine Test Bed Overview

An overview of the complete test rig layout is reported in Fig. 2.4, adapted from the work of Head [15], where the overall architecture and operating philosophy of the facility are described in detail.

The test rig reproduces an ORC loop, in which the working fluid circulates continuously through the main thermodynamic components of the cycle. This system involves a liquid pump, an electrically heated evaporator, the radial inflow turbine, a condenser and a set of auxiliary components including pipes, valves, heat exchangers, and the control system. This configuration enables controlled operations over a wide range of conditions, achieved by changing the pressure ratio, the rotational speed and the thermodynamic conditions.

The loop followed by the flow is schematically illustrated in the flow diagram in Fig. 2.5, adapted from [15].

The working fluid extracted from the tank is pressurized by the boost pump and subsequently by the main pump, which increases its pressure up to the required level. The fluid is then preheated in a regenerator, where the heat source is the hot vapor exiting the turbine. The recovery process improves the overall cycle efficiency, reducing the thermal load on the primary heater. Once preheated, it passes to the evaporator, which consists of a heat exchanger that allows the fluid phase transition from liquid to vapor. This vapor is then directed to the turbine, where the mechanical power is extracted through the expansion process.

The thermodynamic cycle ends in the condenser, where the fluid is cooled down and returned to liquid form. During starting phase or in some off-design conditions, the flow, or part of it, is conveyed directly to the condenser through a turbine bypass line that starts downstream of the evaporator. This configuration improves operational flexibility while ensuring precise control of the turbine inlet conditions.

The ORCHID facility is specifically designed to operate with an organic working fluid called Siloxane MM[1] under high-pressure and high-temperature conditions, where dense-vapor and non-ideal thermodynamic effects become significant.

As discussed in [15], this imposes stringent safety requirements on the entire installation. For this reason, the test rig is designed in compliance with ATEX regulations [16](Zone 2 with temperature class T2[17]), which regulates the use of potentially hazardous fluids and electrical equipment in explosive environments.

The adoption of ATEX-certified components, together with dedicated safety systems and operating procedures, constitutes a fundamental constraint that has strongly influenced the mechanical layout and component selection of the facility.

[1] Siloxane MM refers to Hexamethyldisiloxane (HMDSO), $C_6H_{18}OSi_2$.

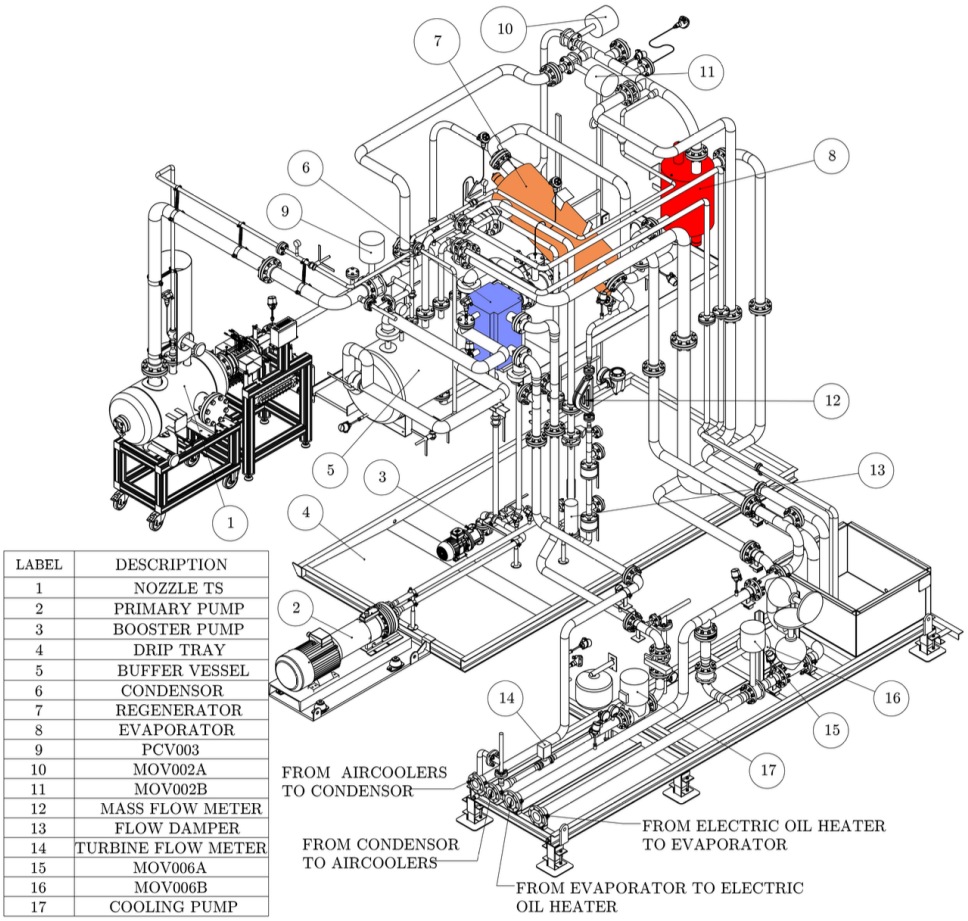

LABEL	DESCRIPTION
1	NOZZLE TS
2	PRIMARY PUMP
3	BOOSTER PUMP
4	DRIP TRAY
5	BUFFER VESSEL
6	CONDENSOR
7	REGENERATOR
8	EVAPORATOR
9	PCV003
10	MOV002A
11	MOV002B
12	MASS FLOW METER
13	FLOW DAMPER
14	TURBINE FLOW METER
15	MOV006A
16	MOV006B
17	COOLING PUMP

Figure 2.4: CAD isomeric view of the ORCHID turbine test bed. Adapted from [15].

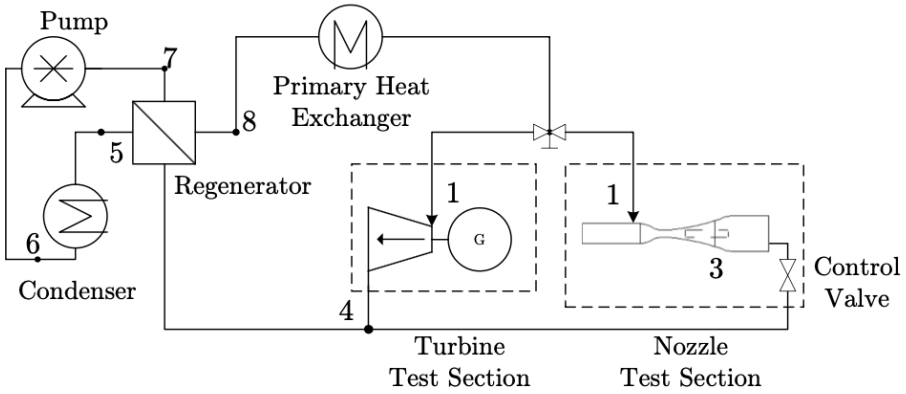

Figure 2.5: Simplified flow diagram of the ORCHID facility, illustrating the closed-loop Organic Rankine Cycle followed by the working fluid. The main components include the pump, regenerator, evaporator, turbine test section, bypass line, and condenser. Adapted from [15].

The ORCHID turbine test section

The ORCHID turbine represents a prototype for low-power ORC applications and consists of a single-stage radial inflow turbine, characterized by a high expansion ratio and rotational speed.

At the design operating condition, the turbine delivers approximately 10 kW of mechanical power at a rotational speed close to 98 krpm. Its high expansion ratio ($>$ 40) leads to highly supersonic flow within the stator vanes, with local Mach numbers exceeding 2, and to large flow deflections within the rotor passages.

The main thermodynamic design parameters of the ORCHID turbine are summarized in Table 2.1, while the principal geometric characteristics of the stage are reported in Table 2.2. The turbine stage consists of a radial stator followed by a radial–axial impeller.

Table 2.1: Main thermodynamic design parameters of the ORCHID turbine.

Parameter	Value
Inlet total pressure P_{t0}	18.1 bar
Inlet total temperature T_{t0}	300 °C
Outlet static pressure P_3	0.44 bar
Pressure ratio PR	40.84
Rotational speed n	98.1 krpm
Mass flow rate $\dot{m}$	132 g/s
Estimated Total–static efficiency η_{ts}	83%

Table 2.2: Main geometric parameters of the ORCHID turbine stage.

Parameter	Value
Impeller inlet radius R_2	25.75 mm
Exducer hub radius R_{3h}	8.2 mm
Impeller inlet blade height b_2	2 mm
Impeller exit blade height b_3	12.3 mm
Impeller axial length L_{ax}	10.2 mm
Stator outlet flow angle α_1	78°
Impeller inlet relative angle β_2	35.5°
Impeller exit relative angle β_3	−57.6°

The stator is designed as a convergent–divergent nozzle row that accelerates the flow to supersonic conditions and imposes a large absolute flow angle at the rotor inlet. The impeller then turns the radial component of the flow toward an axial direction while extracting mechanical work from the expanding vapor. The rotor has 13 blade passages while the stator has 12.

The meridional view of the turbine stage with the conventional enumeration assigned to each station, is shown in Figure 2.6. Section 0 corresponds to the volute inlet, section $0'$ indicates the stator inlet and 1 its outlet, section 2 and 3 stands respectively for impeller inlet and outlet, while section 4 is the diffuser outlet.

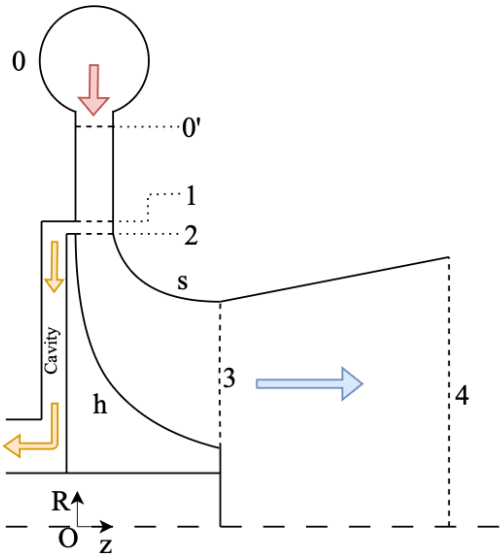

Figure 2.6: Meridional view of the ORCHID turbine stage and reference flow sections. Adapted from Majer [2].

Although the volute and diffuser were designed as part of the overall machine, the fluid-dynamic analyses presented in this thesis focus on the stator–rotor stage and the downstream outlet region.

In Figure 2.7 a three-dimensional view of the radial inflow turbine developed at the ORCHID facility is shown. Here it is possible to recognize the main components such as the turbine inlet, the stator plate, the rotor wheel (in red), the primary diffuser cone, of which the first segment is a cylindrical duct, and the secondary diffuser cone.

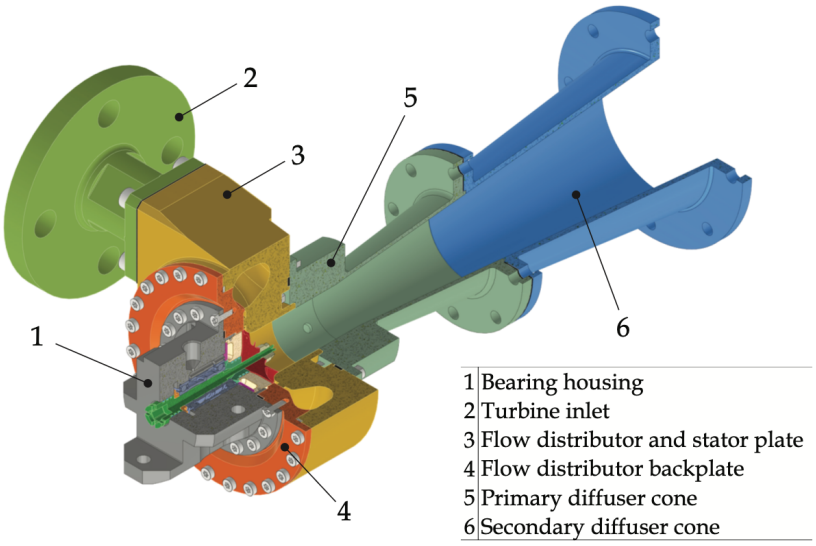

Figure 2.7: Three-dimensional view of the ORCHID radial inflow turbine developed at TU Delft. The turbine is designed for experimental investigations of high-temperature ORC systems. Image adapted from [2].

2.4 Research Scope and Objectives

The overall objective of the present research is to design a total-pressure measurement system for the ORCHID radial inflow turbine, with the aim of experimentally characterizing the turbine performance and supporting the validation of numerical predictions.

This system has to comply with the space constraints and safety regulations of the facility.

In order to achieve this objective, it is necessary to answer the following research questions:

Q1 What is the spatial distribution of total pressure at the rotor outlet and how does it evolve up to the measurement plane?

Q2 To what extent do circumferential flow non-uniformities persist downstream of the rotor and how do they affect the pressure probe selection?

Q3 Are residual swirl and flow angle variations still significant at the measurement plane and what implications do they have for probe type and orientation?

Chapter 3

Methodology

Three dimensional numerical simulations were carried out using the geometrical model and the spatial discretization of [2] and subsequently a cylindrical domain was added downstream of the rotor to study the flow field in this region. These CFD simulations represent a preliminary investigation tool used to characterize the flow field, in order to assess the feasibility and the challenges associated with total pressure measurements in a non-uniform and potentially swirling flow, prior to the experimental campaign. All of these characteristics can significantly affect the accuracy and reliability of measurements made with traditional probes, so numerical results are essential for guiding the design of the experimental measurement system and the selection of a suitable probe.

The overall research workflow adopted is summarized in Figure 3.1.

This chapter introduces the computational domain and the baseline numerical setup adopted for the simulations, describes the CFD workflow and the different modeling strategies investigated, and analyzes the solution dependence to different outlet boundary models. Finally, it presents the mesh sensitivity study conducted.

3.1 CFD Setup

The CFD setup adopted in this work is derived from a numerical framework developed and validated during earlier research activities on the ORCHID turbine. This framework, documented in detail in [2], represents the starting point of the present analysis, which was progressively extended to address the specific objectives of this thesis.

The computational domain described in Chapter 4 of [2], consists of a reduced annular sector including both the stator and the rotor passages. The stationary domain comprises a convergent–divergent stator vane passage corresponding to a sector of 1/12, while the rotating domain includes a single impeller blade channel of 1/13. The stator and rotor domains are coupled through a mixing-plane interface, which enables steady-state simulations at a reduced computational cost by circumferentially averaging the flow variables exchanged between the stationary and rotating frames of reference.

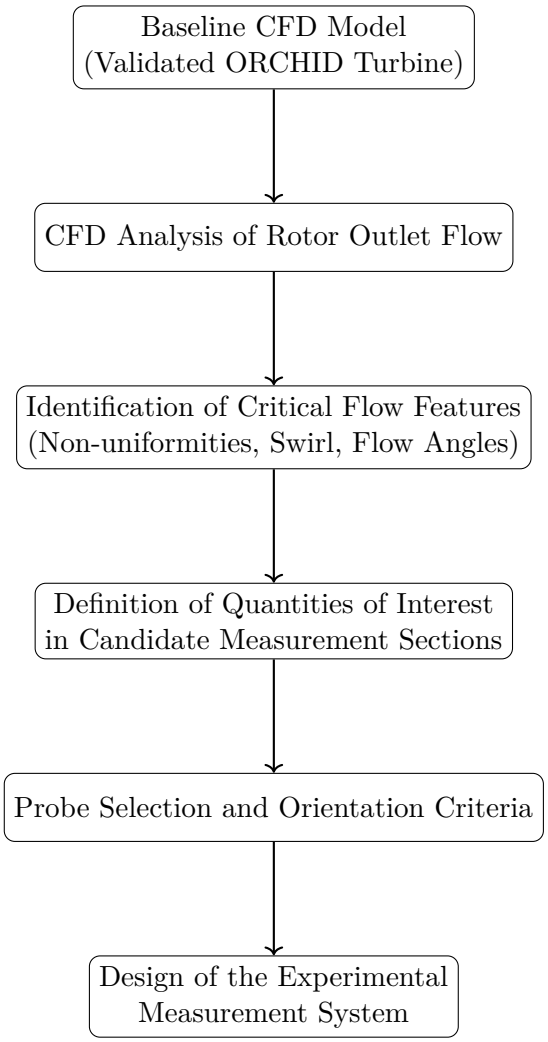

Figure 3.1: Overall research workflow adopted in this work, highlighting the CFD-driven approach used to support the design of the experimental measurement system.

This approach was selected as a suitable compromise between accuracy and efficiency for the baseline simulations.

The numerical model does not include the volute, the downstream diffuser and the cavity behind the impeller disk, while a tip clearance of 0.2 mm is prescribed between the tip of the impeller and the shroud.

The mesh, generated through ANSYS® TurboGrid [18], is designed to resolve boundary layers, shocks and regions of strong flow curvature, all features present in a flow that passes through highly supersonic stator and transonic–supersonic rotor passages. The baseline grid is made of approximately three million cells and is already demonstrated to provide mesh-independent results [2].

The flow is modeled using the Reynolds-Averaged Navier–Stokes (RANS) equations. Spatial discretization of the advection terms is performed using a second-order accurate central difference scheme, while turbulence effects are modeled using the shear stress transport (SST) k–ω model. The transport equations of the turbulence model are discretized using a hybrid scheme following the approach proposed by Barth and Jespersen [19].

All simulations were performed using ANSYS® CFX [20]. The baseline configuration was first analyzed in order to ensure consistency with the reference numerical simulations and provide a reliable initial solution for subsequent CFD analyses.

The simulations presented in the following sections refer to the on-design operating condition, characterized by a rotor rotational speed of 98 krpm and a total pressure of 18 bar prescribed at the stator inlet [2].

3.1.1 Selection of the interface model

In the mixing-plane approach, the flow variables exchanged between the stationary and rotating domains are circumferentially averaged at the interface. This formulation is well suited for predicting global performance parameters at a reduced computational cost. However, it suppresses azimuthal non-uniformities associated with the stator discharge flow and, as a consequence, wake structures are interrupted at the stator–rotor interface.

In contrast, the frozen-rotor approach preserves the relative circumferential position between stator and rotor blades. This allows non-axisymmetric flow features to be transferred across the interface without circumferential averaging. For this reason, the frozen-rotor approach was adopted in place of the mixing-plane formulation, as it provides a more suitable framework to visualize the persistence and spatial extent of stator-induced non-uniformities. This capability is essential for the interpretation of downstream flow features relevant to the experimental measurement campaign.

Numerical setup and initialization strategy

To ensure that the new frozen-rotor configuration remained consistent with the baseline simulation, the mesh, turbulence model, boundary conditions, and spatial discretization schemes were kept unchanged, and the setup was similarly configured.

A multi-step initialization strategy was adopted to ensure stable convergence. The solution was first initialized in three subsequent steps keeping a blend factor equal to zero. The blend factor controls the contribution between first-order upwind discretization and higher-order schemes. Setting a value of 0.0 is equivalent to using the first order advection scheme, which is the most robust option. A value of 1.0 corresponds to second order differencing for the advection terms, which improve accuracy at the cost of reduced numerical stability. Values from 0.0 to 1.0 allow for a gradual transition toward higher-order, with increased accuracy and reduced robustness when approaching 1.0 [21]. In these subsequent steps the outlet static pressure was decreased from 5 bar to the target of 0.44 bar while the rotational speed was increased starting from 0 rpm until it reached the nominal value. Both quantities were varied following a linear ramp, implemented choosing three equally spaced values of pressure and rotational speed. This procedure allowed the flow field to adapt slowly to the new conditions, avoiding numerical instabilities.

Once a stable solution was obtained and the target values of pressure and speed were met, the blend factor was raised to 0.5.

As we can see in Figure 3.2, which shows the convergence history, convergence was monitored by tracking the trend of mass and momentum equation residuals, but also selected quantities such as mass flow rate and error, and total-to-static pressure ratio. The pressure ratio is the ratio between the total pressure at the stator inlet and the static pressure imposed at the outlet boundary, while the mass flow rate and the mass flow error are defined as

$$\text{Mass Flow Rate} = \sum \dot{m}_{\text{in}} \tag{3.1}$$

$$\text{Mass Flow Error} = \frac{\sum \dot{m}_{\text{in}} - \left|\sum \dot{m}_{\text{out}}\right|}{\sum \dot{m}_{\text{in}}}. \tag{3.2}$$

where $\sum \dot{m}_{\text{in}}$ and $\sum \dot{m}_{\text{out}}$ are the mass flow rates through the inlet and outlet boundaries. The solution was considered sufficiently accurate when the residuals of all governing equations were lower than 10^{-5} and at the same time the mass flow error stabilized around zero and the pressure ratio reached a steady value consistent with the imposed outlet pressure. Only once these convergence criteria were simultaneously satisfied, the subsequent step could be taken.

A similar initialization procedure was adopted for all simulations presented in this work.

Flow field analysis and comparison with mixing-plane results

The frozen-rotor results were post-processed focusing on the quantities relevant for the experimental investigation, namely Mach number, static pressure, total pressure and entropy.

Figure 3.3 shows the entropy profiles on a constant span surface both with mixing-plane and frozen-rotor interfaces. In the left hand side picture, which was

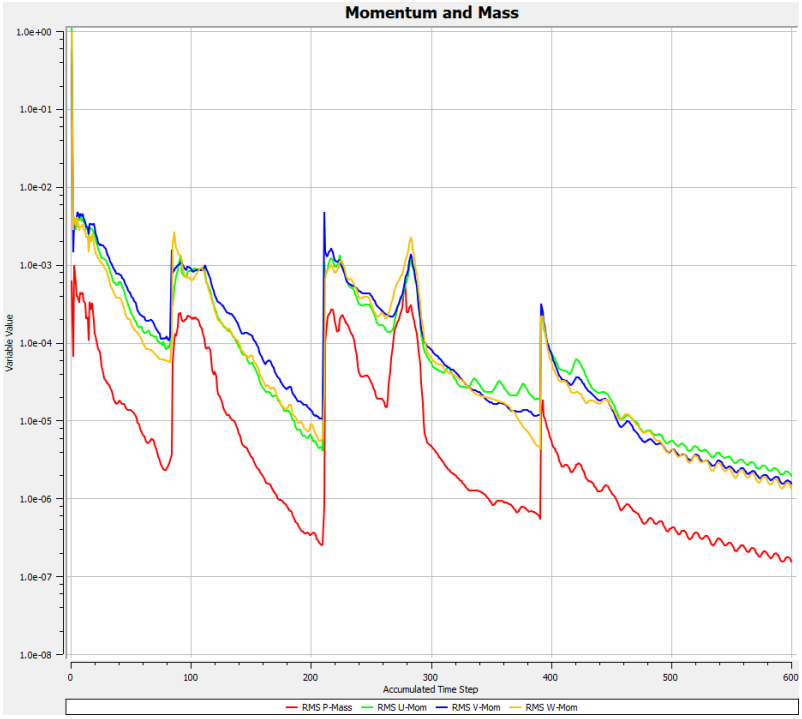

Figure 3.2: Convergence history of the frozen-rotor simulation during the initialization phase.

obtained by simulating the flow using a mixing plane interface, one can see that the wakes cast by the stator vane trailing edges are averaged out across the mixing plane. Hence, the flow entering the rotor domain is uniform. On the contrary, the right hand side picture shows the solution obtained using a frozen rotor interface, and one can notice that the stator trailing edge wakes persist within the rotor domain.

This difference between the two approaches is also visible at the rotor outlet shown in Figure 3.4. While in the mixing plane configuration the wake extend over a shorter distance downstream of the rotor blades trailing edge, in the frozen rotor they persist further downstream. This behavior confirms the suitability of the frozen rotor interface for verifying the spatial extent of non-uniformities and their potential impact on downstream flow measurements. These observations motivate a further investigation of the outlet channel, aiming to quantify the spatial extent of wake structures.

Total pressure, Mach number and static pressure fields were also analyzed and shown respectively in Figure 3.5, 3.6 and 3.7. Figure 3.6 shows that the flow at stator exit is strongly accelerated due to the supersonic expansion in the blade channels, while, within the rotor passages, the Mach number distribution is the product of the combined effects of curvature and rotation.

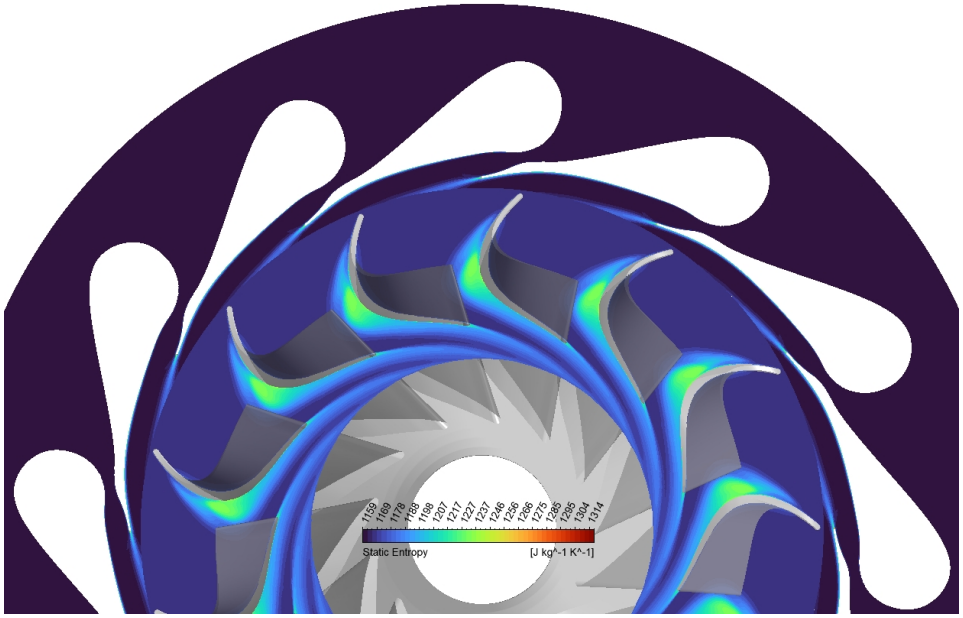

(a) Mixing-plane solution at the stator–rotor interface.

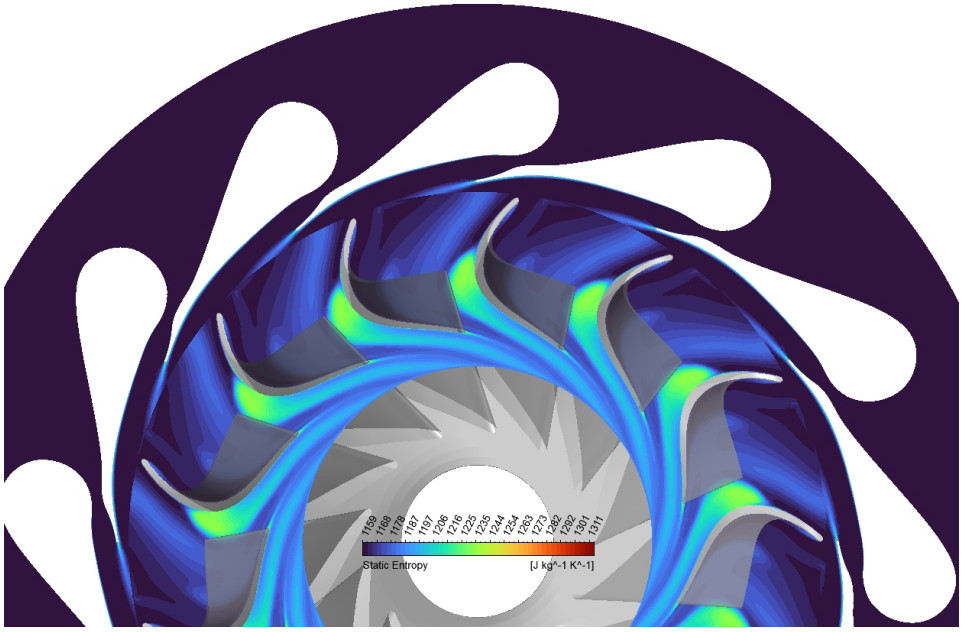

(b) Frozen-rotor solution at the stator–rotor interface.

Figure 3.3: Comparison of entropy contours at the stator–rotor interface obtained using the mixing-plane and frozen-rotor approaches. The frozen-rotor solution preserves stator wake structures that are circumferentially averaged in the mixing-plane case.

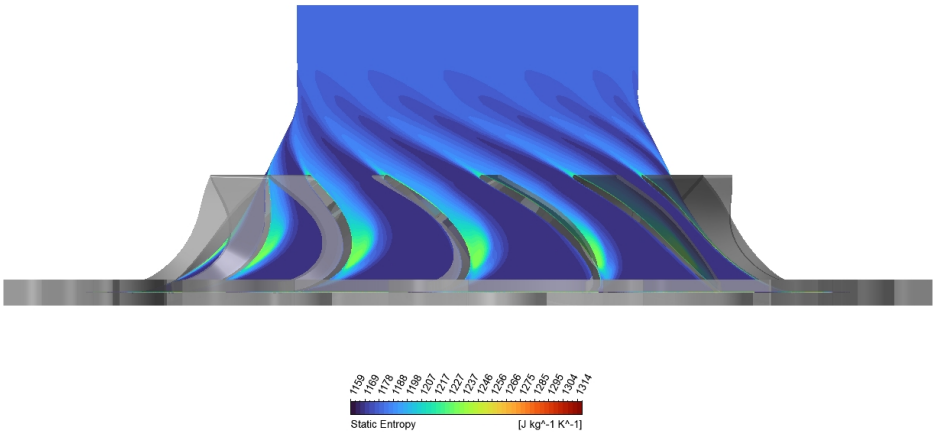

(a) Axial view of the entropy field obtained with the mixing-plane approach.

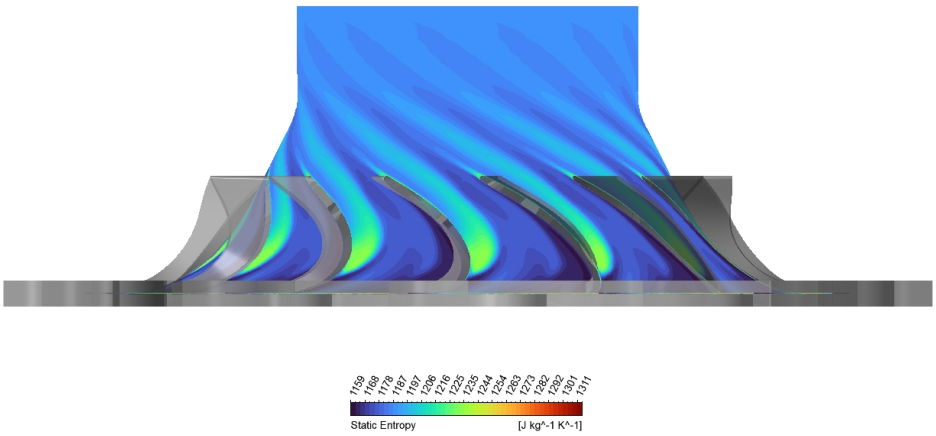

(b) Axial view of the entropy field obtained with the frozen-rotor approach.

Figure 3.4: Axial comparison of entropy contours obtained using the mixing-plane and frozen-rotor approaches. The frozen-rotor simulation highlights the downstream persistence of entropy wakes towards the outlet region.

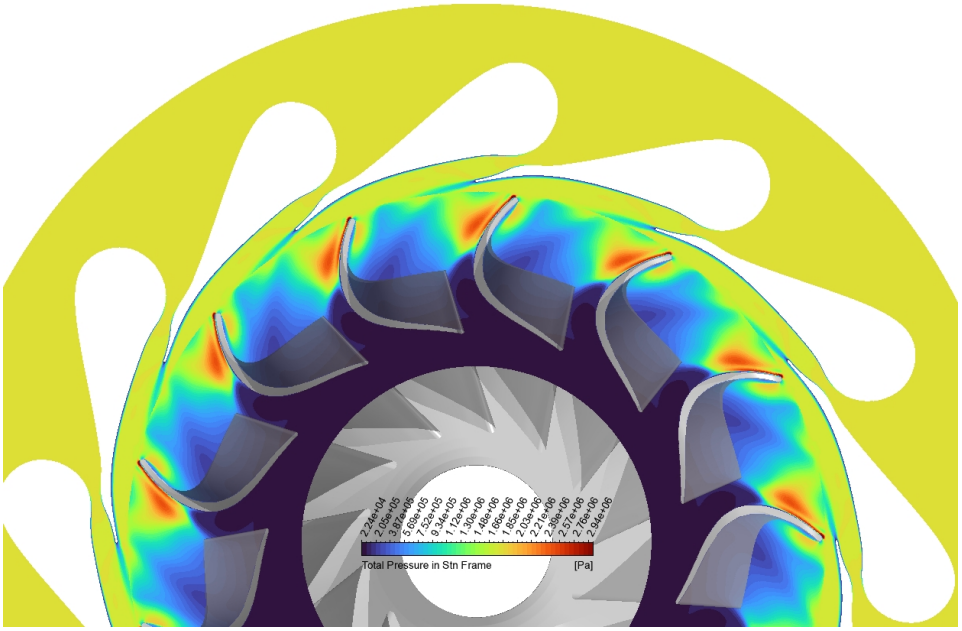

Figure 3.5: Total pressure contours obtained from the frozen-rotor simulation.

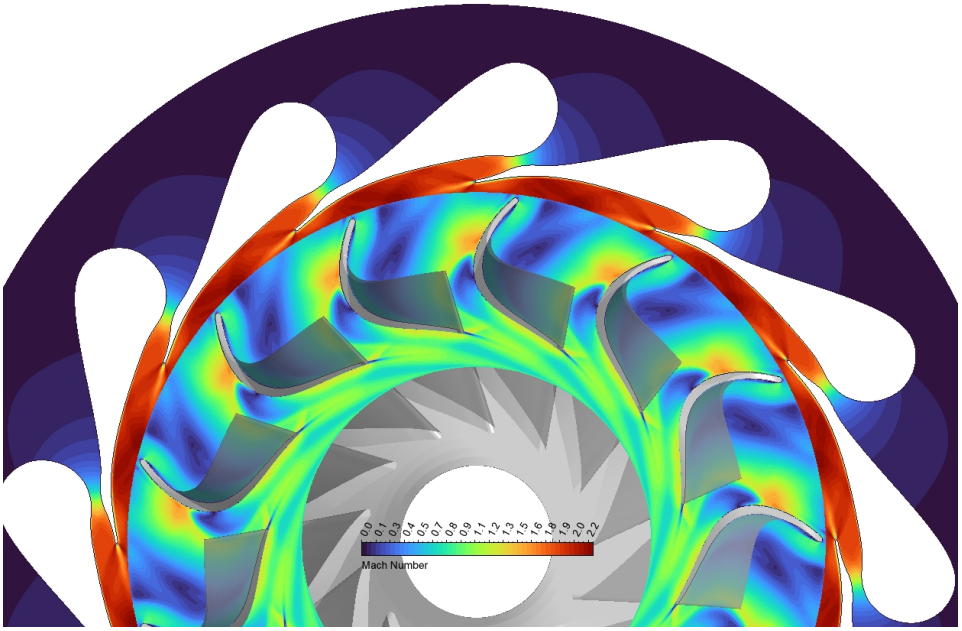

Figure 3.6: Mach number distribution obtained from the frozen-rotor simulation.

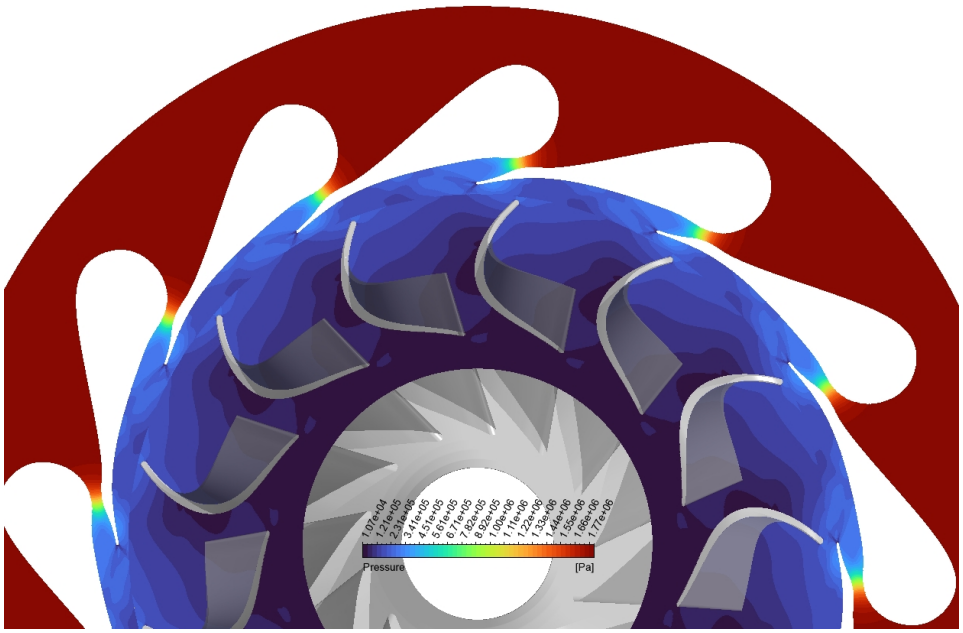

Figure 3.7: Static pressure field obtained from the frozen-rotor simulation.

3.1.2 Simulation with Outlet Channel

In order to investigate the evolution of the flow downstream of the rotor, the computational domain was extended by including a cylindrical outlet channel downstream of the impeller. The predisposed measurement section is located at a distance of 60 mm from the rotor outlet, so this extension of the domain is needed to inspect the persistence of flow non-uniformities and swirl up to this distance.

Geometry extension and modeling strategy

The first step taken was modeling the geometry of the cylindric outlet channel downstream of the rotor. The existing outlet geometry, created in ANSYS® BladeGen [22], was extended and meshed together with the existing stator-rotor domain. To avoid issues with mesh quality, which degrades exponentially with very sharp corners, the central edge of the sector has been slightly rounded. With this approach it was possible to obtain a good quality mesh, characterized by low skewness and distortions, while maintaining consistency with the stator and rotor meshes.

The outlet channel was extended up to 90 mm downstream of the rotor, to minimize interference of the boundary condition with the flow solution obtained in the measurement section, which is located 60 mm from the rotor. For simplicity, a circular ogive was modeled when extending the hub of the rotor domain. However, the manufactured rotor disk features a lock nut whose shape should affect the flow field differently, but this aspect was deemed outside the scope of the present work.

A view of the extended computational domain, including the stator, rotor and the cylindrical outlet channel, is reported in Figure 3.8, where the measurement section location is highlighted.

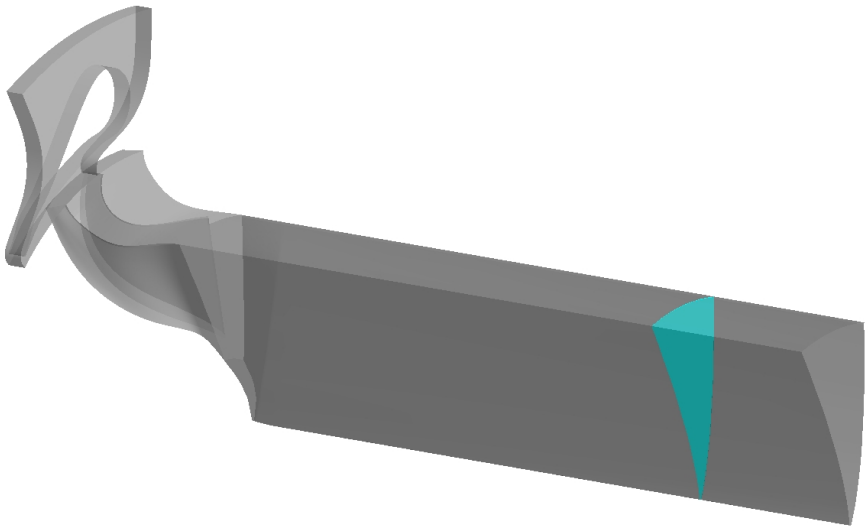

Figure 3.8: Computational domain including stator, rotor and extended cylindrical outlet channel.

Mesh generation

The meshes of the stator and rotor domains were kept unchanged with respect to the baseline configuration, while the outlet channel mesh was newly generated. The outlet mesh consists of approximately 340 000 elements, with an expansion rate of 1.1 along the streamwise direction to ensure a gradual resolution coarsening downstream. The near-wall region was treated with a boundary layer refinement based on the first element offset approach. With this method the height of the first cell adjacent to the wall is selected in order to achieve an $y^+ \simeq 1.6$ with a reference Reynolds number of $Re \approx 3.7 \times 10^5$. The expansion rate in the direction normal to the wall was fixed to 1.1 to ensure a gradual growth of the cell size across the boundary layer.

Numerical setup and boundary conditions

The numerical setup was defined in ANSYS CFX-Pre. The stator–rotor domains were modeled in the same manner as in the frozen-rotor simulations discussed in the previous section. Similarly, a frozen-rotor interface was adopted between the rotor and the outlet channel to preserve circumferential non-uniformities.

At the outlet of the domain, a pressure boundary condition was applied. Periodic rotational boundary conditions were imposed on the lateral faces of the sector, while no-slip wall conditions were adopted on the shroud.

Flow Field Analysis

The flow field obtained from the frozen-rotor simulation including the outlet channel was post-processed in ANSYS CFX-Post. Figure 3.9 shows the Mach number

distribution on a constant-span plane. Immediately downstream of the rotor, residual blade-to-blade non-uniformities associated with the rotor wakes are visible. However, these structures progressively weaken along the outlet channel, indicating an effective attenuation of the circumferential gradients. The Mach number field confirms that, while local acceleration effects are present close to the rotor exit, the flow becomes progressively more uniform in terms of velocity magnitude along the duct.

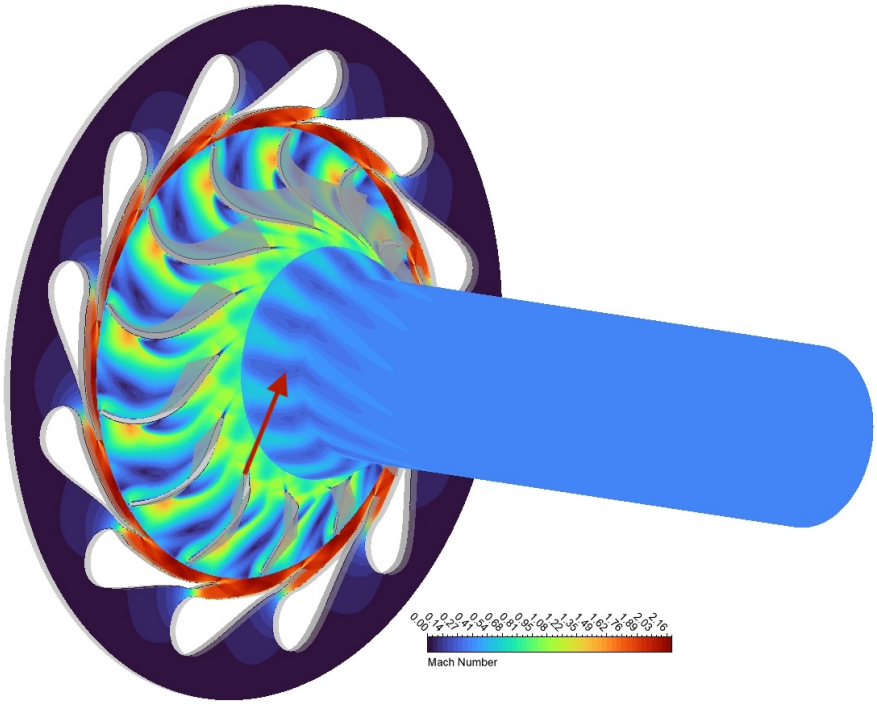

Figure 3.9: Mach number contours on a constant-span plane for the frozen-rotor simulation including the outlet channel. The arrow points towards the rotor wakes.

The streamlines reported in Figure 3.10 highlight the strong residual swirl characterizing the flow downstream of the rotor. Here, a three-dimensional flow angle (α) is represented in a plane perpendicular to the axial direction. This angle is defined as the deviation of the velocity vector from the axial direction and calculated as

$$\alpha = \arctan\left(\frac{\sqrt{V_x^2 + V_y^2}}{|V_z|}\right).$$

Despite the attenuation of circumferential non-uniformities, the flow maintains a pronounced tangential component over the entire outlet length and the flow angle varies consistently along the radial direction. This behavior is a direct consequence of the rotor exit flow angle and is a key result for the experimental campaign, as it directly affects probe alignment and measurement accuracy.

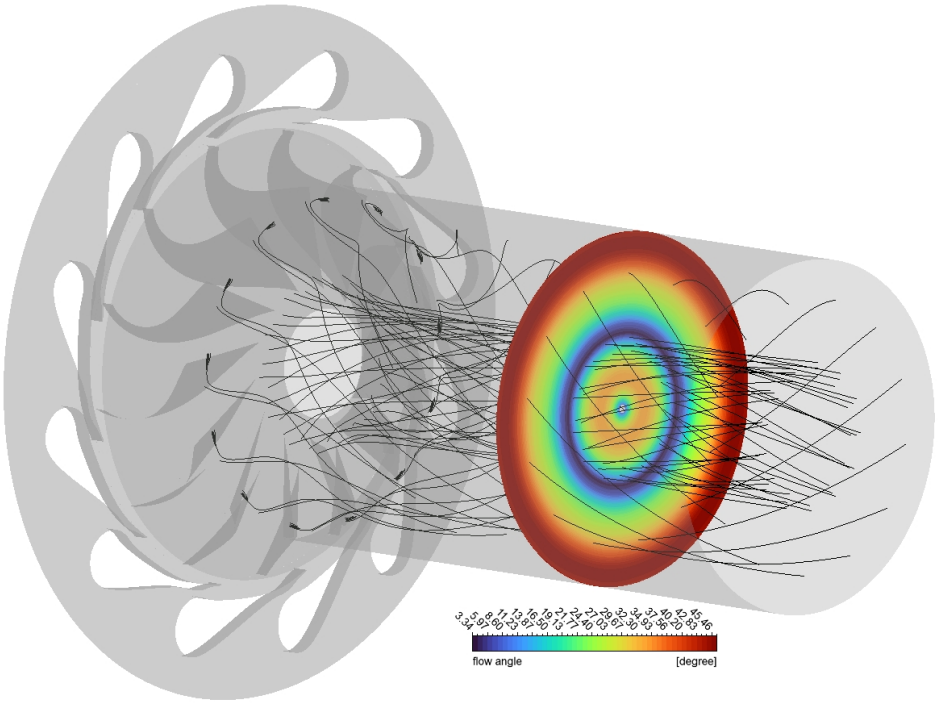

Figure 3.10: The streamlines in the outlet channel highlights the strong residual swirl downstream of the rotor. The three-dimensional flow angle (α) is represented in a plane perpendicular to the axial direction.

Figure 3.11 and Figure 3.12 present respectively the entropy and the total pressure contours on a constant-radius plane. These two quantities exhibit similar trends along the outlet channel, since near the rotor output both quantities show pronounced circumferential non-uniformities associated with the rotor wake pattern and characterized by localized regions of increased entropy and corresponding total pressure deficits. Moving downstream along the outlet channel, the circumferential variations of both entropy and total pressure progressively decay due to viscous mixing and turbulent diffusion.

At the axial location corresponding to the measurement section the wake structures are largely attenuated while a strong residual swirl is still present. This confirms that, despite the strong non-axisymmetric flow features present immediately downstream of the rotor, the flow field at the measurement plane is substantially uniform in terms of entropy and total pressure.

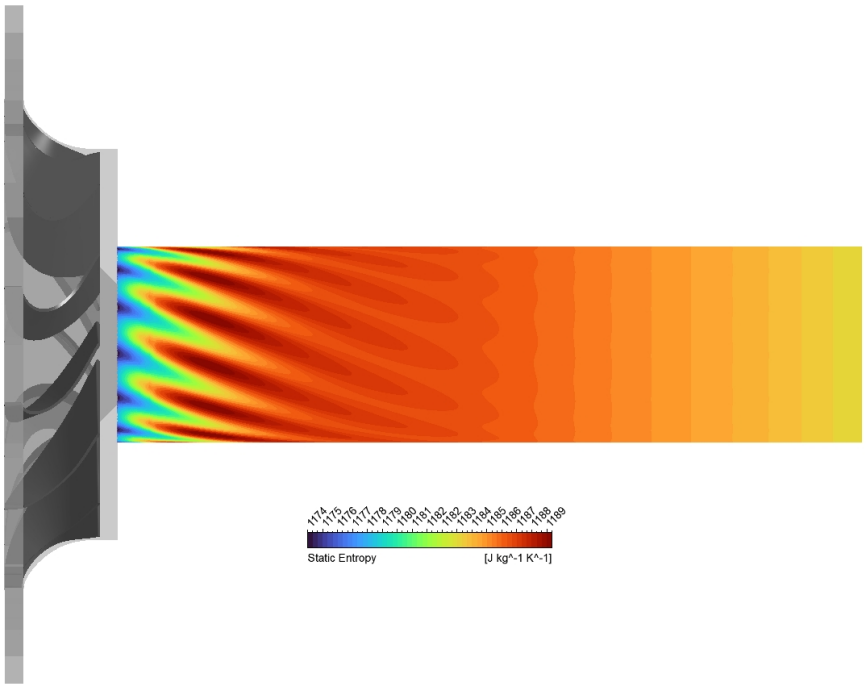

Figure 3.11: Entropy contours on a constant-radius plane. The contours are referred to the local range considering only the outlet domain.

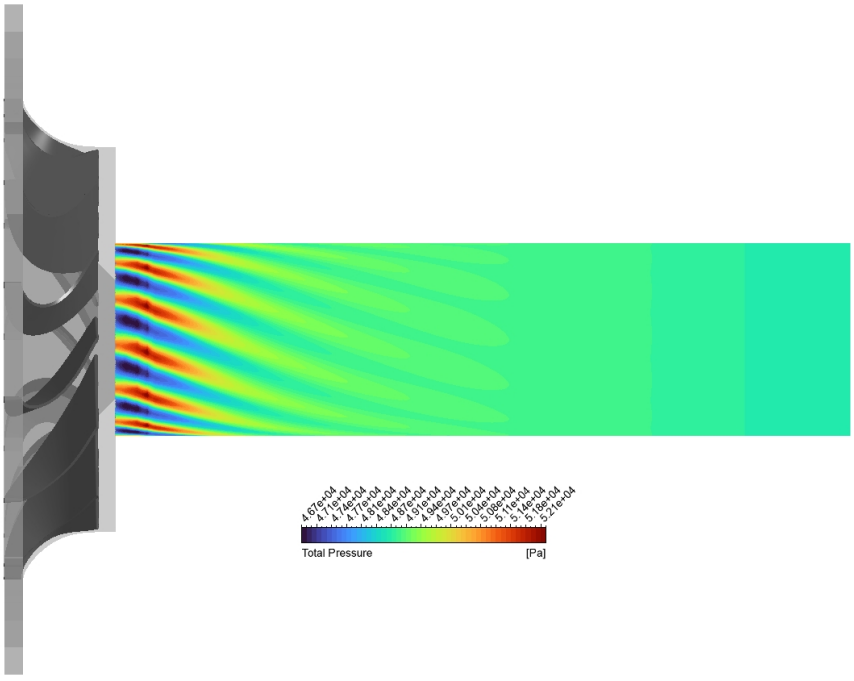

Figure 3.12: Total pressure contours on a constant-radius plane. The contours are referred to the local range considering only the outlet domain.

3.2 Solution dependence to different outlet boundary models

To ensure that the flow features observed in the outlet channel are not influenced by the imposed downstream boundary condition, a verification study on outlet boundary condition independence was carried out.

Additional simulations were performed to analyze different boundary conditions at the outlet with the objective of verifying whether the flow circumferential non-uniformities and wake structure evolution are affected by different outlet treatments.

The two outlet boundary conditions considered are:

1. a fixed outlet static pressure condition;
2. an opening boundary condition.

In the fixed outlet static pressure condition, the value of the static pressure is imposed at the outlet boundary, allowing the solver to determine the velocity field and mass flow rate that corresponds to this prescribed value. If this boundary is selected, the solver enforces outflow by erecting artificial walls on those faces where the flow attempts to enter the domain. This condition is adopted when the downstream pressure is known or reasonably assumed [21]. However, it can influence the upstream solution if applied too close to the region of interest.

The opening boundary condition allows both inflow and outflow across the boundary. Here, the static pressure value at the domain exit is required as a reference, making it a less intrusive boundary condition. In fact, if during the course of the simulation the flow is directed out of the domain, the value is treated as a static pressure. Conversely, if the flow is entering the domain, the value is taken as a total pressure, from which the static pressure is calculated [21]. This formulation is suitable for situations in which minimizing constraints on the solution is desirable.

For these simulations, the numerical setup of the baseline configuration previously described was maintained unchanged. The only difference between the two analysis consists in the replacement of the pressure outlet with an opening boundary condition.

Figure 3.13 reports contours of total pressure and entropy obtained with the opening condition. The results show that the spatial extent of the wakes and the level of circumferential non-uniformity in the outlet channel remain nearly unchanged with respect to the pressure outlet case (see Figure 3.11 and Figure 3.12). This indicates that the pressure outlet condition does not affect the flow field in the region of interest, and can therefore be retained for subsequent analyses.

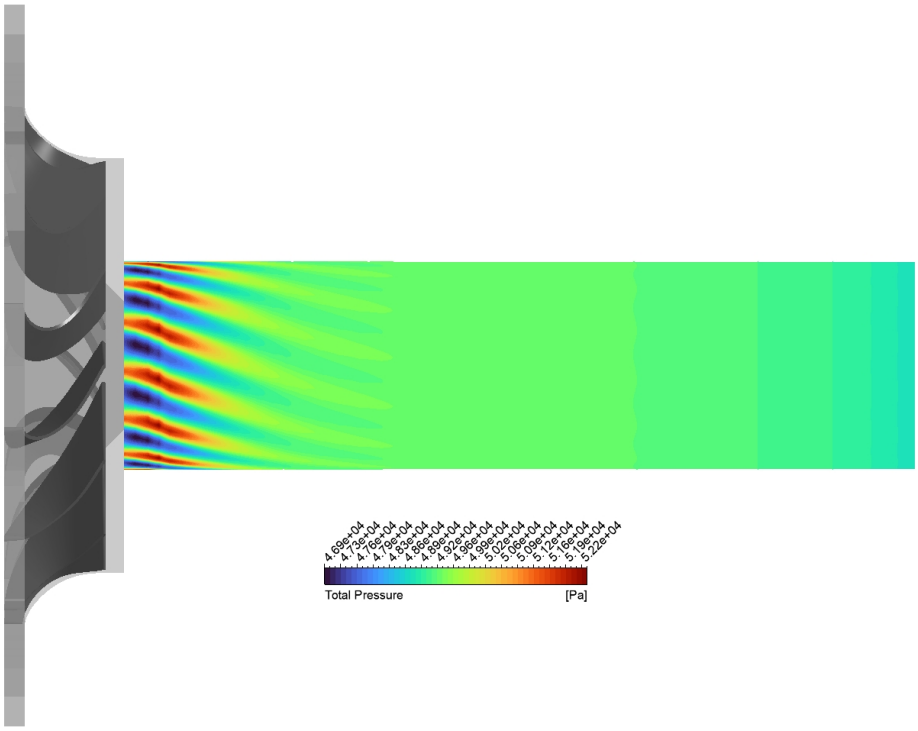

(a) Total pressure contours

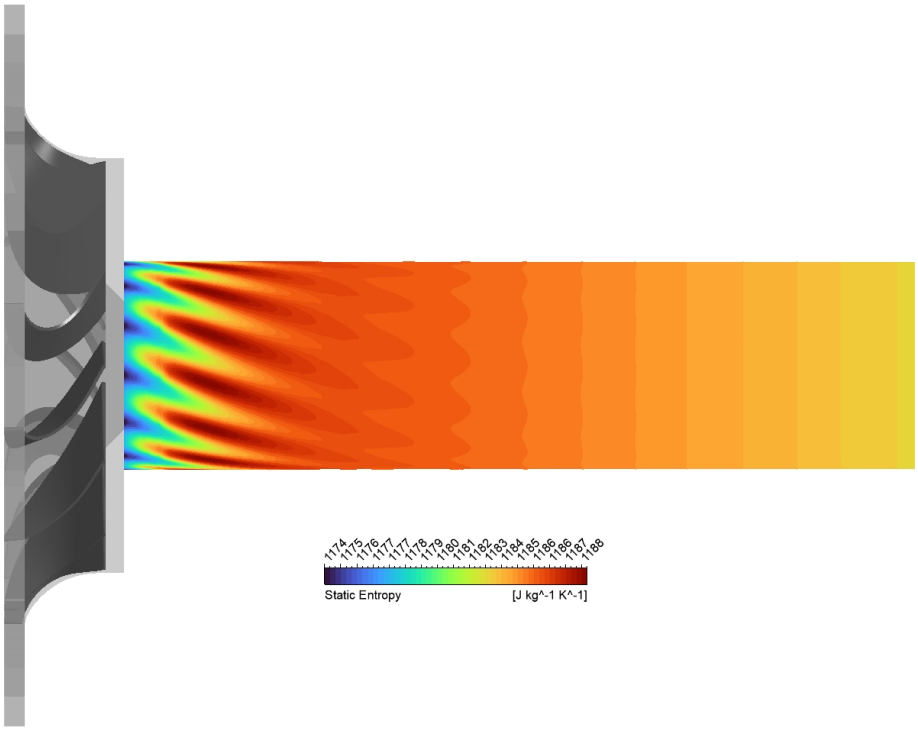

(b) Entropy contours

Figure 3.13: Flow field obtained with opening boundary condition at the outlet. The persistence and spatial extent of wakes and circumferential non-uniformities are comparable to the pressure outlet case.

As a further verification of the independence of the flow field from the outlet boundary condition, an additional simulation was performed by further extending the length of the outlet duct from 90 to 120 mm. A new mesh was generated following the same criteria adopted for the baseline configuration, while the numerical setup was kept unchanged with respect to the reference case, including the use of a pressure outlet boundary condition.

The results obtained from are shown in Figure 3.14: compared to the baseline configuration (see Figure 3.11 and Figure 3.12), the elongated duct shows a slightly delayed attenuation of the wake structures, however, at the axial location corresponding to the candidate measurement section, the wake structures are already fully mixed and the circumferential variations of both total pressure and entropy are negligible.

It is possible to conclude that the outlet boundary position does not significantly affects the flow field in the channel.

Therefore, the original outlet configuration was retained for all subsequent simulations, as neither the opening condition nor a further extension of the outlet duct provides additional benefits for the objectives of the present study.

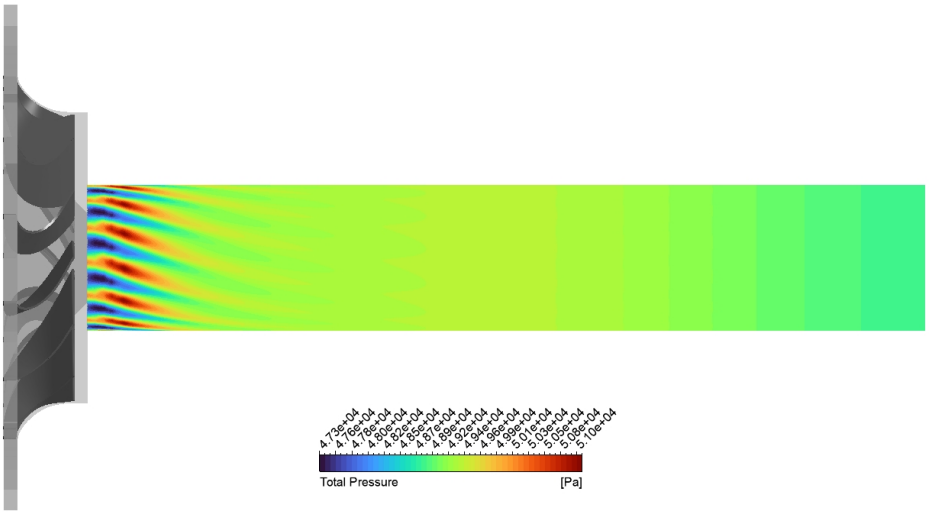

(a) Total pressure contours

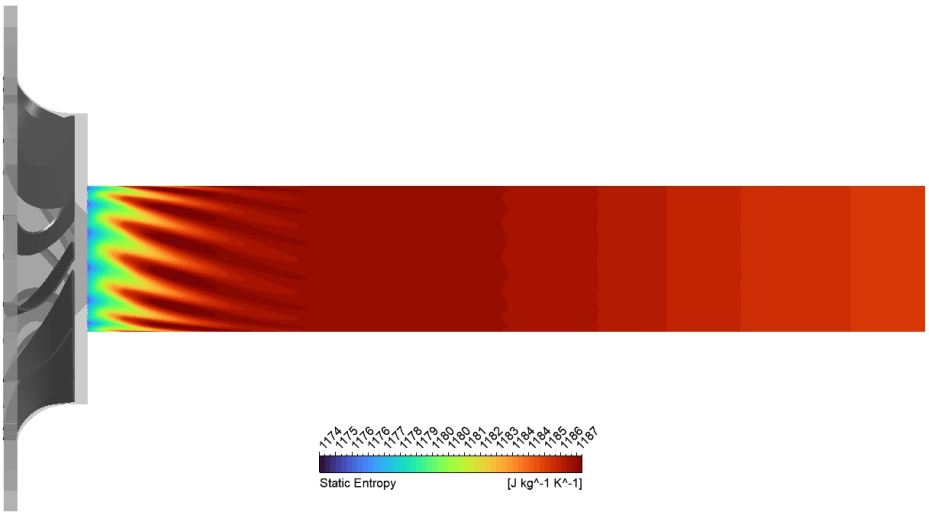

(b) Entropy contours

Figure 3.14: Flow field obtained with elongated outlet channel. The persistence and spatial extent of wakes and circumferential non-uniformities are comparable to the pressure outlet case.

3.3 Mesh Sensitivity Study

A mesh sensitivity analysis was carried out to quantify the discretization error associated with the spatial resolution of the computational grid. The objective of this analysis is to assess whether the numerical solution is sufficiently independent of the mesh size, and to provide an estimate of the remaining discretization uncertainty. In the present work, the analysis is performed using the Richardson extrapolation method, following the framework described by Phillips and Roy [23].

3.3.1 Richardson Extrapolation Method

Richardson extrapolation is based on the assumption that, in the asymptotic convergence range, the discretization error of a numerical solution can be expressed as a power law of the grid spacing. Considering a generic quantity of interest u computed on a mesh with characteristic grid spacing h, the discretization error can be written as

$$e_h = u_h - \tilde{u} \approx Ch^p, \tag{3.3}$$

where $\tilde{u}$ denotes the exact solution of the governing equations, C is an unknown constant, and p is the formal order of accuracy of the numerical scheme.

In practice, Richardson extrapolation requires a family of three systematically refined meshes, typically referred to as coarse (3), medium (2), and fine (1). The grids must be related by a constant refinement factor

$$r = \frac{h_2}{h_1} = \frac{h_3}{h_2}, \tag{3.4}$$

with $r > 1$. As recommended in the literature, values of $r > 1.1$ are preferred in order to reduce the influence of non-discretization-related numerical errors and to improve the reliability of the extrapolation [23].

After defining the three meshes, the values of the quantity of interest were computed on them and used for the Richardson extrapolation procedure.

The first indicator of statistical convergence is the convergence ratio, expressed as

$$R = \frac{u_3 - u_2}{u_2 - u_1}. \tag{3.5}$$

A value of $R > 1$ means that the difference between solutions in successive meshes decreases with refinement, and indicates convergence in the asymptotic range.

Using the three-grid solution set, the observed order of convergence $\hat{p}$ can be estimated as

$$\hat{p} = \frac{\ln\left(\frac{u_3 - u_2}{u_2 - u_1}\right)}{\ln(r)}. \tag{3.6}$$

For a verified numerical solution in the asymptotic range, the observed order of convergence is expected to be close to the formal order of accuracy of the discretization scheme.

The use of Richardson method is reliable only if the observed solution behavior falls within the asymptotic convergence range. This assumption can be assessed by verifying that

$$R \approx r^{\hat{p}}. \tag{3.7}$$

If this condition is met, then the Richardson extrapolation applies correctly.

Under these assumptions, the discretization error on the fine mesh can be estimated as

$$e_1 = \frac{u_2 - u_1}{r^{\hat{p}} - 1}, \tag{3.8}$$

and the extrapolated solution is obtained as

$$u_{\text{ext}} = u_1 + e_1. \tag{3.9}$$

Finally, the discretization uncertainty is commonly quantified using the Grid Convergence Index (GCI), defined as

$$\text{GCI}_1 = F_s \frac{|e_1|}{|u_1|}, \tag{3.10}$$

where F_s is a safety factor, typically equal to 1.25 when three grids are available and the observed order of convergence is close to the formal one.

The choice of an appropriate metric is a crucial aspect in the application of the Richardson Extrapolation Method. As discussed in detail in [23], the method is strictly valid when applied to global flow quantities, whereas local variables typically exhibit slow and non-monotonic convergence behavior. In particular, quantities defined at a single point or over a very limited spatial region are strongly affected by local discretization errors and may not reach the asymptotic convergence range even for relatively fine grids. For this reason, the use of local quantities is generally discouraged within the Richardson Extrapolation Method framework.

To ensure the validity of the extrapolation procedure, the present study adopts a strictly global quantity of interest. Given that the primary focus of this work is the characterization of total pressure non-uniformities downstream of the rotor, the selected metric is the mass-flow-averaged total pressure evaluated at the candidate measurement section located 60 mm downstream of the rotor trailing edge. This quantity is defined as

$$\overline{p}_t = \frac{\displaystyle\int_A p_t \, \rho \, \mathrm{u_n} \, \mathrm{d}A}{\displaystyle\int_A \rho \, \mathrm{u_n} \, \mathrm{d}A}, \tag{3.11}$$

where p_t denotes the local total pressure, $\dot{m}$ the local mass flow rate, and the integration is performed over the entire cross-sectional area of the measurement plane.

If the focus is on the interpretation of future experimental measurements, a more appropriated metric is represented by the radial profile of the total pressure at the test section. However, since this quantity is not properly global, it cannot be adopted

Table 3.1: Summary of the mesh family adopted for the mesh sensitivity study.

Mesh level	Element count [N]	Metric u $[Pa]$
Coarse	123000	50469,7
Medium	338256	50414,9
Fine	928174	50375,3

for the Richardson extrapolation method, but it is nevertheless used qualitatively in this study as a visual consistency check to ensure that it does not change significantly with mesh refinement.

3.3.2 Mesh Refinement

In order to apply the Richardson Extrapolation Method, a set of computational meshes was defined. The mesh set consists of three systematically refined grids, namely a coarse, a medium, and a fine mesh.

The meshes were generated by applying a uniform refinement strategy characterized by a constant refinement factor $r = 1.4$. The refinement factor r was defined based on the characteristic cell size. Since the computational grid is three-dimensional, this corresponds to an approximate ratio of r^3 between the total number of elements of two consecutive meshes. The grid refinement strategy was applied to the global mesh resolution by increasing or decreasing the number of elements, while the height of the first cell near the wall was kept unchanged for all the three meshes. This ensures consistency in the boundary layer resolution and in the y^+ values among the different grids.

For each mesh level, the total number of elements and the corresponding value of the selected quantity of interest were computed. Table 3.1 summarizes the main characteristics of the mesh family adopted for the mesh sensitivity study.

3.3.3 Results of the Mesh Sensitivity Study

The Richardson extrapolation method was applied to the selected quantity u by computing the convergence ratio R, the extrapolated solution u_{ext}, the absolute and relative discretization errors and the Grid Convergence Index (GCI) according to the procedure described in the previous section.

Table 3.2 summarizes the main results of the mesh sensitivity analysis.

The interpretation of the mesh refinement results is based on the distinction between the formal order of accuracy of the numerical scheme and the observed order of convergence. As stated in [23], the formal order of accuracy is determined by the chosen discretization scheme and corresponds to the exponent of the leading error term. If discontinuities or non-smooth solution are present, this order may be reduced.

In the present numerical setup, a high-resolution scheme combined with a blend factor of 0.5 is applied for the advection discretization. As stated in section 3.1.1, this factor controls the contribution between first-order upwind discretization and

Table 3.2: Results of the Richardson extrapolation applied to the selected quantity of interest.

Quantity	Value
Refinement factor r	1.4
Convergence ratio R	1.384
Observed order p	0.96
Theoretical r^p	1.4
Observed r^p	1.381
Extrapolated solution u_{ext} $[Pa]$	50272.43
Absolute error $[Pa]$	102.88
Relative error [%]	0.2
GCI [%]	0.25

higher-order schemes, therefore, with this value set to 0.5, one can expect a formal order of accuracy lower than the nominal second order. To be conservative, we can assume a reference formal order of $p = 1$ and, consequently, an observed order of convergence equal or lower than this. Assuming this, the theoretical r^p is equal to 1.4, while the observed r^p is 1.384. The convergence ratio R is found to be close to the observed r^p value, indicating a monotonic reduction of the discretization error as the mesh is refined. This confirms that the solutions lie within the asymptotic convergence range so Richarson Extrapolation Method is applicable.

The estimated relative discretization error on the quantity of interest is approximately 0.2%, which is considered acceptable for the objectives of the present study. These results indicate that the selected quantity of interest is effectively independent of the mesh resolution within the investigated range.

For completeness, a qualitative assessment of mesh sensitivity was also performed by inspecting the radial profiles of total pressure at the measurement section. Although this quantity is not strictly global and was therefore not used to drive the Richardson extrapolation, it provides useful insight into the expected experimental measurements.

Figure 3.15 shows the radial distribution of total pressure obtained with the three mesh resolutions. The profiles are very similar and tend to collapse as the mesh is refined, confirming the limited influence of grid resolution on both the mean value and the spatial distribution of total pressure.

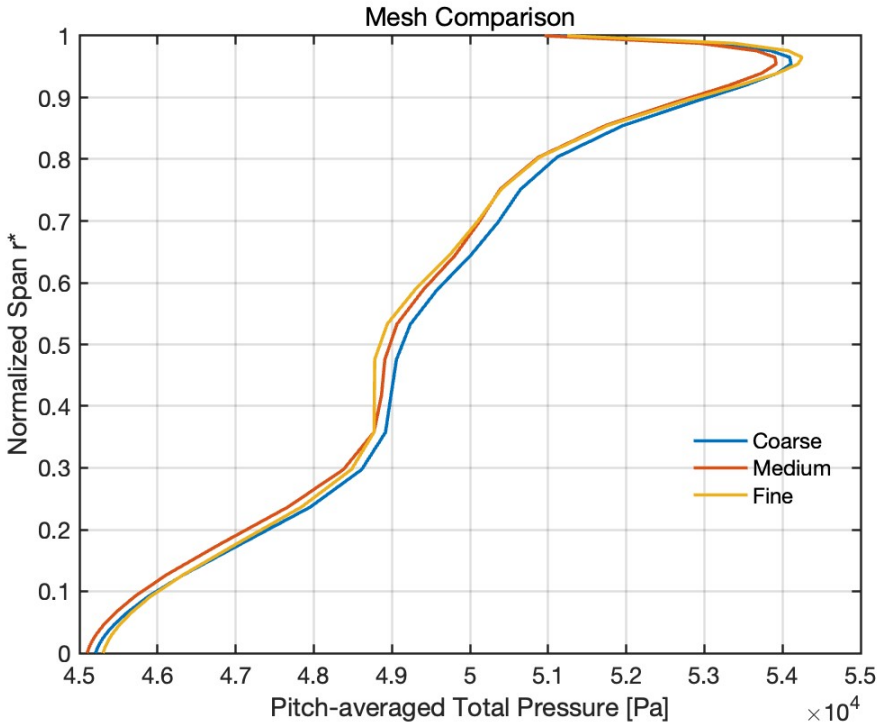

Figure 3.15: Radial profiles of total pressure at the candidate measurement section obtained with the coarse, medium, and fine meshes.

Chapter 4

Results

This chapter discusses the analysis of the results obtained from the CFD simulations, which were further post-processed to derive information and trends useful to guide the definition of the experimental measurement strategy and system design.

In the following sections the study of flow non-uniformities, angle and off-design operating points is presented.

4.1 Flow Non-Uniformity Analysis

The objective of the present non-uniformity study is to quantify the level of pitch-wise (i.e. circumferential) flow non-uniformity within the outlet channel downstream of the rotor. This analysis is performed both at different axial locations and along the radial direction, with the aim of assessing the spatial persistence of flow non-uniformities and their potential impact on the experimental measurements.

In order to do this, the pitch-wise non-uniformity index introduced by Cappiello and Tuccillo [24] was adopted as a quantitative figure of merit. This index provides a scalar measure of the circumferential non-uniformity of a generic flow quantity χ, and is defined as the pitch-averaged absolute deviation from the mean value, normalized by the angular pitch:

$$\mathrm{U}_\chi = \frac{1}{\Delta\theta_{\mathrm{pitch}}} \int_0^{\Delta\theta_{\mathrm{pitch}}} \frac{|\chi(\theta) - \overline{\chi}|}{\overline{\chi}} \, \mathrm{d}\theta, \tag{4.1}$$

where θ is the circumferential coordinate, $\Delta\theta_{\mathrm{pitch}}$ is the angular pitch of the periodic sector, and $\overline{\chi}$ denotes the pitch-averaged value of the quantity of interest.

In the present study, the non-uniformity index was evaluated for the total pressure and the entropy fields and expressed as a percentage, in order to provide a more readable and comparable parameter. This percentage is obtained by multiplying the non-uniformity index by 100, without introducing a normalization with respect to a reference value. The resulting quantitative assessment of pitch-wise non-uniformities is instrumental in estimating the expected variability of the measured quantities and, consequently, in supporting the selection of the most appropriate probe technology for the experimental campaign.

4.1.1 Axial Non-Uniformity

The axial evolution of pitch-wise non-uniformity was assessed by keeping the radial position fixed and varying the axial coordinate along the outlet duct, from the rotor exit up to the duct outlet. Using the `.csv` data exported from the results file (mid-radius surface distributions of total pressure, entropy, and spatial coordinates), a dedicated MATLAB[25] script was developed to: (i) extract the pitch-wise distributions at a set of axial stations, (ii) shift each distribution to a common mean value for improved visualization of the oscillations, and (iii) compute the non-uniformity index.

Figure 4.1 reports the pitch-wise total pressure signal at six axial locations and the corresponding non-uniformity index as a function of the axial coordinate. Similarly, Figure 4.2 shows the same analysis performed on entropy.

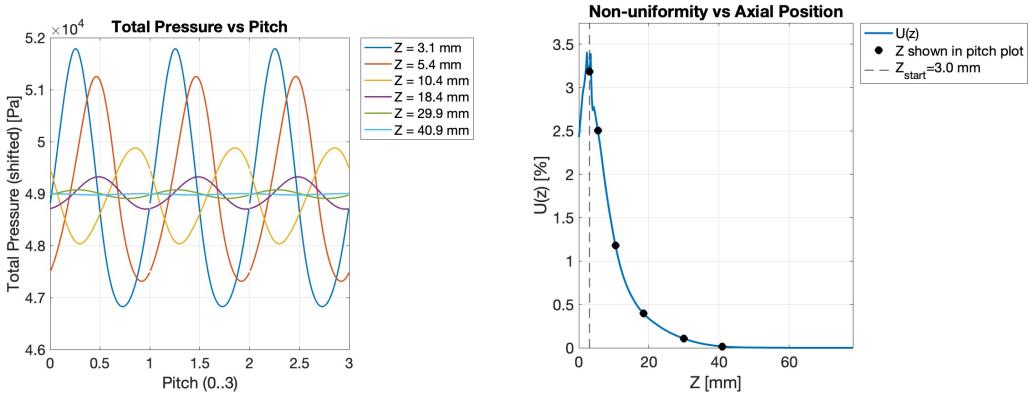

(a) Pitch-wise total pressure oscillations at different axial locations (shifted to a common mean for visualization).

(b) Axial evolution of the total-pressure non-uniformity index $U(z)$.

Figure 4.1: Axial non-uniformity analysis for total pressure at mid-radius.

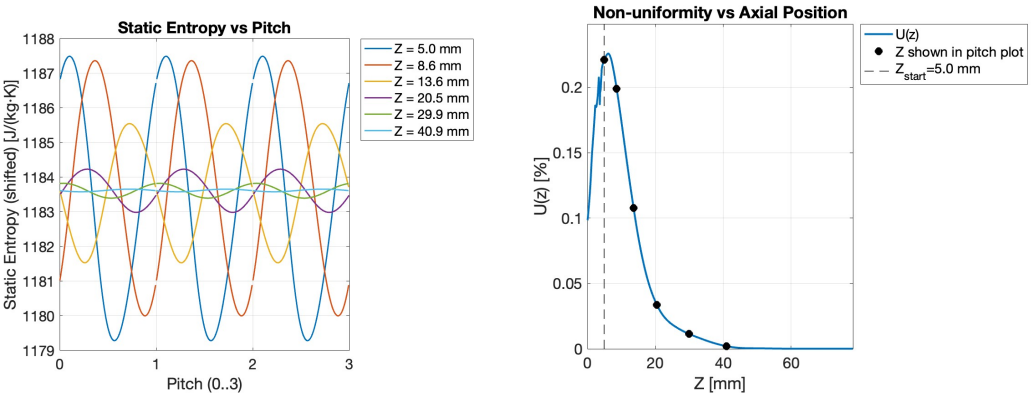

(a) Pitch-wise entropy oscillations at different axial locations (shifted to a common mean for visualization).

(b) Axial evolution of the entropy non-uniformity index $U(z)$.

Figure 4.2: Axial non-uniformity analysis for entropy at mid-radius.

For both total pressure and entropy, the pitch-wise oscillations progressively flatten as the flow convects downstream, indicating a rapid attenuation of the circumferential non-uniformities generated at the rotor exit.

Consistently, the non-uniformity index decreases with increasing axial distance. The region upstream of the dashed line is not considered representative, as it is affected by the frozen-rotor interface and may artificially distort the non-uniformity estimate (apparent local increase). Beyond this region, $U(z)$ decays monotonically and becomes nearly zero at the candidate measurement plane located 60 mm downstream of the rotor.

Therefore, at the measurement location the pitch-wise non-uniformity in both total pressure and entropy is essentially negligible, and the corresponding pitch-wise distributions are almost flat.

4.1.2 Radial Non-Uniformity

The radial non-uniformity analysis was conducted to assess the pitch-wise variability of the flow quantities as a function of the radial position at fixed axial locations. Two axial sections were considered: one located close to the rotor outlet, at $z = 20$ mm, and a second one corresponding to the measurement section at $z = 60$ mm.

For each section, the analysis was performed by extracting total pressure data on circumferential surfaces at constant axial position from the CFD results. Similarly to the axial analysis, the flow quantities and spatial coordinates were exported in `.csv` format and post-processed using a dedicated script. The script was used to reconstruct the pitch-wise oscillations at different radial locations, shifted to a common mean for visualization purposes, and to compute the corresponding non-uniformity index U as a function of the radius.

For clarity and conciseness, only the results for total pressure are reported in the following, as the entropy field exhibited a qualitatively similar behavior.

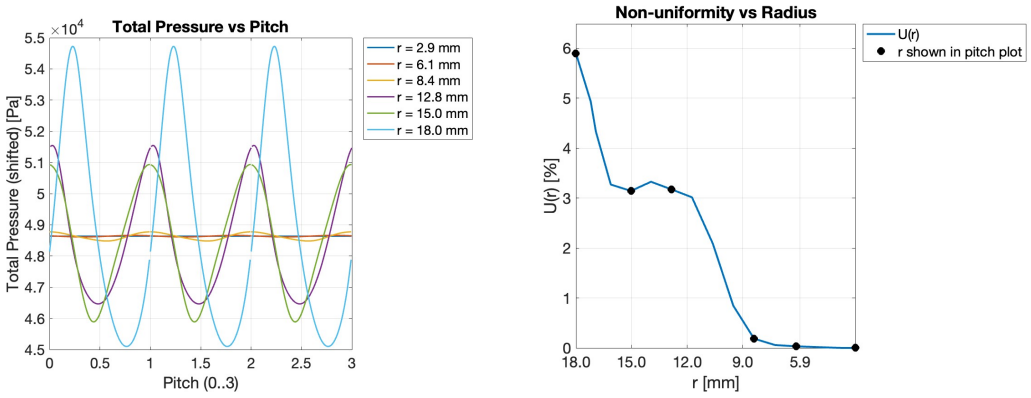

(a) Pitch-wise total pressure oscillations at different radial locations ($z = 20$ mm).

(b) Radial evolution of the total-pressure non-uniformity index $U(r)$ ($z = 20$ mm).

Figure 4.3: Radial non-uniformity analysis for total pressure close to the rotor outlet.

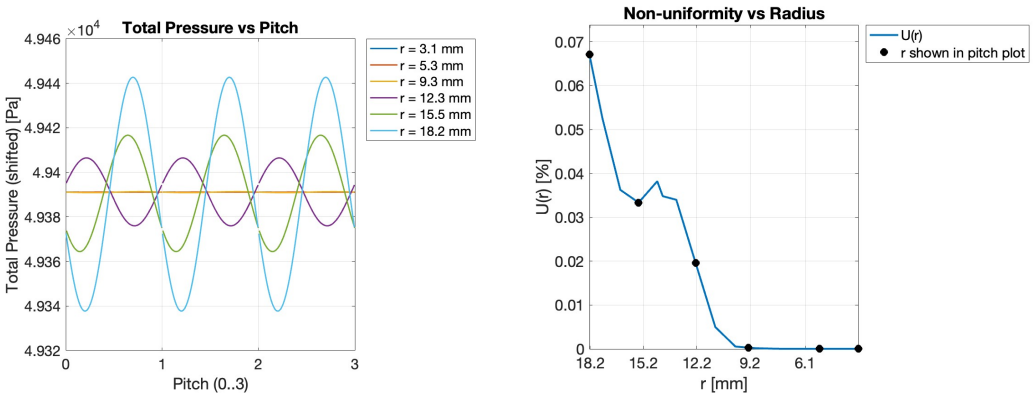

(a) Pitch-wise total pressure oscillations at different radial locations ($z = 60$ mm).

(b) Radial evolution of the total-pressure non-uniformity index $U(r)$ ($z = 60$ mm).

Figure 4.4: Radial non-uniformity analysis for total pressure at the candidate measurement section.

As shown in Figure 4.3, the section located close to the rotor outlet is characterized by pronounced pitch-wise oscillations of total pressure and by a quite high level of non-uniformity. The non-uniformity index reaches values approximately two orders of magnitude larger than those observed at the downstream measurement section, shown in Figure 4.4. In addition, the amplitude of the pitch-wise total pressure fluctuations is significantly larger, reflecting the direct imprint of rotor-induced wakes and flow non-uniformities. In both representations, a reduction of non-uniformity is observed when moving from the shroud region towards the channel centerline.

At the measurement section ($z = 60$ mm), as shown in Figure 4.4, the non-uniformity index is nearly negligible over the entire radial extent, and the total pressure variations relative to the mean value are extremely small. In particular, the maximum observed deviation of the total pressure from its mean value is $\Delta p_t^{\max} \approx 0.004$ Pa.

Conversely, the analysis performed at $z = 20$ mm downstream of the rotor highlights significantly higher levels of pitch-wise non-uniformity and total pressure fluctuations. Although this section is not selected for the present experimental campaign, it represents a more suitable location for future investigations of unsteady total pressure fluctuations.

The non-uniformity analysis was also repeated for the cases employing an opening boundary condition and an elongated outlet duct, showing no appreciable differences with respect to the reference pressure-outlet configuration.

4.2 Flow Angle Analysis

The analysis of the flow angles and their radial variation is essential to support the selection of the pressure probe and to define its optimal orientation during the experimental campaign.

Figure 4.5 shows the definitions and schematic representation of the pitch and yaw angles with respect to the probe axis and to the local reference planes of the cylindrical outlet channel.

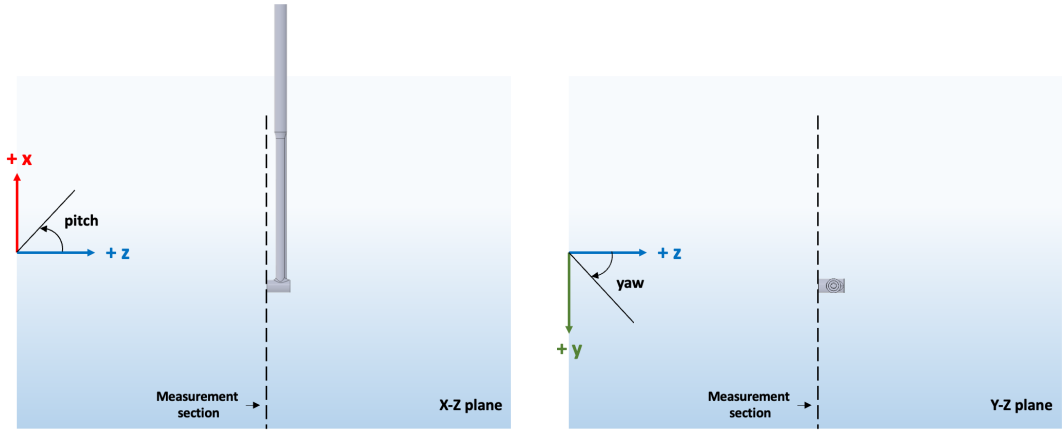

(a) Schematic representation of the pitch angle in the X–Z plane.

(b) Schematic definition of the yaw angle in the Y–Z plane.

Figure 4.5: Representation of pitch and yaw angles with respect to the probe axis and to the local reference planes of the cylindrical outlet channel.

Denoting by u, v, and w the velocity components along the x, y, and z directions, respectively, the two angles are computed as

$$\alpha_{\text{pitch}} = \arctan\left(\frac{u}{w}\right), \qquad \alpha_{\text{yaw}} = \arctan\left(\frac{v}{w}\right). \tag{4.2}$$

The flow angles were evaluated by exporting the velocity components u, v, and w on a surface normal to the Z axis, located at the measurement section. A dedicated script was developed to compute the pitch and yaw angles as a function of the radial position.

As shown in Figure 4.6, the pitch angle remains between $\pm 10°$ along the radial span, while the yaw angle shows a much larger variation, due to the swirl of the flow.

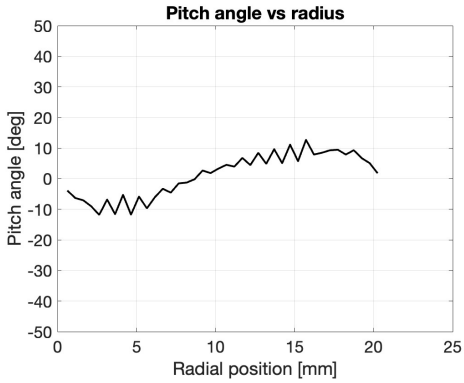

(a) Radial distribution of pitch angle at the measurement section.

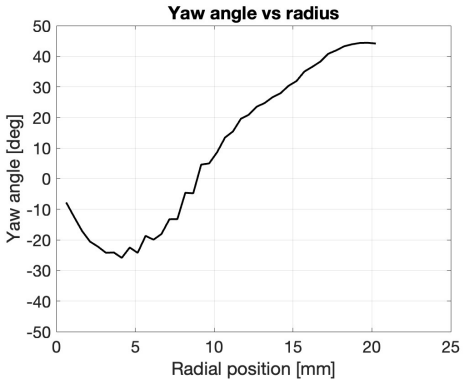

(b) Radial distribution of yaw angle at the measurement section.

Figure 4.6: Radial variation of pitch and yaw flow angles at the measurement section.

4.3 Off-Design Operating Points Analysis

In addition to the design operating point previously analyzed , a set of off-design operating conditions was considered in order to assess whether different flow regimes could give rise to enhanced circumferential non-uniformities or other features of relevance for experimental measurements.

The definition of the operating points follows the convention introduced in [2], and is reported in Table 4.1. The design point, corresponding to OP7, is characterized by a rotational speed of 98.1 krpm and a stator inlet total pressure of 18.1 bar.

Table 4.1: Operating points considered in the off-design analysis, following the nomenclature of Majer [2].

n [krpm]	P_{t0} [bar]			
	10.9	14.5	18.1	23.5
80.0	OP1	OP2	OP3	OP4
98.1	OP5	OP6	OP7	OP8
120.0	OP9	OP10	OP11	OP12

The objective of this analysis is to identify off-design conditions that may exhibit stronger wake persistence, increased pitch-wise non-uniformity, or other flow features requiring special attention when planning experimental measurements. To this end, a preliminary screening of off-design points was carried out using the baseline stator–rotor configuration with a short outlet section, prior to performing full outlet-channel simulations.

Starting from OP1, the inlet total pressure was progressively increased to analyze OP2, OP3, and OP4. For each operating point, the same non-uniformity analysis discussed before together with a qualitative inspection of the flow field were performed. As one can see from Table 4.2, which shows the maximum axial non-uniformity at mid-span for each operating point, among the cases at 80 krpm, OP4 ($P_{t0} = 23.5$ bar) seemed to be the most critical point.

Table 4.2: Maximum axial non-uniformity at mid-span for each operating point expressed as a percentage. The nomenclature refers to Majer [2].

n [krpm]	P_{t0} [bar]			
	10.9	14.5	18.1	23.5
80.0	0.013	0.06	0.42	2.5
98.1	0.224	0.11	3.4	5.67
120.0	0.28	0.34	0.8	12

Subsequently, operating points at the same inlet total pressure but higher rotational speeds were analyzed, namely OP8 and OP12. This preliminary investigation revealed that both cases exhibit higher non-uniformity levels than OP4. Although OP12 shows more intense wake structures in the immediate vicinity of the rotor, these structures were observed to mix out more rapidly than in OP8.

Based on these observations, OP4, OP8, and OP12 were selected for full simulations including the complete outlet channel, in order to further assess the downstream evolution of flow non-uniformities under off-design conditions.

For completeness the remaining operating points were also quickly analyzed, confirming that other cases were less critical than those identified (see Table 4.2).

4.3.1 CFD simulations of OP4, OP8 and OP12

A CFD simulation was performed for operating points 4, 8 and 12 using the same numerical setup, turbulence model, discretization schemes, and initialization strategy adopted for the design-point simulations.

Figure 4.7 reports a comparison of the total pressure in the outlet region of the analyzed off-design operating points. From a qualitative standpoint, one can notice that the wake structures generated at OP4 appear to attenuate more rapidly along the outlet duct compared to the other OPs, with a visibly smoother circumferential distribution already at short axial distances from the rotor.

For as regards OP8, the wakes originating from the rotor appear more elongated and persist further downstream. These structures may extend up to the measurement section, suggesting a potentially more critical operating condition with respect to pitch-wise non-uniformities.

Finally, in OP12 the wake structures are observed to decay more rapidly than in OP8, resulting in a faster attenuation of non-uniformities along the outlet duct.

To support these qualitative observations, both axial and radial non-uniformity analyses were carried out. Figure 4.8 shows the comparison of the axial and radial evolution of the total-pressure non-uniformity index in the analyzed operating points, including the on design point for reference (OP7). The corresponding entropy trend is similar and is not reported for brevity.

Both the axial and radial analyses confirm that the level of circumferential non-uniformity at OP4 is lower than that observed at the other OPs. The non-uniformity decays rapidly along the outlet duct and reaches negligible values already upstream of the measurement section.

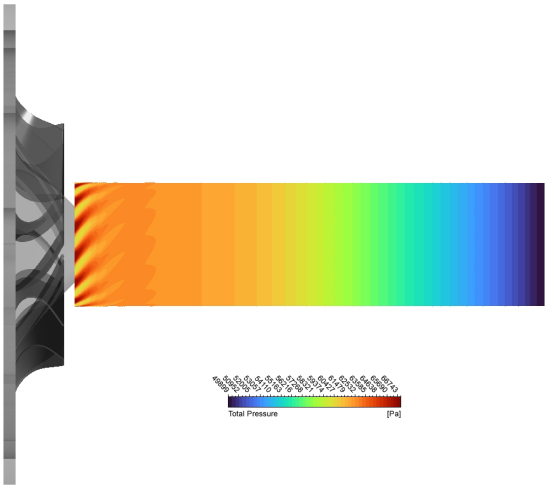

(a) OP4 total pressure contours.

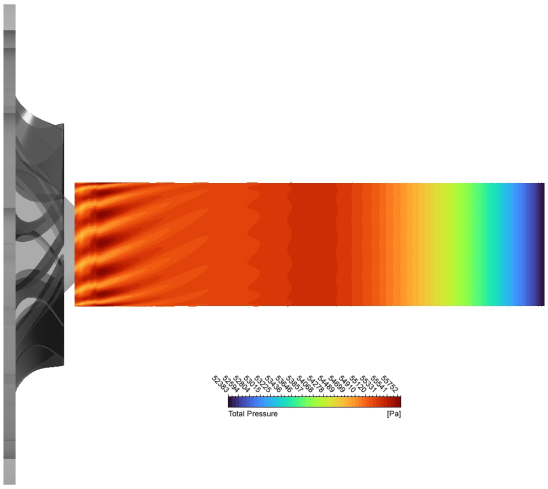

(b) OP8 total pressure contours.

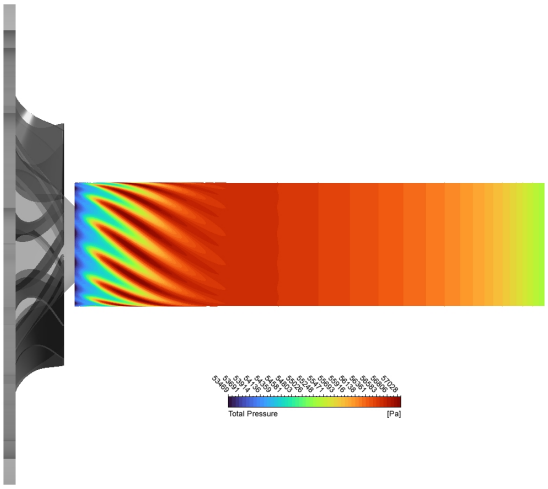

(c) OP12 total pressure contours.

Figure 4.7: Outlet total pressure contours for operating points OP4, OP8, and OP12.

For as concerns OP8, the level of non-uniformity is higher than that observed at the design operating point OP7. This confirms that OP8 represents a more challenging condition in terms of circumferential flow non-uniformities within the outlet channel.

In OP12 the level of non-uniformity is higher than that observed at OP7. Nevertheless, the non-uniformity attenuates more rapidly along the outlet channel than in OP8, confirming an intermediate behavior between the two operating conditions.

4.3.2 Flow Angle Analysis for Off-Design Operating Points

In this section, the flow-angle characteristics at the candidate measurement section are analyzed for the off-design operating points OP4, OP8, and OP12. The same definitions of pitch and yaw angles introduced in Section 4.2 are adopted, together with the same post-processing methodology.

For each operating point, the velocity components extracted from the CFD results at the measurement section were used to compute the pitch and yaw angles as a function of the radial position. The objective of this analysis is to assess how the flow-angle distribution varies across different operating conditions.

Figure 4.9 shows the radial distribution of pitch and yaw angles for the three operating points considered. In OP4, near the wall, it is possible to recognize regions where the flow proceeds in the opposite direction (red markers on the graph) as the axial velocity component w is negative. In OP8 the pitch angle is a range between -30° and 5°, while the yaw changes more along the radial direction. In OP12, as in the other cases, the pitch angle remains closer to zero than the yaw angle.

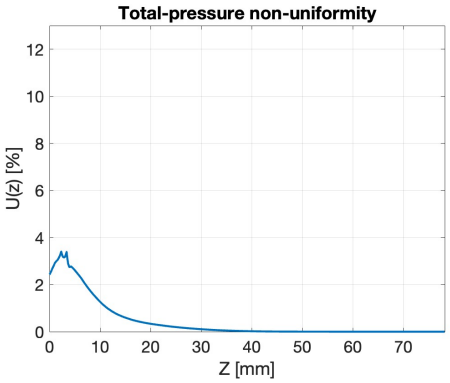

(a) Axial non-uniformity for OP7.

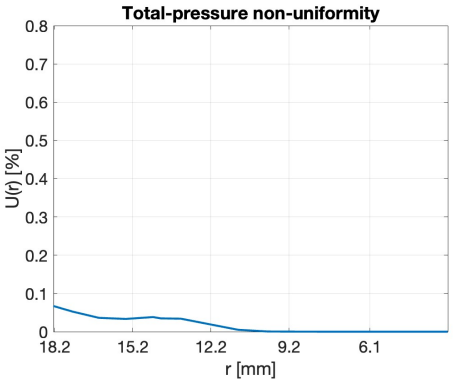

(b) Radial non-uniformity for OP7.

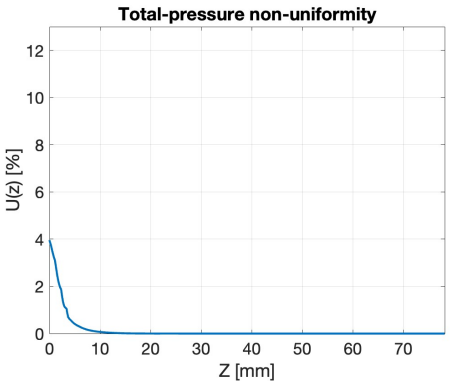

(c) Axial non-uniformity for OP4.

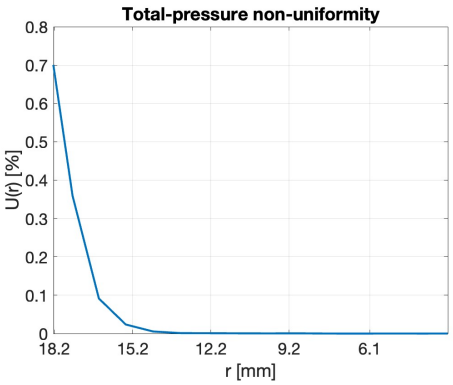

(d) Radial non-uniformity for OP4.

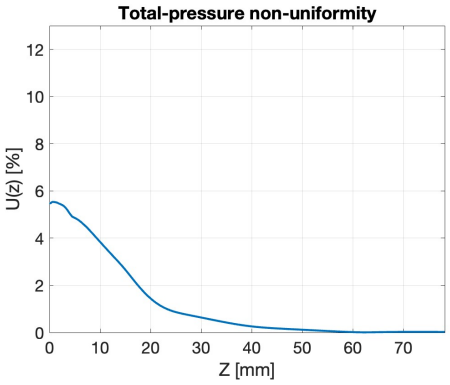

(e) Axial non-uniformity for OP8.

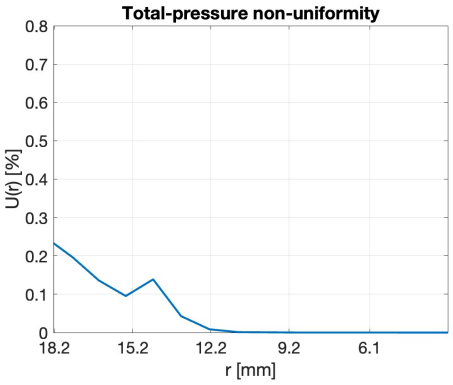

(f) Radial non-uniformity for OP8.

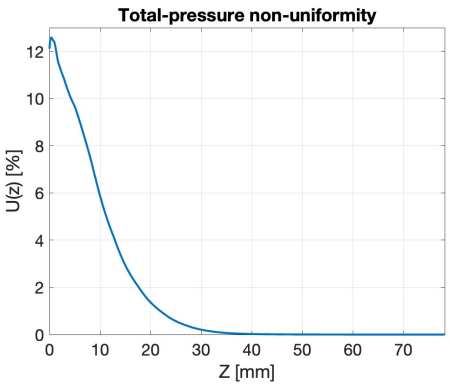

(g) Axial non-uniformity for OP12.

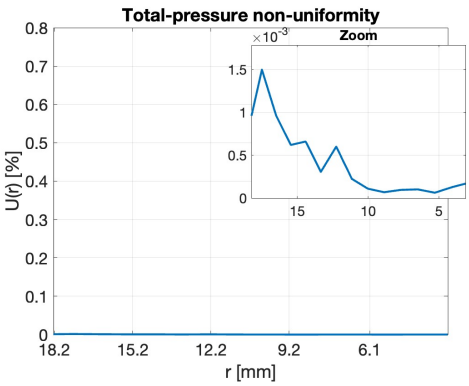

(h) Radial non-uniformity for OP12.

Figure 4.8: Axial and radial distributions of the total-pressure non-uniformity for OP7, OP4, OP8, and OP12.

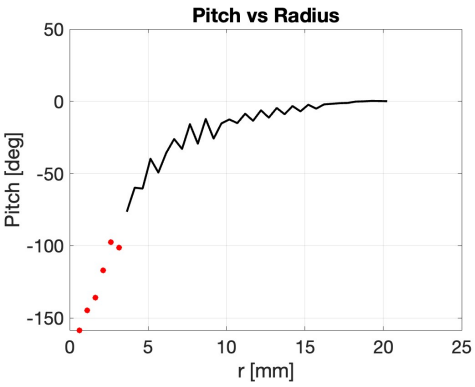

(a) OP4 Pitch angle.

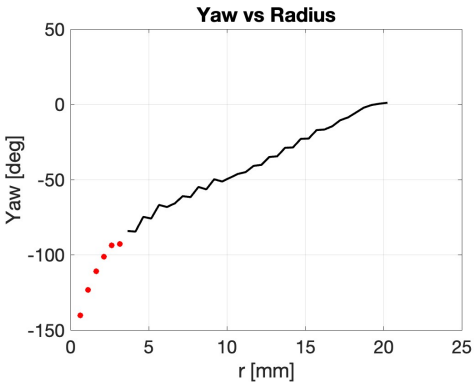

(b) OP4 Yaw angle.

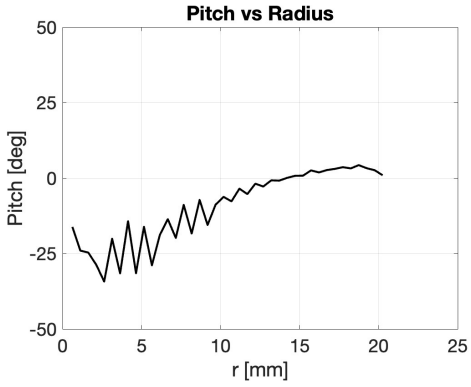

(c) OP8 Pitch angle.

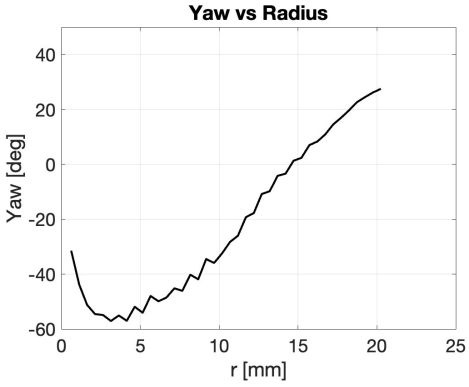

(d) OP8 Yaw angle.

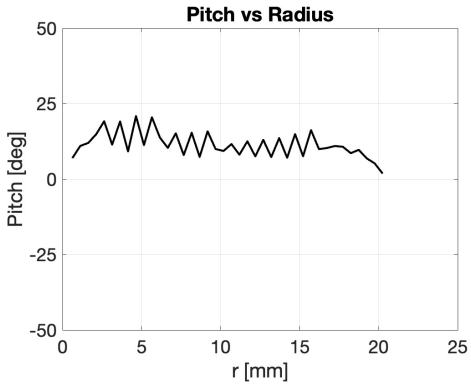

(e) OP12 Pitch angle.

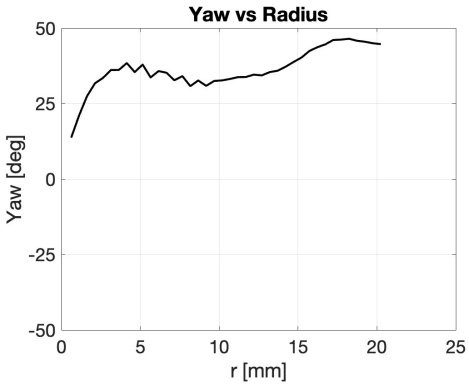

(f) OP12 Yaw angle.

Figure 4.9: Pitch and yaw angle distributions at the measurement section for OP4, OP8, and OP12.

Chapter 5

Measurement System Design

This chapter presents the design of the total pressure measurement system, explaining the reasons behind the probe selection and the choice of all components required for its operation, including the traversing mechanism, the pressure transducer and the sealing system.

5.1 Description of the Measurement Section

Geometry and location

The measurement section selected for this study and shown in Figure 5.1 is located 60 mm downstream of the rotor blade trailing edge, within the short cylindrical duct that connects the rotor to the diffuser. This channel is equipped with four ports for process connections allowing the installation of pressure and temperature probes.

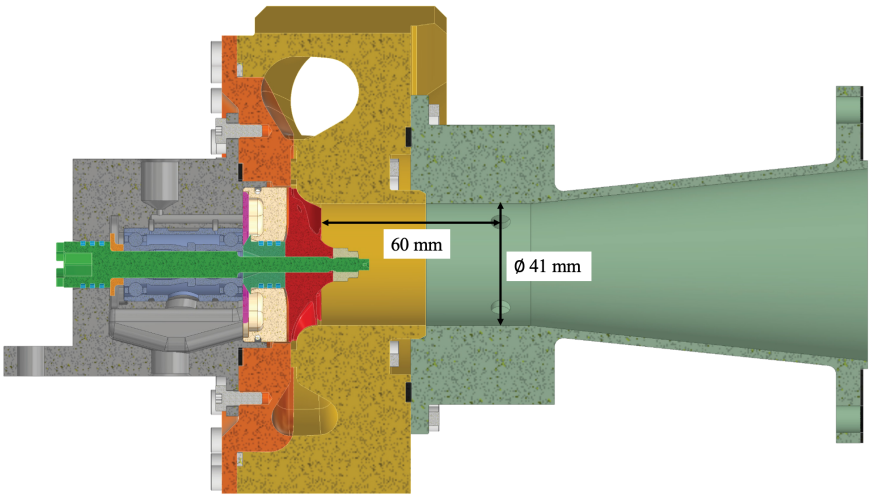

Figure 5.1: Section view of the ORCHID turbine highlighting the rotor outlet measurement section diameter and location. Adapted from [2]

Thermodynamic conditions

In the selected measurement section, a static pressure of approximately 0.44 bar and a static temperature of approximately 249 °C is expected, based on CFD analysis. It can be assumed that given these thermodynamic conditions, the working fluid is a perfect gas, so the thermodynamic effects due to non-ideality are neglected in this discussion.

This statement is supported by the reduced temperature-entropy diagram of Siloxane MM represented in Figure 5.2. The plot shows the isentropic expansions for four different operating points namely A, B, C and D corresponding to four different inlet total pressure, respectively 10.9 bar, 14.5 bar, 18.1 bar and 23.5 bar [2]. The contours of compressibility factor Z are reported as an indicator for the thermodynamic behavior of the gas and its distance from ideal gases as explained in Section 2.1.

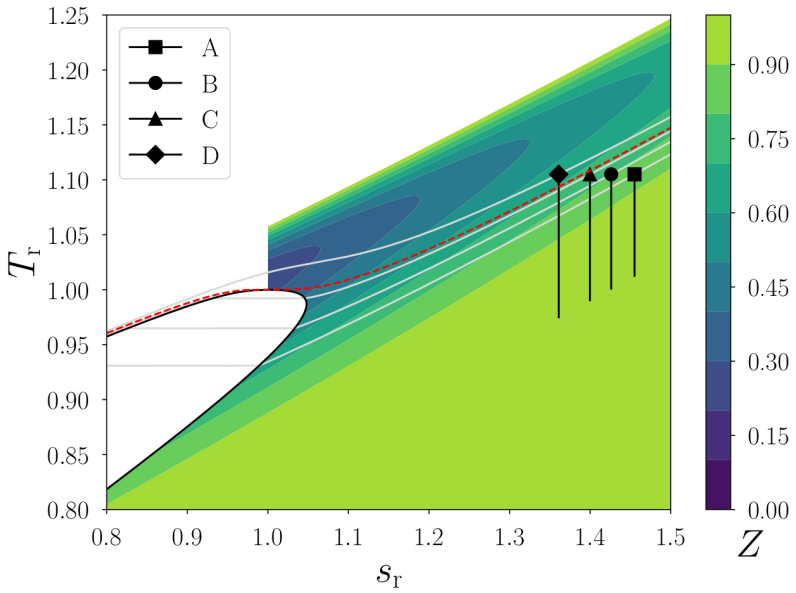

Figure 5.2: Reduced temperature–entropy diagram of Siloxane MM showing expansion precesses A, B, C and D. The reduced temperature and entropy are defined as $T_r = T/T_{cr}$ and $s_r = s/s_{cr}$, where the reference condition is the vapor liquid critical point. The red dashed line indicates the critical isobar. Adapted from [2]

All four operating points lie within a Z range close enough to 1 to consider an ideal-flow condition.

This assumption represents a significant simplification, particularly for the pressure probe calibration process. In this thermodynamic regime, it is possible to follow the standard calibration provided by probe suppliers, without the need to correct or repeat the process in non-ideal fluid.

Flow characteristics at the measurement plane

As discussed in detail in Chapter 4, the CFD simulations performed provide an overview of the flow field at the rotor outlet, including the behavior at the measurement section. Here, the flow exhibits an almost negligible circumferential non-uniformity, with no visible wake structures.

However, the flow maintains a strong residual vortex inherited from the flow angle at the rotor outlet and a significant radial variation in the flow angle.

5.2 Probe Selection

The most critical and delicate part of designing a reliable and accurate measurement system is undoubtedly the selection of a suitable probe. The following sections provide an overview of the main options that were considered during the selection process.

5.2.1 Remote Probes

One of the most reliable and widespread technology for measuring total pressure in turbomachinery are pneumatic probes, also known as remote probes. This name is derived from the fact that pressure is sensed locally on the probe head, but the transducer is located outside the flow and connected to it through a pneumatic line. This technique is widely documented in literature, and this study takes into consideration several of these classic and modern studies [26, 27, 28].

It's precisely this separation between the sensing point and the transducer that allows the sensor to operate in a thermally and mechanically non-hostile environment. This is one of the major advantages of this type of probe since it makes them particularly suitable for use in high-temperature flows, harsh operating conditions and confined spaces[26].

Moreover, since the probe head does not incorporate the sensor, its dimensions can be highly reduced, allowing spatially resolved measurements with low flow blockage.

The finite volume of the pipe line and of the transducer introduces a filtering effect that dampens high-frequency fluctuations [29], which are consequently not detected. For this reason, pneumatic probes provide a measurement of the average total pressure over time. Although this limits their application for dynamic measurements or where frequency resolution is required, it is generally acceptable, and often preferable, when the objective is the characterization of average flow quantities.

In order to avoid any compromise to the accuracy of measurements taken using these probes, it is necessary to take into account and properly manage response time and latency, which depend on the length and diameter of the pneumatic tube and the volume connected to the transducer.

Single-hole probes: Pitot and Kiel

Single-hole pneumatic probes are the simplest type of total pressure measurement devices. The classic Pitot probe consists of a tube directed upstream, in which the flow is slowed down until it stops, allowing the stagnation pressure to be measured [26, 27].

One of the main limitations of this type of probe is the need to align it with the flow direction, due to the high probability of errors caused by an asymmetrical pressure distribution on the probe head [28]. As one can see in Figure 5.3, the magnitude of this error strongly depends on the probe head geometry. In particular, the diagram shows typical yaw insensitive range for various head geometries, pointing out that some configurations are less affected by flow misalignment.

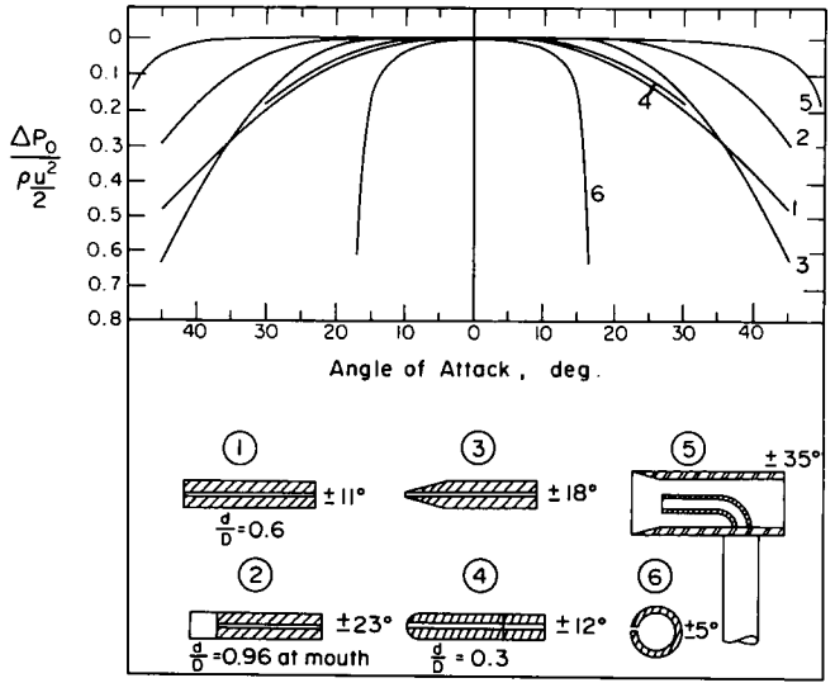

Figure 5.3: Yaw insensitivity range for various head geometries, showing the variation of total pressure error with flow angle. Adapted from [28].

Referring back to the Figure 5.3, it is possible to notice how the probe with a Kiel head (indicated with 5 in the image) manages to reduce the directional sensitivity of conventional Pitot probes. In this configuration, the Pitot tube is surrounded by a cylindrical shroud with a converging edge that induces the flow to realign in the axial direction with respect to the inner tube. [27, 28].

Thanks to this shroud, Kiel probes have a much wider yaw insensitivity range (up to $\pm 45°$ for optimized models) [28] and are particularly suitable for applications where the flow direction is unknown or varies significantly in space.

The higher misalignment tolerance of Kiel probes compared to other total-pressure probe geometries is remarked again in Figure 5.4, where the decay of measured total pressure due to an increasing yaw angle is reported for several head shapes.

The Kiel probe maintains a nearly constant total-pressure over a much wider angular range than other Pitot probes.

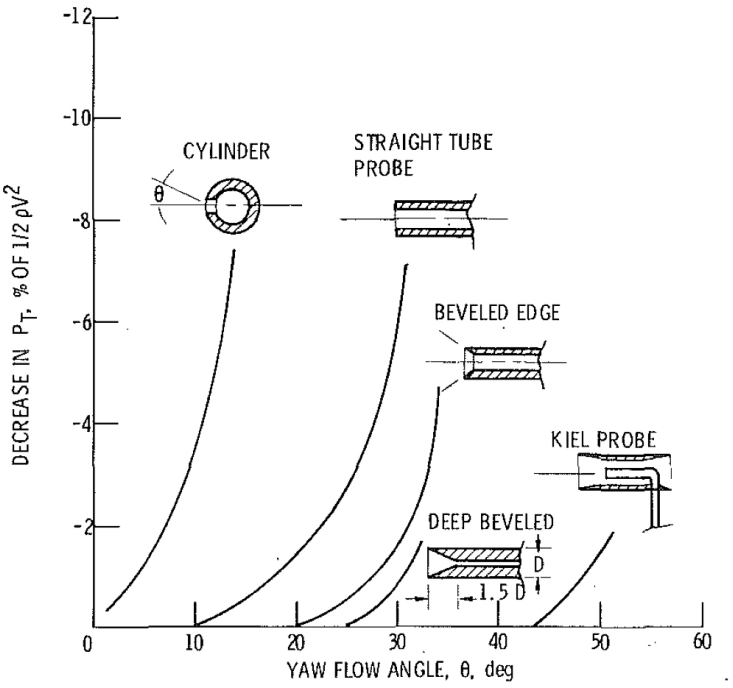

Figure 5.4: Total pressure decrease as a function of yaw angle for different probe geometries, highlighting the higher yaw insensitivity of Kiel probes. Adapted from [26].

Kiel probes, like all remote probes, measure an average quantity and may be subject to displacement errors in presence of strong pressure gradients. However, these effects are generally minimal, making Kiel probes a robust and reliable choice for average total pressure measurements in turbomachinery flows. [27, 28].

Multi-hole probes

Compared to single-hole probes, multi-hole pneumatic probes allow the reconstruction of the average local vectorial flow field, giving also information on the direction. This is achieved by reading the differential pressure from multiple ports (typically four, five or seven in classic models) distributed across the probe head, which is usually conical or pyramidal. This configuration allows the simultaneous determination of total pressure, static pressure and local flow direction, typically expressed in terms of yaw and pitch angles. [26, 27].

The proper use of multi-hole probes is strictly related to their preliminary calibration, during which the pressure distribution between the ports is mapped according to known flow angles and pressure levels in a reference flow. During measurements, the derived calibration maps are used to deduce unknown flow quantities by data interpolation. On one hand, this approach allows for the reconstruction of the complete velocity vector, which remains unknown when using a single hole, but on the other

hand, it makes the technique intrinsically dependent on calibration. This results in higher sensitivity to variations between calibration and operating conditions, in terms of Reynolds number, turbulence, compressibility, and type of working fluid [29, 30].

Given the ability of multi-hole probes to provide a richer set of flow information, they are very attractive when detailed investigations of the flow field are required, particularly when optical techniques are not feasible. This comes at the cost of greater sensitivity to flow misalignment, pressure gradients and unstable incidence. In fact, the accuracy of the total pressure measured tends to decrease as the local flow angle increases, since the contribution of the side ports becomes dominant and the post processed reconstruction is increasingly based on non-linear calibration [28, 31].

When compared directly to Kiel probes, multi-hole probes are not optimised for conditions involving high flow angles, strong gradients or instability. As a result, the uncertainty associated with total pressure measurements obtained from such probes can be significantly higher than that of a Kiel probe, even when state-of-the-art calibration strategies are employed [31].

Another limitation of multi-hole probes is related to spatial resolution and blocking effects. In fact, the presence of multiple pressure ports distributed across the probe head involves both a larger probe size and lower spatial resolution, since these ports are placed at a finite distance apart and measure in slightly different locations. To mitigate these effects, which are mainly due to the size of the head and the proximity of the ports, miniaturised multi-hole probes have been designed in order to offer better resolution and reduced flow disturbance, at the expense of increased manufacturing complexity [30, 32].

5.2.2 Fast Response Aerodynamic Pressure Probes

Fast response aerodynamic pressure probes (FRAPs) overcome the limitations of pneumatic probes in terms of dynamic response, providing a rapid frequency response when applied to highly unsteady flows exhibiting, for example, pressure fluctuations at the blade passing frequency [26, 29].

This result is achieved by placing fast-response pressure transducers directly inside the probe head, close to the point of pressure detection. The sensing element is typically a piezoresistive or piezoelectric silicon membrane, whose electrical output reflects the instantaneous pressure exerted on the sensor. Unlike remote probes, the absence of long pneumatic lines allows FRAPs to guarantee a frequency response in the order of tens of kilohertz, capturing pressure oscillations around the average value [33, 34].

Frequency-resolved measurements enable the study of stator-rotor interaction, periodic instability and wake structures evolution. However, achieving this higher temporal resolution involves increased design complexity, accompanied by greater fragility and more rigorous and complex calibration procedures.

To further complicate the picture, measurements made with FRAPs are more sensitive to temperature effects, sensor drift, and electrical noise, requiring careful experimental design and accurate data processing [35].

In the past, FRAPs consisted of multiple pressure sensors embedded in the probe head to directly reconstruct the instantaneous flow field: a conceptually intuitive configuration but at the same time disadvantageous in terms of the blocking effect. Recently, research has focused on mitigating these limitations by introducing approaches based on single or dual sensor probes operating in a mode known as virtual mode. In this study, the work of the Politecnico di Milano and ETH Zurich is particularly relevant.

In the virtual mode approach, measurements are not acquired simultaneously but sequentially at different orientations and subsequently reconstructed in post-processing. This allows for a reduction in the number of transducers housed in the head, resulting in a lower blockage. The reconstruction is based on the periodicity of the flow and on the phase-locked average with respect to a reference signal from the rotor. This approach allows the unstable component of the flow to be resolved, while stochastic turbulent fluctuations are partially filtered [33, 36].

Several miniaturised solutions operating in virtual mode have been developed at ETH Zurich. In particular, virtual four-sensor (V4S) and virtual five-sensor (V5S) probes have been tested, showing acceptable accuracy in terms of total and static pressure, flow angles and Mach number, while their main advantage lies in the drastic reduction in probe diameter [37, 38]. The same path has also been pursued at the Politecnico di Milano, where compact FRAPs have been developed and optimised specifically for applications in turbomachinery [33].

These progress have been fundamental for the miniaturisation of sensors, high-temperature operation and the reliability of dynamic calibration and data reconstruction. However, their adoption must be contextualised and justified based on the measurement objectives. If only time-averaged quantities are required, or if the flow does not present significant non-uniformities, pneumatic probes are often a more robust and affordable solution.

For this reason, the feasibility and the utility of applying fast-response aerodynamic probes to the experimental configuration discussed in this work was carefully evaluated through a dedicated study, reported in Appendix A. Here, the possible applications of these probes for our case are specifically addressed, evaluating their advantages and limitations.

5.2.3 Probe Selection Criteria

The selection criteria that led to the identification of the most suitable solution are presented below.

Probe size constraints

The first criterion adopted for probe selection concerns the size of the probe head. Careful selection of the right dimensions solves problems related to aerodynamic flow disturbance and spatial resolution, especially in presence of strong gradients.

It is therefore necessary to select a reference length for sizing, which depends on the nature of the flow field. In case of uniform flow, the relevant and commonly adopted length scale is the characteristic dimension of the duct, which in the cylindrical case corresponds to its diameter.

According to the ASME recommendations, illustrated in Figure 5.5, for a Mach number of approximately 0.6, representative of our case, the pressure losses due to blockage remain acceptable for probe-to-duct diameter ratio $d/D \lesssim 0.05$ [27]. For the present application, with a duct diameter of $D \approx 41\,\text{mm}$, a probe head diameter of less than 2 mm, typical of miniaturised probes, would be required.

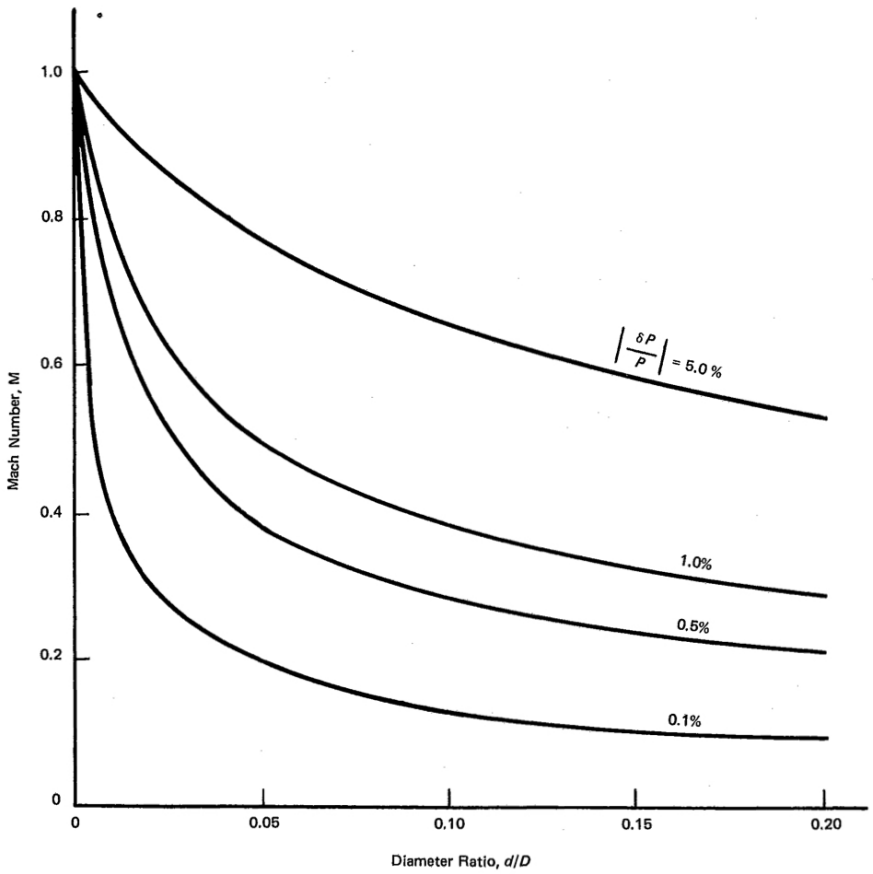

Figure 5.5: Magnitude of probe blockage effects as a function of Mach number and probe-to-duct diameter ratio d/D. For $M \approx 0.6$, acceptable losses are obtained for $d/D \lesssim 0.05$. Adapted from [27]

By contrast, in case of flows dominated by wakes, the characteristic length is the wake thickness. Several experimental studies, such as the one reported in [39], demonstrate a decrease in spatial gradient resolution when the probe head diameter becomes comparable to or greater than the wake width.

This occurs because different parts of the sensor or, in case of multi-hole probes, different pressure ports, simultaneously measure different regions of the wake, violating the assumption of locally uniform flow at the basis of probe calibration. The consequence is an underestimation of the wake depth and of the losses associated with it. To prevent this, it is necessary to keep the probe diameter below the wake thickness, as shown in the image on the right in Fig. 5.6.

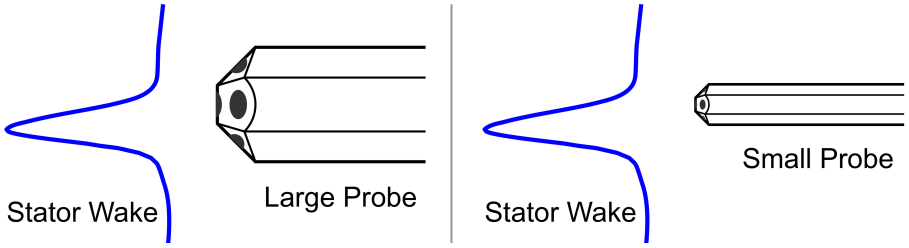

Figure 5.6: Effect of probe head diameter on wake resolution. When the probe diameter becomes comparable to the wake thickness, spatial averaging leads to a distortion of the measured wake profile. Adapted by [39]

In our measurement section, as revealed by the CFD analyses discussed in Chapter 5, the wakes and the resulting non-uniformity are already significantly attenuated, so the characteristic size chosen for the probe is the diameter of the duct.

As mentioned above, to obtain acceptable losses in our case, it is necessary to have miniaturised probes with head diameter smaller than 2 mm.

Flow non-uniformity and pressure fluctuation level

The second selection criterion relates to the level of circumferential flow non-uniformity detected on the measurement plane. As pointed out by the non-uniformity analysis in Chapter 5, the variation of total pressure in the pitch-wise direction across the section of interest is negligible as no significant wake structures are detected.

By comparing the amplitude of the total pressure oscillation relative to the average value with the sensitivity of the fast-response pressure transducers typically used in FRAPs, it was found that, in most cases, these deviations are below the minimum resolvable pressure level. Consequently, these fluctuations would not be detected even with the use of FRAP, whose complexity of construction and implementation is not justified by a corresponding gain in information compared to a time-averaged measurement.

To demonstrate this, a more detailed analysis was carried out to quantify the amplitude of total-pressure variations at the measurement section of the two operating points with the higher non-uniformity, namely OP8 and OP12.

The maximum peak-to-mean variation of total pressure was evaluated at each radial position and defined as

$$\Delta p_{t,\max}(r) = \left| p_{t,\max}(r) - \overline{p_t}(r) \right| .$$

Figure 5.7 shows the radial distribution of $\Delta p_{t,\max}$ at the measurement section. In the same figure, the sensitivity threshold of a high-accuracy pressure transducer is also reported. The selected reference sensor features a full-scale range of 0.35 bar and an accuracy of $\pm 0.1\%$ of full scale, corresponding to a minimum detectable pressure variation of approximately 35 Pa.

The comparison indicates that total pressure fluctuations exceed the sensor sensitivity only for radial positions above 65% of the radius. Therefore, even in this more critical condition, the use of a fast-response pressure probe at the considered measurement section is not justified.

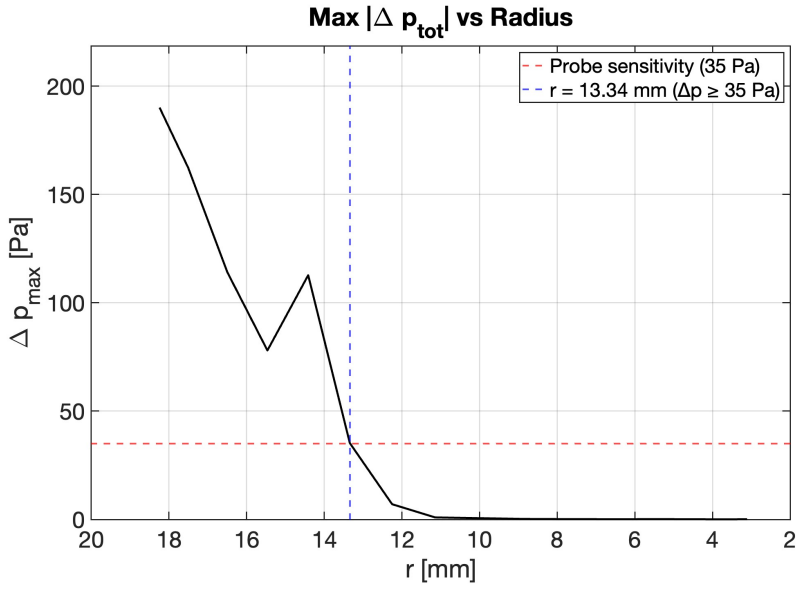

Figure 5.7: Radial distribution of the maximum total-pressure deviation from the mean at the candidate measurement section for OP8. The dashed line indicates the sensitivity threshold of a high-accuracy pressure sensor (35 Pa).

The same approach was adopted for OP12, finding that all maximum total-pressure fluctuations remain below the sensitivity threshold of the reference high-accuracy pressure transducer.

These findings suggest that pneumatic probes are preferred as they are more suitable to measure average total pressure for nearly uniform flow. These constitute a simpler, more robust and reliable solution for the present study, consistent with the observed flow characteristics.

Flow angle magnitude and spatial gradient

The third selection criterion concerns the flow angle and its spatial gradient along the measurement plane. As reported in the flow angle analysis presented in Chapter 5, there is a significant variation in the direction of the flow, and consequently in its angle along the radial coordinate, particularly with regard to the yaw angle.

Since a probe traversing strategy will be adopted in the future experimental campaign, during a radial scan along the diameter of the section the probe would encounter significantly different flow angles. Under such conditions, probes that are highly sensitive to flow misalignment would require continuous and precise reorientation at each measurement point, adding complications and uncertainties.

To avoid this, a probe geometry with low sensitivity to the flow angle is required and this feature is possessed by the aforementioned Kiel probes. Thanks to the shroud surrounding the inner tube, these probes allow accurate measurements of total pressure even when the probe axis is not perfectly aligned with the local flow direction.

This feature is particularly advantageous in the present case, since this probe is able to provide reliable measurements without needing to be continuously reoriented, ensuring greater robustness, repeatability and efficiency.

5.2.4 Selected Probe

Single-hole Pitot pneumatic probes and multi-hole probes are excluded due to their sensitivity to alignment and larger dimensions in the case of multiple ports, while FRAP probes are not necessary as total pressure oscillation would not be detected. A Kiel type probe was then selected as a result of the above analysis.

Among the commercially available solutions, the optimal choice was the miniaturised Kiel probe manufactured by *Aero Sensor Ltd.* (UK) [40]. This probe features a compact geometry, a wide range of angular insensitivity and resistance to high temperatures.

The selected probe has a head diameter of 1.65 mm, leading to a probe-to-duct diameter ratio $\frac{d}{D} = 0.04$. The angle insensitivity range is approximately $\pm 45°$, meaning that the probe does not need to be reoriented for each measurement during the traversing. The probe head is oriented at 90° with respect to the stem axis, a preferred configuration over the one parallel to the stem, as it simplifies mechanical integration into the traversing system. The probe can operate up to Mach 1 and is available in materials suitable for temperatures up to 980 °C.

To increase structural rigidity and allow for integration with the probe's traversing and sealing system, a custom stem configuration was requested. In this new design the thin section of the original stem is connected to a 4 mm diameter intermediate shaft, which in turn merges into an 8 mm diameter shaft. This stepped geometry ensures that only the smaller diameter portion enters the flow, so this portion was designed long enough to perform the entire traversing from wall to center. The larger diameter is necessary not only for greater robustness but also for compatibility with

the sealing elements, which have an internal diameter of 8 mm.

It is specified that the probe is supplied without an integrated pressure transducer, which will be selected separately and screwed onto the shaft end outside the flow. In the technical drawings provided by the manufacturer and shown in Fig. 5.8 it is possible to see in detail the probe stem geometry and the male threaded connection (BSPP G $\frac{1}{4}$).

Probe blockage assessment

Even though the probe head diameter is well below the critical diameter ratio, an evaluation of the Kiel blocking effect was performed to ensure that it does not cause transonic flow. The analysis was conducted assuming the worst case scenario, i.e., when the probe stem is completely immersed in the flow and creates maximum blockage. This condition occurs when the probe tip reaches the center of the channel. The calculation was made considering an average Mach number of $M_1 = 0.6$ in the measurement section, while the specific heat ratio of the working fluid at the same condition is $\gamma = 1.025$.

The probe frontal area (A_K) and the available flow area before (A_1) and after (A_2) insertion are:

$$A_K = l_s \cdot d_t = 20 \cdot 1.65 \text{ mm}^2 = 33 \text{ mm}^2, \tag{5.1}$$

$$A_1 = \pi R^2 = \pi \cdot (20 \text{ mm})^2 = 1256 \text{ mm}^2 \tag{5.2}$$

$$A_2 = A_{\text{tot}} - A_K = 1256 - 33 = 1223 \text{ mm}^2 \tag{5.3}$$

where l_s is the probe shaft length exposed to the flow, d_t is the probe tip diameter and R is the duct radius.

Therefore, the area reduction ratio is:

$$\frac{A_2}{A_1} = \frac{1223}{1256} = 0.9737. \tag{5.4}$$

Given the assumption of quasi-one-dimensional isentropic flow, the area–Mach relation is:

$$\frac{A}{A^*} = \frac{1}{M}\left[\frac{2}{\gamma+1}\left(1 + \frac{\gamma-1}{2}M^2\right)\right]^{\frac{\gamma+1}{2(\gamma-1)}}. \tag{5.5}$$

Using $M_1 = 0.6$ and $\gamma = 1.025$ yields:

$$\frac{A_1}{A^*} = \frac{1}{M_1}\left[\frac{2}{\gamma+1}\left(1 + \frac{\gamma-1}{2}M_1^2\right)\right]^{\frac{\gamma+1}{2(\gamma-1)}} \simeq 1.162. \tag{5.6}$$

The reduced area ratio is then:

$$\frac{A_2}{A^*} = \frac{A_2}{A_1}\frac{A_1}{A^*} = 0.9737 \cdot 1.162 = 1.1316. \tag{5.7}$$

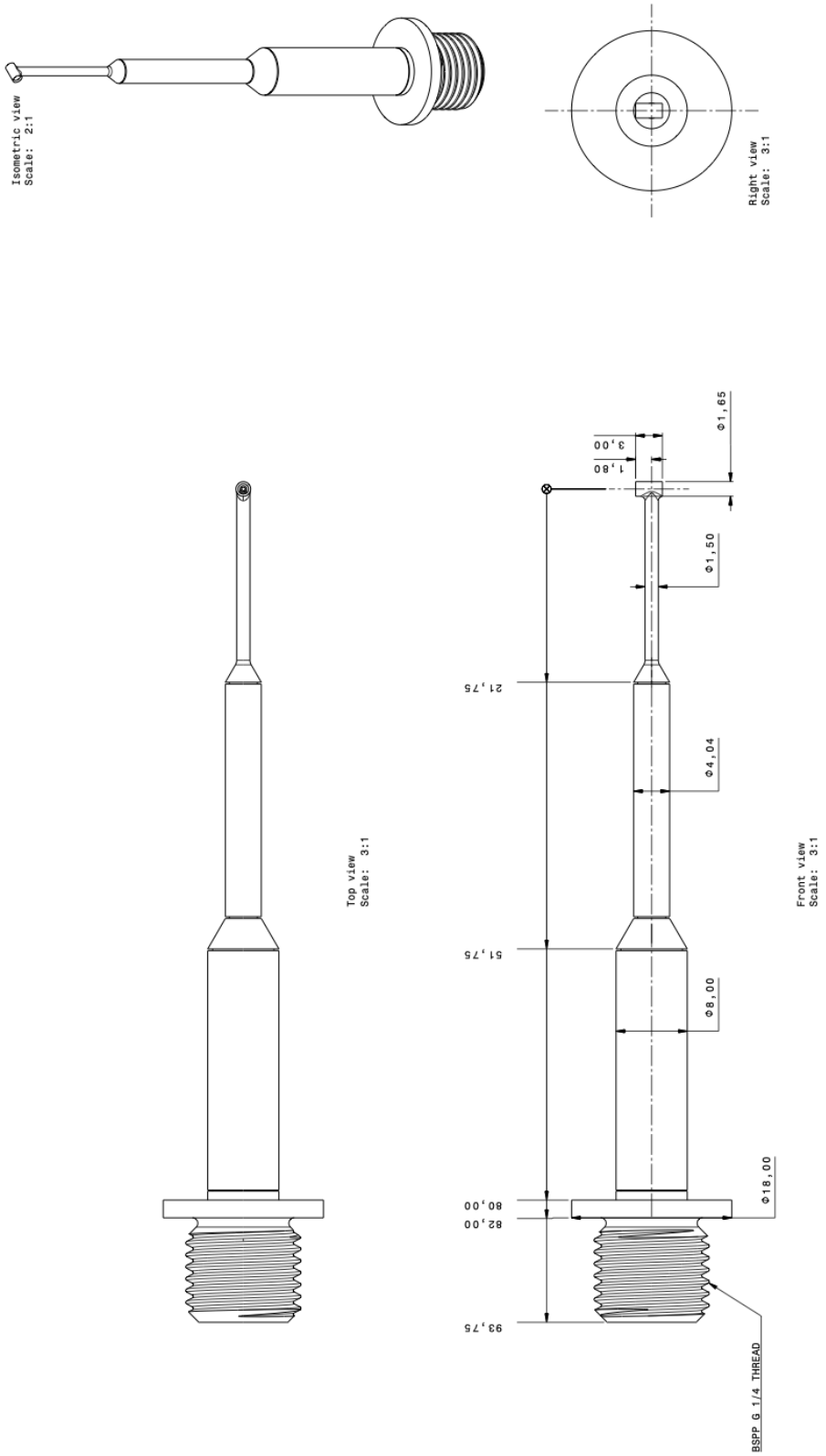

Figure 5.8: Technical drawing of the selected miniaturized Kiel probe [40], showing the probe head geometry and stem dimensions.

The corresponding Mach number M_2 is obtained by iteratively solving Eq. (5.5) for M such that $A/A^* = 1.1316$:

$$1.1316 = \frac{1}{M_2}\left[\frac{2}{\gamma+1}\left(1+\frac{\gamma-1}{2}M_2^2\right)\right]^{\frac{\gamma+1}{2(\gamma-1)}} \quad \Rightarrow \quad M_2 \approx 0.67. \tag{5.8}$$

The resulting increase in Mach number is therefore limited ($M_1 = 0.60 \rightarrow M_2 \approx 0.67$) and remains well below unity. This means that even under worst-case blockage, the probe does not induce transonic flow in the measurement section.

Aerodynamic load, bending stress, and tip deflection

A conservative assessment of the aerodynamic force exerted by the flow on the probe was performed. The objective is to ensure that the stress and deflection remain below allowable limits, hence preventing the structural failure of the probe. The analysis considers the worst-case operating condition, taking the maximum flow velocity measured in the cross-section and the probe fully inserted into the flow, in an identical configuration as the one described in the previous paragraph.

The maximum velocity and mean density used for the worst-case estimate are:

$$V_{\max} = 88.65 \text{ m/s}, \qquad \rho = 1.7282 \text{ kg/m}^3. \tag{5.9}$$

The corresponding dynamic pressure is:

$$q = \frac{1}{2}\rho V_{\max}^2 = \frac{1}{2} \cdot 1.7282 \cdot (88.65)^2 = 6790.7 \text{ Pa}. \tag{5.10}$$

The aerodynamic force is estimated as a drag-type load:

$$D = C_D \, q \, A_K, \tag{5.11}$$

where C_D is the drag coefficient and A_K is the frontal projected area of the probe in the fully inserted configuration. Here, $C_D = 1.2$ is adopted for conservativeness, and the corrected frontal area is taken consistently with the blockage assessment discussed earlier.

Therefore,

$$D = 1.2 \cdot 6790.7 \cdot 33 \times 10^{-6} = 0.269 \text{ N}. \tag{5.12}$$

The resulting bending moment at the critical section is calculated as:

$$M_{\max} = D \, \ell_M, \tag{5.13}$$

where ℓ_M is the effective lever arm considering that the aerodynamic force is applied at the center of the projected area.

The resulting bending moment is:

$$M_{\max} = 0.00274 \text{ N m}. \tag{5.14}$$

The probe stem is modeled as a hollow circular beam with outer and inner diameters:

$$d_o = 1.5 \text{ mm}, \qquad d_i = 1.1 \text{ mm}. \tag{5.15}$$

The moment of inertia, with respect to an axis lying in a plane perpendicular to the cylinder axis, can be calculated as:

$$I = \frac{\pi}{64}\left(d_o^4 - d_i^4\right) = \frac{\pi}{64}\left(1.5^4 - 1.1^4\right) \times 10^{-12} = 1.77 \times 10^{-13} \text{ m}^4. \tag{5.16}$$

The maximum bending stress is then:

$$\sigma_{\max} = \frac{M_{\max}\,(d_o/2)}{I} = \frac{0.00274 \cdot (1.5 \times 10^{-3}/2)}{1.77 \times 10^{-13}} = 11.6 \text{ MPa}. \tag{5.17}$$

Since the probe stem material is known and is AISI 316L stainless steel, is it possible to calculate the maximum allowable stress as:

$$\sigma_{\text{allow}} = \frac{\sigma_y}{SF} = \frac{170 \text{ MPa}}{2} = 85 \text{ MPa}, \tag{5.18}$$

where σ_y is the yield strength and SF is the safety factor applied. Since $\sigma_{\max} \ll \sigma_{\text{allow}}$, the stress level lies within acceptable limits.

Using the cantilever-beam approximation, the tip deflection is then extimated as:

$$\delta = \frac{D\,\ell_\delta^3}{3EI}, \tag{5.19}$$

where E is the Young's modulus and ℓ_δ is the the length of the cantilever shaft. With $E = 193$ GPa (proper of the specific material) the deflection results to be:

$$\delta \approx 0.0225 \text{ mm}. \tag{5.20}$$

Overall, even under worst-case conditions, the aerodynamic load produces a maximum bending stress far below the allowable limit and a negligible tip deflection. Thanks to these results is it possible to state that the selected probe configuration is structurally adequate for the planned experimental campaign.

Probe Orientation

The insensitivity range for yaw and pitch angles of the selected Kiel probe is $\pm 45°$. Therefore a proper probe orientation is required to keep the flow angle seen by the head within these limits.

On the design operating point as reported in Section 4.2, the pitch angle remains between $\pm 10°$, so orienting the probe head parallel to the z-axis does not introduce significant misalignment issues. Concerning the yaw angle, although it remains within the $\pm 45°$ insensitivity limits, a more favorable orientation of $9°$ in the y–z plane reduce the effective flow angle experienced by the probe, as shown in Figure 5.9

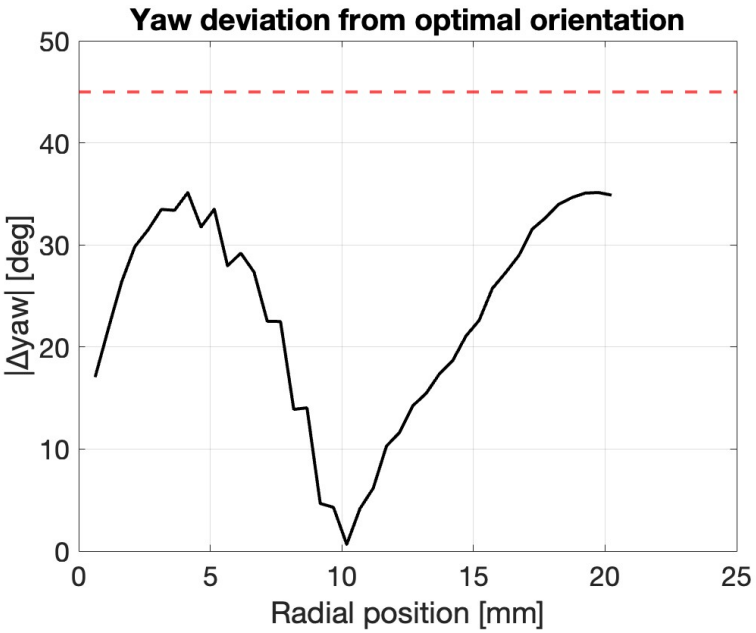

Figure 5.9: Absolute yaw angle seen by the probe after reorienting the probe head by approximately 9°. The flow angles remain well below the insensitivity limits of the Kiel probe over the entire radial range.

The same analysis was carried on operating points 4, 8 and 12, whose flow angle distribution is described in Section 4.3.2. For OP4 the optimal yaw orientation is approximately −40°, for OP8 around −15°, while for OP12 is 30°.

An additional analysis was performed to assess whether a fixed probe orientation corresponding to the on-design condition (9°) could still be adopted for off-design measurements.

Figure 5.10 reports the resulting effective yaw angle relative to the probe for the three off-design operating points.

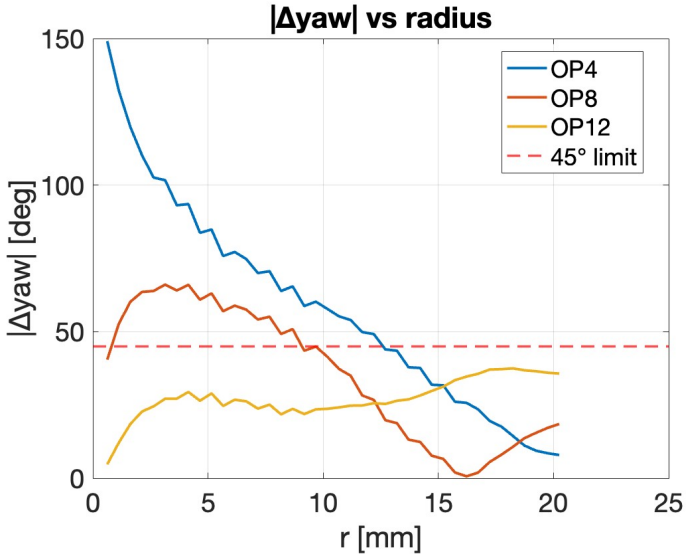

Figure 5.10: Effective yaw angle seen by the probe assuming a fixed orientation of 9° for OP4, OP8, and OP12.

The results show that only for OP12 the effective yaw angle remains entirely within the ±45° insensitivity limits. Therefore, for OP12, the same probe orientation adopted at the design condition can be retained, while for OP4 and OP8 a dedicated reorientation would be required to minimize flow-angle effects.

5.3 Pressure Transducer

A pressure transducer compatible with functional, environmental, and safety requirements was selected.

An initial selection is made by narrowing the field to pressure transducers certified for operation in hazardous environments, in compliance with the ATEX directive applied to the facility [16]. Among these, the focus is on those that provide an absolute, non-differential total pressure measurement, with a full-scale appropriate to the pressure range expected. Based on the CFD predictions in the measurement section, total pressures are expected to be in a range of 0.4-0.6 bar.

Another constraint that drives the choice is the temperature rating, since the fluid inside the channel is approximately at 249°C at the test section and it is currently not known how much cooling does the fluid undergo within the probe stem.

Additional requirements include good accuracy, a compact package, and a compatible threaded connection with that of the probe stem.

All of the above requirements were met by the *Model IS-3* pressure transmitter manufactured by *WIKA Alexander Wiegand SE & Co. KG* [41].

This model is intrinsically safe, which means that it is certified for use in hazardous areas. The transducer was configured with an optional cooling duct that allows it to be used in applications where the temperature can be up to 200°C.

The absolute pressure measurement range can be narrowed between 0 and 1 bar, a choice that allows a reduction of measurement error which is proportional to the full scale (i.e., 0.25% FS).

An image of the selected pressure transmitter and the corresponding dimensional drawing provided by the manufacturer are shown in Fig. 5.11.

5.4 Traversing System

The total pressure profile in the measurement section is non-uniform, so a single-point measurement would not be representative of the phenomenon.

To better describe the flow conditions, spatially resolved measurements analyzing multiple points within the section are required. This objective is achieved using a dedicated traversing system, which allows for controlled and repeatable positioning of the radial direction.

The objective is to acquire the radial total pressure profile by reconstructing discrete measurements taken at multiple points, with the aim of validating numerical predictions and predicting turbine performance.

(a) Intrinsically safe pressure transmitter [41].

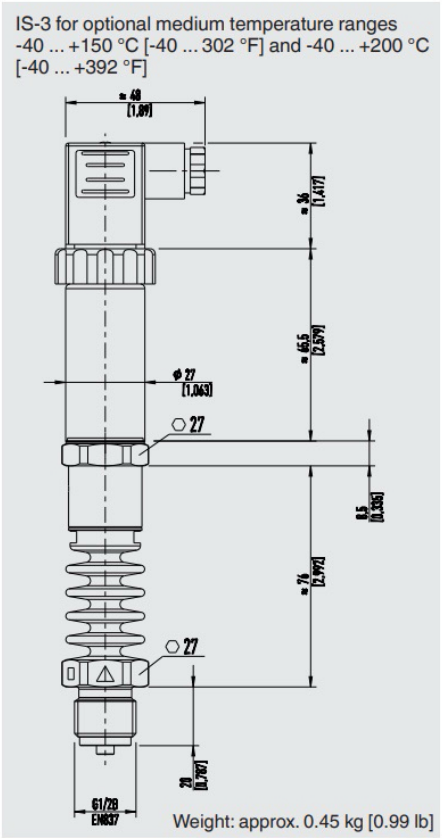

(b) Overall dimensions of the pressure transducer [41].

Figure 5.11: Selected pressure transducer for total pressure measurements [41].

The design and implementation of this system must ensure adequate positioning accuracy and mechanical robustness, always complying with the facility constraints.

The following sections describe the traversing system strategy and architecture, including all the components that make it operational.

5.4.1 Traversing Requirements

The design of the traversing system is guided by safety requirements derived from operational standards, and functional requirements related to flow characteristics.

For as regards safety requirements, it is necessary to comply with the ATEX regulation so all electrical and electromechanical components must be certified for use in Zone 2 with temperature class T2 [17]. This regulation applies not only to the actuator, but also to its accessory parts such as cables, motor and connectors.

From the functional requirements perspective, the traversing system must allow for the probe to move radially from the wall to the center of the duct, covering a total distance of approximately 20 mm. This distance must be covered with discrete positioning steps of $1 - 2\,\text{mm}$ to adequately reconstruct the total pressure profile. The impact of radial step size on pressure profile reconstruction is illustrated in Fig. 5.12, where the total pressure profiles obtained using radial spacings of 1 mm and 2 mm are compared. Although both resolutions capture the overall trend, the finer 1 mm step is preferable as it allows for a more accurate representation of the curve. Wider steps will result in too coarse reconstruction so 2 mm it's kept as a top limit.

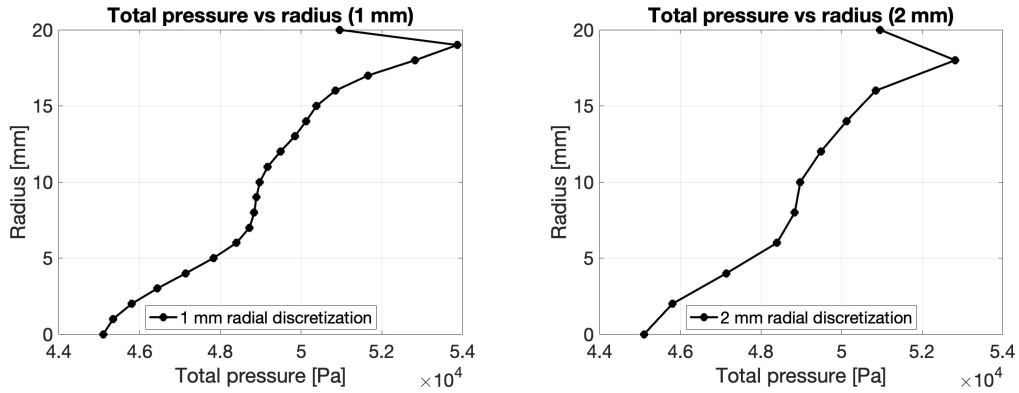

(a) Radial reconstruction using 1 mm step size.

(b) Radial reconstruction using 2 mm step size.

Figure 5.12: Effect of radial traversing step size on the reconstruction total pressure profiles at the test section.

In order to assure a reliable reproduction of the selected step size over the full stroke, positioning accuracy and repeatability are also fundamental requirements, in addition with stable motion and low vibrations.

5.4.2 Selected Design Solution

The traversing system selected in the design phase is based on pneumatic actuation. This choice was primarily driven by the safety constraints imposed by the environment, since the availability of compact and fully ATEX-compliant electric actuators and auxiliary components is limited. In contrast, a wide range of pneumatic ATEX-certified components is commercially available, including actuators, valves, and control elements, which simplifies both the design and certification process. While ATEX-certified electric motors and actuators are only available in large sizes, pneumatic ones generally feature reduced overall dimensions. Another advantage of the selected design is that it is composed exclusively of certified components supplied by the same manufacturer (*Festo BV.* [42]). This improves compatibility between elements, simplifies assembly, and enhances overall system reliability. Moreover, the pneumatic solution is readily adoptable in the facility, as a compressed air supply line is available.

The selected solution consists of a linear actuator, a proportional directional control valve, a controller and auxiliary equipment such as an air-filter, pneumatic hoses, electrical connections, fittings and mounting supports. In the following sections all these components are presented in detail while the alternative design solution is discussed in Appendix C.

Pneumatic linear actuator

The actuator for the selected traversing solution is a pneumatic linear actuator ATEX certified with protection level II 3G/3D and temperature class T4, which safely exceeds the minimum temperature-class requirement (T2).

The actuator works with compressed air delivered by a proportional control valve through two pneumatic hoses.

The main functional elements of the actuator, indicated in Fig. 5.13, are described below:

- **Mechanical hard stops (1):** integrated end-of-stroke stops that provide a physical limit to the actuator motion, in order to prevent overtravel.
- **Pneumatic ports (2, 8):** two pneumatic connections used to delivery compressed air coming from the valve to the actuator and enable bidirectional linear motion.
- **Measuring system port (3):** electrical interface used to connect the actuator displacement encoder to the valve electronics in order to provide real-time position feedback.
- **Displacement encoder (6):** integrated position sensor that continuously measures the actuator stroke in order to guarantee closed-loop position control and accurate and repeatable probe positioning .

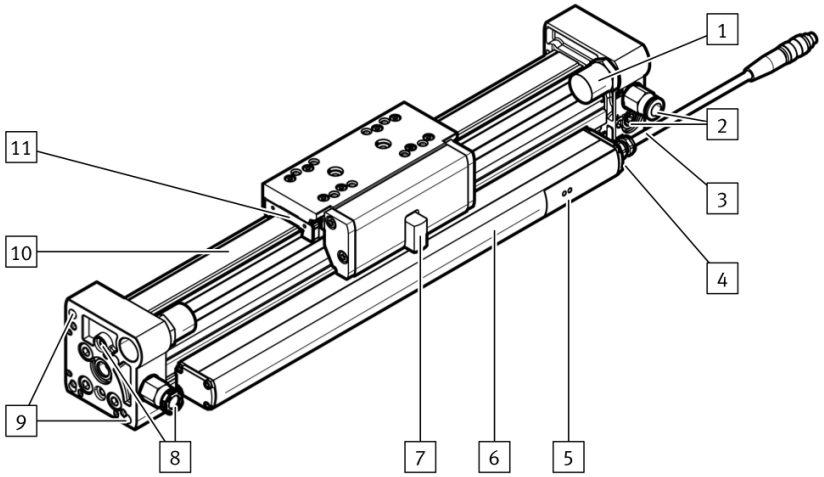

Fig. 1: Product design

1	Stop bolt	7	Measuring magnet
2	Pneumatic port 2, Motion to right	8	Pneumatic port 1, Motion to left
3	Measuring system port	9	Mounting thread for drive
4	Earthing strap for displacement encoder	10	Guide rail
5	LED display	11	Lubrication nipple for rolling bearings
6	Displacement encoder		

Figure 5.13: Pneumatic linear actuator DGCI with integrated displacement encoder and recirculating ball bearing guide (numbers refer to the main functional components) [42].

- **Measuring magnet (7):** permanent magnet mechanically coupled to the moving carriage; its position is detected in a contactless mode by the displacement encoder, without needing for electrical connections.
- **Guide rail (10):** recirculating ball bearing guide that supports the moving carriage upon which the probe is mounted. This solution allows for a more smooth and stable motion during traversing.

Table 5.1 summarizes the specifications of the selected actuator and the corresponding part-number coding.

Table 5.1: Main specifications and coding of the selected pneumatic actuator DGCI-18-100-KF-QD-EX2 [42].

Item	**Value**	**Description / Notes**
Model / Part number	DGCI-18-100-KF-QD-EX2	Linear actuator with integrated displacement encoder
Actuation type	Pneumatic	Compressed-air driven
Nominal stroke	100 mm	Adaptable to our 20 mm stroke
Piston diameter	18 mm	Determines actuation force
Guide type	KF	Recirculating ball bearing guide
Pneumatic fittings	QD	Push-in fittings on front side
Integrated sensor	Yes	Displacement encoder for closed-loop positioning
Position resolution	0.01 mm	Encoder resolution
Repeatability	± 0.2 mm	Manufacturer specification
Minimum reliable step	5 mm	Used as baseline for robust positioning; refined in the traversing strategy
ATEX certification	II 3G / II 3D	Suitable for Zone 2 environments
ATEX marking (gas)	Ex nA IIC T4 X (Gc)	Max surface temperature class T4 ($< 135°C$)
ATEX marking (dust)	Ex tc IIIC T120°C X (Dc)	Dust protection; enclosure rated IP65
Ingress protection	IP65	Protection against dust and water jets

Although the minimum reliable positioning step of the actuator is 5 mm, this limitation is overcome through the adopted traversing strategy, as discussed in the following section (Section 5.4.3).

Proportional directional control valve

The valve chosen to drive the actuator is ATEX certified for a category II 3G with temperature class T5, compatible with the requirements of the present application.

The VPWP valve regulates the pneumatic supply to the actuator by modulating the direction and intensity of the air flow as a function of the control signal and allowing closed-loop position control of the actuator.

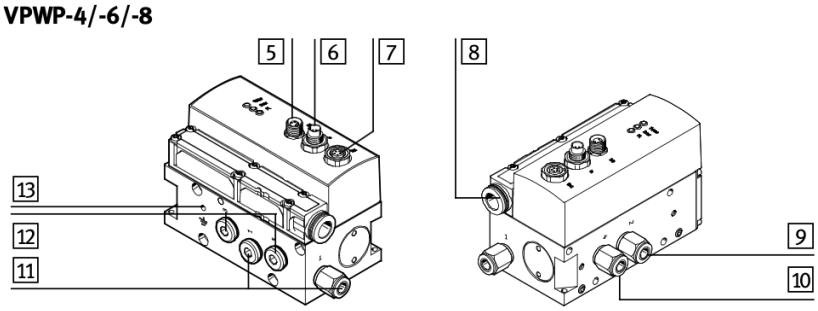

Figure 5.14: Proportional directional control valve VPWP (numbers refer to the main functional components) [42].

The main functional components of the proportional valve, indicated in Fig. 5.14, are summarized below:

- **Digital / voltage output (DO) (5):** electrical output providing status and diagnostic information. It can be implemented as a digital or voltage signal.
- **Controller module connection (IN) (6):** electrical interface between the valve and the external controller. It sends input command signals for proportional actuation.
- **Sensor interface connection (OUT) (7):** electrical interface used to transmit feedback signals in output from the valve to the control system, enabling closed-loop operation.
- **Pneumatic exhaust connections (3/5) (8, 12):** exhaust ports for the 5/3-way valve configuration. These ports can be open to ambient or sealed.
- **Pneumatic connection 2 and 4 (9-10):** actuator ports that supply compressed air to the pneumatic actuator, enabling motion in both directions.
- **Pneumatic supply connection (11):** main compressed air supply port which feeds the proportional valve.
- **Earth terminal (FE) (13):** earthing connection to ensure grounding of the valve.

The main technical features of the selected proportional valve and the interpretation of the part-number coding, are summarized in Table 5.2.

Table 5.2: Main specifications and coding of the selected proportional directional control valve VPWP-4-L-5-Q6-10-E-F-EX1 [42].

Item	Value	Description / Notes
Model / Part number	VPWP-4-L-5-Q6-10-E-F-EX1	Proportional directional control valve
Valve type	VPWP	Proportional directional control valve
Size	4	Nominal size
Installation	In-line (L)	Direct in-line mounting
Valve function	5/3-way	Bidirectional control with center position
Pneumatic fittings	Q6	Push-in fittings QS-1/8-6
Pressure range	0–10 bar	Suitable for actuator supply
Electrical interface	E	LED indication only
Exhaust treatment	F	Flat plate silencer
ATEX certification	II 3G	Suitable for Zone 2 environments
ATEX marking	Ex ec IIC T5 Gc X	Max surface temperature $<$ 100°C

Controller and electrical terminal

The control of the proportional valve and of the pneumatic actuator is handled by a modular electrical terminal of the CPX family, equipped with an integrated position controller (CMAX).

Figure 5.15: Exemplary configuration of the CPX modular electrical terminal with integrated position controller [42].

Like the previously presented components, the CPX terminal is also available in an ATEX-certified version, with protection level II 3G and temperature class T4, making it suitable for operation in Zone 2. However, the controller is expected to be installed outside the ATEX-classified area, so the non certified version may be sufficient.

This CPX terminal constitutes the control unit of the traversing system, as it receives position commands from the workstation and consequently actuates the valve acquiring position feedback from the encoder. This allows the closed loop control of the probe's position. In order to perform this control, the CPX controller has to interface with:

- the **power supply** that provides the required operating voltage to the terminal;
- the **proportional directional control valve**, electrically driven by the CPX;
- the **pneumatic actuator**, indirectly controlled through the valve and encoder feedback;
- the **laboratory control system** which sends motion commands for probe traversing and positioning.

In Table 5.3 the main technical features of the selected CPX controller configuration and an explanation of the part-number coding are summarized.

Table 5.3: Main specifications and coding of the selected controller configuration [42].

Item	**Value**	**Description / Notes**
Terminal family	CPX	Modular electrical terminal
Integrated controller	CMAX T21	Position controller for pneumatic drives
Part number	50E-F36GCQST21-Z-EX1E+HNGZ	Complete configured assembly
Fieldbus node	F36	Ethernet/IP communication interface
Bus connection	Ethernet	Real-time communication with control system
Electrical supply	M18, 4-pin	Power supply connector
Operating voltage	24 V DC	Nominal DC voltage
Ingress protection	IP65 / IP67	Depending on module configuration
Internal cycle time	< 1 ms	Suitable for closed-loop motion control
Diagnostics	Integrated	Module- and channel-level diagnostics
ATEX certification	II 3G	Suitable for Zone 2 environments
ATEX marking	Ex nA IIC T4 X Gc	Max surface temperature $< 135°C$
Mounting	Hat rail (H)	DIN rail mounting

Regarding the integration of the CPX terminal into the laboratory control architecture, the connection method with the current control system of the experimental facility, consisting of a *CompactRIO* Ethernet chassis manufactured by *National Instruments* [43], is still being evaluated.

The most suitable integration option is to connect the CPX terminal to the CompactRIO through an Ethernet switch to allow the programming of the traversing directly from the laboratory workstation. With this solution it is possible to maintain the same control environment both for probe movement and pressure data acquisition, eliminating the risk of conflicts between them.

An alternative option would be to bypass the CompactRIO and control the CPX terminal through an external controller. The downside of this approach is that the traversing would be programmed in a separate environment, potentially introducing conflicts or poor synchronization between probe positioning and pressure acquisition. For this reason, Ethernet integration with the CompactRIO is currently considered the most reliable solution.

Auxiliary Equipment

In order to ensure the correct operation of the pneumatic actuation system, several auxiliary elements are required. All of them are listed below.

- **Pneumatic hoses for valve–actuator connection (PUN-H-6X1-BL)**: two pneumatic hoses with outer diameter 6 mm used to connect the valve to the actuator pneumatic ports.
- **Pneumatic hoses for air supply line (PUN-H-8X1,25-BL)**: one pneumatic hoses with outer diameter 8 mm used to connect the laboratory compressed air supply to the inlet of the proportional valve.
- **Filter and pressure regulator unit (MSB4-1/8:C4:J5:H3-WP)**: air-filter and pressure regulator installed between the compressor and the proportional valve in order to ensure that the supplied air meets the cleanliness and pressure required.
- **Electrical connection cable (KVI-CP-3-GS-GD-2)**: ATEX certified electrical connection cable which links the proportional valve to the CPX controller providing both power and signal transmission.
- **Pneumatic fittings (QS-G1/8-8)**: push-in fittings with G1/8 thread used to connect the pneumatic hoses to the valve, filter–regulator unit, and actuator ports.
- **Mounting kit for valve/controller assembly (CPASC1-BG-NRH)**: Standardized mounting interfaces used to fix the proportional valve and/or the controller to the supporting structure.

- **Mounting kit for pneumatic actuator (HPC-18)**: Foot mounting kit designed for the DGCI-18 actuator, used to attach the actuator to the traversing system support.

Overview of Pneumatic and Electrical Connections

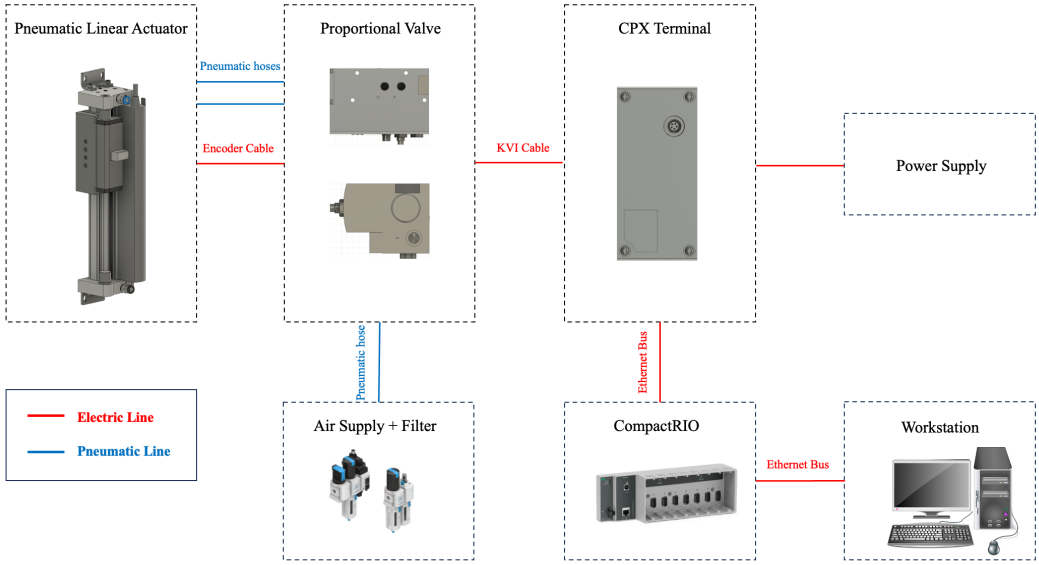

Figure 5.16: Overview of the pneumatic and electrical connections of the traversing system. Configuration with CompactRIO-based control architecture.

Figure 5.16 gives an overview of the pneumatic and electrical connections of the traversing system in the preferred configuration with the CompactRIO, as discussed before.

Considering the pneumatic line, the air exiting the compressor is filtered by the filter-regulator unit and then conveyed to the valve via the pneumatic hose. The air is then sent from the valve to the pneumatic actuator via flexible pneumatic hoses, enabling controlled bidirectional movement of the probe.

Following the electrical line, the external power supply powers the CPX terminal, which communicates via Ethernet bus with the CompactRIO system. The proportional valve receives position feedback from the actuator encoder through a dedicated integrated cable, while it receives commands from the controller via KVI cable.

Integration in the setup

To further assess the feasibility of the selected pneumatic traversing solution, a CAD integration of the assembly into the turbine test rig was made. The aim of this analysis is the visual evaluation of the overall footprint of the system and its compatibility with the existing setup.

Figure 5.17 shows two representative CAD views of the integrated configuration. The pneumatic linear actuator is mounted vertically above the test section, and, in

order to allow the probe to be inserted radially into the flow, the flange hosting the process-connection ports must be reinstalled with a rotation of 22.5°.

Overall, the CAD integration confirms that the selected solution can be accommodated within the available space without interfering with the already built structures.

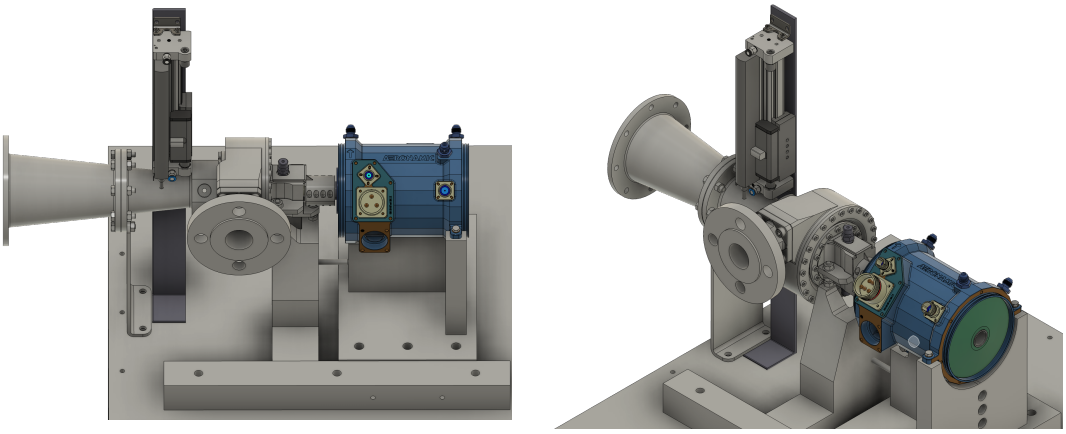

Front view

Perspective view

Figure 5.17: CAD integration of the pneumatic traversing system with the turbine test rig, showing the overall footprint.

5.4.3 Traversing Strategy

As mentioned in Section 5.4.1, the maximum step size for measurement acquisition to obtain a faithful reconstruction of the pressure profile is 2 mm. However, this is not compatible with the minimum step size for reliable positioning of the selected pneumatic actuator, which is 5 mm, as shown in Table 5.1 . This limitation can be circumvented by adopting a multiple-traverse strategy. The probe traverses the distance from the wall to the center of the duct five times, using a 5 mm step size, but with an initial offset of 1 mm between consecutive passes. This strategy, by interleaving the five sequences, achieves finer spatial sampling, with an effective step size of 1 mm. For safety reasons and to avoid potential mechanical interference during the traversing, the measurement point closest to the wall is set at 2 mm from it.

Figure 5.18 schematically illustrates this traversing strategy, where the points scanned by different traversal are indicated by different colors. In particular, filled circular markers indicate measurement points acquired during the outward traverse from wall to center, while open triangular markers denote points acquired during the return motion towards the wall. As an illustrative example, during the second traversing pass the probe moves outward through the positions at 6, 11, and 16 mm, and subsequently acquires an additional measurement at 3 mm while returning to the wall at the homing position. In this way it is also possible to scan the near-wall region without requiring steps smaller than the minimum reliable increment. For the return movement from the last point to the homing position, the step size constraint

of 5 mm does not necessarily need to be respected, since the positioning accuracy during the return to zero is not as important as it is for the measurement points. This strategy allows for repeatable and accurate positioning while achieving the required spatial resolution.

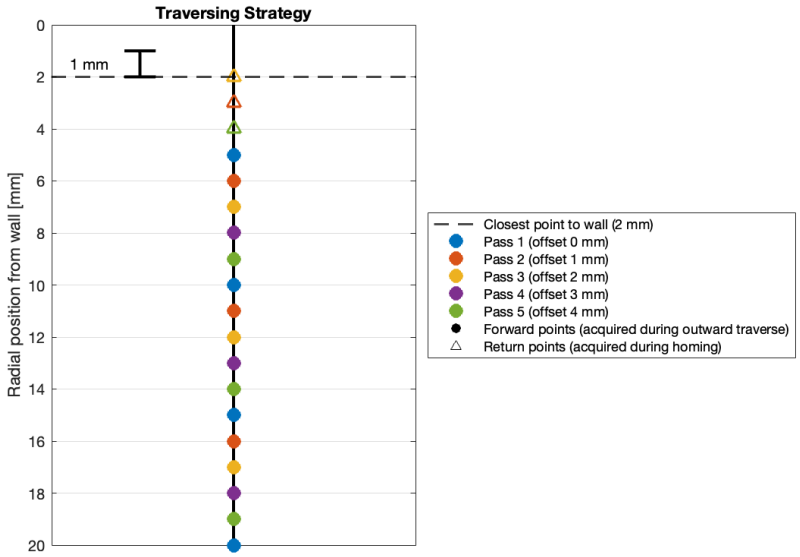

Figure 5.18: Schematic representation of the multi-pass traversing strategy. Five traverses with a 5 mm step and 1 mm relative offset are interleaved to achieve an effective spatial resolution of 1 mm along the radial direction.

Dwell Time Estimation and Dynamic Response of the Pneumatic Measurement Chain

A key consideration when defining the traversing strategy is the length of time the probe must remain at each point to correctly acquire the measurement, also known as dwell time. In case of pneumatic probes, the pressure measured by the transducer converges to the pressure actually recorded at the probe inlet with a certain delay. This delay is due to the dynamic response of the pneumatic system, which has an intrinsic latency dependent on the fluid characteristics and on the volume of the probe and transducer.

To calculate the dwell time, the pneumatic measurement chain is modeled as a first-order linear dynamic system. The response of these systems is such that when a step change in pressure at the probe inlet occurs, the pressure measured by the transducer asymptotically approaches its value according to an exponential law of the type

$$p_L(t) = p_0 \left(1 - e^{-t/\tau}\right), \tag{5.21}$$

where p_0 is the pressure at the probe inlet, p_L is the pressure measured by the transducer, and τ is the characteristic time constant of the pneumatic system.

In the Laplace domain, the corresponding transfer function reads

$$\frac{p_L(s)}{p_0(s)} = \frac{1}{1+s\tau}. \tag{5.22}$$

After approximately 3τ–5τ the response reaches 95–99% of the final value, which provides a direct criterion for the minimum dwell time at each traversing position.

The relationship between the pressure and volumetric flow rate at the inlet (0) and at the outlet (L) of a pneumatic tube of length L can be expressed through the transmission-line matrix (ABCD) [44].

In the frequency domain, this relation is

$$\begin{bmatrix} p_0 \\ U_0 \end{bmatrix} = \begin{bmatrix} \cosh(\varphi L) & Z_c \sinh(\varphi L) \\ \dfrac{1}{Z_c}\sinh(\varphi L) & \cosh(\varphi L) \end{bmatrix} \begin{bmatrix} p_L \\ U_L \end{bmatrix}, \tag{5.23}$$

where p is the pressure, U the volumetric flow rate, $Z_c = p/U$ the characteristic impedance of the tube, φ the complex propagation constant, and L the tube length.

In the present application, it is possible to assume low frequency domain associated with probe motion and pressure settling and a short pneumatic tube. With these assumption we have

$$\varphi L \ll 1 \tag{5.24}$$

so the transmission matrix become

$$\begin{bmatrix} p_0 \\ U_0 \end{bmatrix} = \begin{bmatrix} 1 & Z_c(\varphi L) \\ \dfrac{1}{Z_c}(\varphi L) & 1 \end{bmatrix} \begin{bmatrix} p_L \\ U_L \end{bmatrix}, \tag{5.25}$$

The first equation of this linear system is

$$p_0 = p_L + Z_c \varphi L \, U_L \tag{5.26}$$

where the product $Z_c\varphi L$ represents the series impedance of the pneumatic line and is denoted as

$$Z_s = Z_c \varphi L, \tag{5.27}$$

which accounts for viscous pressure losses along the tube.

To solve the system, it is necessary to impose a boundary condition at the tube outlet, where it is known to have place a transducer. It can be modeled as a compliant volume of gas V_T and, under low-frequency assumption, the transducer impedance can be written as [45]

$$Z_T = \frac{\rho c^2}{i\omega V_T}\frac{k_p}{\gamma} = \frac{\gamma p}{i\omega V_T}\frac{k_p}{\gamma} \tag{5.28}$$

$$= \frac{k_p\, p}{i\omega V_T} = \frac{\beta}{i\omega V_T} = \frac{1}{sC_h} \tag{5.29}$$

where ρ is the fluid density, c is the speed of sound in the fluid, ω is the angular frequency, V_T is the compliant gas volume associated with the transducer, γ is the ratio of specific heats, k_p is the polytropic exponent ($k_p = 1$ for isothermal and $k_p = \gamma$ for adiabatic transformations), p is the mean static pressure, Z_T is the acoustic impedance of the transducer, and C_h is the hydraulic compliance of the transducer volume, defined as $C_h = V_T/(k_p p)$.

Imposing the boundary condition

$$p_L = Z_T U_L, \tag{5.30}$$

the inlet–outlet pressure relation becomes

$$p_0 = p_L \left(1 + \frac{Z_s}{Z_T}\right). \tag{5.31}$$

Therefore, the transfer function between the pressure at the probe inlet and the pressure measured by the transducer is

$$\frac{p_L(s)}{p_0(s)} = \frac{1}{1 + \dfrac{Z_s}{Z_T}}, \tag{5.32}$$

which is formally equivalent to a voltage divider.

Always under the assumption of low frequencies, the series impedance of the tube is dominated by viscous effects and can be modeled as a resistive term, also known as Poiseuille resistance [46]. This resistance calculated for a circular duct of length L and diameter D is given by

$$R = \frac{128\mu L}{\pi D^4}, \tag{5.33}$$

where μ is the dynamic viscosity of the fluid.

With $Z_s = R$ and $Z_T = 1/(sC_h)$, the transfer function becomes

$$\frac{p_L(s)}{p_0(s)} = \frac{1}{1 + sRC_h}, \tag{5.34}$$

which corresponds to a first-order system with time constant

$$\tau = RC_h. \tag{5.35}$$

This formulation highlights the analogy between the pneumatic chain and the electrical RC circuit, where the tube acts as a viscous resistance and the transducer as a compliant volume, as also show in (Fig. 5.19). In this case this volume also contains the tube volume so we need to account for

$$V_{tot} = V_T + V_{tube}. \tag{5.36}$$

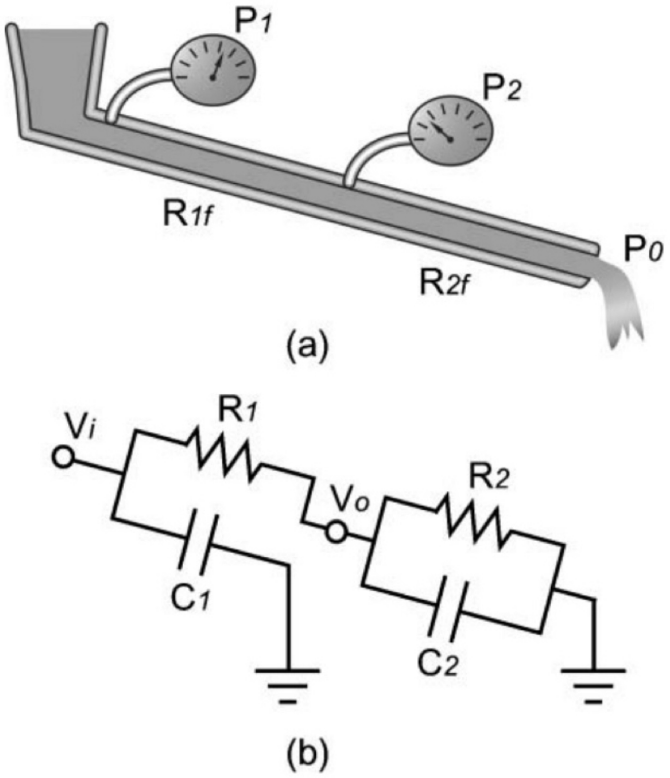

Figure 5.19: Hydraulic–electrical analogy for a pneumatic tubing system, where viscous losses in the tube are modeled as a series resistance and the transducer compliant volume as a capacitance. Adapted from [46].

Once the time constant τ is known, the dwell time should be calculated as

$$t_{\text{dwell}} \geq (3 \div 5)\,\tau, \tag{5.37}$$

in order to ensure that the measured pressure accurately represents the local total pressure at the probe inlet.

To apply this analytical framework to the present experimental setup in order to estimate the required dwell time at each traversing position it is necessary to gather the required data. The pneumatic line from the probe tip to the pressure transducer has a length of $L \approx 160$ mm and an internal diameter of $D \approx 1$ mm. Under the operating conditions in the measurement section, the working fluid has a dynamic viscosity of $\mu \approx 1.7 \times 10^{-5}$ Pa s and a specific heat ratio of $\gamma \approx 1.025$. The mean static pressure level in the measurement section is $p \approx 0.44$ bar. Under these conditions, the viscous Poiseuille resistance of the pneumatic tube is given by

$$R = \frac{128\mu L}{\pi D^4} \approx 1.11 \times 10^8 \text{ Pa s/m}^3, \tag{5.38}$$

The compliant volume of the system is given by the sum of the tube volume and the internal volume of the transducer as reported in 5.36. where $V_{\text{tubo}} \approx 125$ mm^3, while V_T is not precisely known at this stage. Therefore, a parametric analysis has been conducted considering a V_T values range of 50–250 mm^3.

The hydraulic compliance of the system becomes

$$C_h = \frac{V_{\text{tot}}}{\gamma p}. \tag{5.39}$$

The resulting time constant of the pneumatic measurement chain is then obtained as

$$\tau = RC_h. \tag{5.40}$$

In Table 5.4 the resulting values of compliance, time constant, and dwell time required to reach 95% and 99% of the steady-state pressure are summarized.

Table 5.4: Estimated time constant and dwell time of the pneumatic measurement chain for different assumed values of the transducer compliant volume.

V_T [mm^3]	V_{tot} [mm^3]	R [Pa s/m^3]	C_h [m^3/Pa]	τ [ms]	t_{95} [ms]	t_{99} [ms]
50	175	1.11×10^8	3.88×10^{-12}	0.43	1.29	1.98
100	225	1.11×10^8	4.99×10^{-12}	0.55	1.66	2.55
250	375	1.11×10^8	8.32×10^{-12}	0.92	2.76	4.24

From the results, it is possible to notice that even for larger volumes, the dwell time is on the order of a few milliseconds, so the pneumatic system latency is not a limiting factor for the traversing strategy. Therefore, by pausing at each point for approximately 1 ms, the settling time is significantly exceeded and it is possible to acquire a good number of measurements to define a robust average.

5.5 Sealing System

A sealing system is required at the interface between the probe shaft and the test section's process connection, in order to limit leakage and prevent undesired mass exchange between the internal flow and the external environment. Since the test section operates in a subatmospheric environment with a static pressure of approximately 0.44 bar, the primary concern is to limit the ingress of external air. During the traversing operation, the probe shaft is also moved axially, so the selected seal must also be able to accommodate this movement. This means that overall the seal should minimize air inlet and any Siloxane MM leakage, while maintaining low friction on the probe shaft.

5.5.1 Selected Sealing Solution

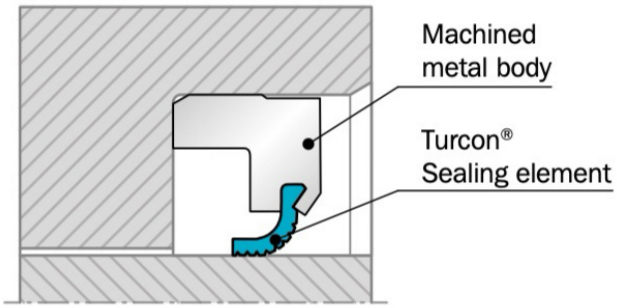

Figure 5.20: Schematic cross-section of a Turcon® Varilip® PDR radial shaft seal [47].

The selected sealing for this application, shown in Fig. 5.20, is a radial shaft seal specifically designed for high temperature environment. This solution consists of a *Turcon® Varilip® PDR* seal, manufactured by *Trelleborg Sealing Solutions* [47], whose part number, TJ A2B 0080 T25 1, identifies a single-lip radial shaft seal with a nominal shaft diameter of 8 mm. The code B represents the bi-directionality of the lip, enabling effectiveness during both insertion and retraction of the probe. The lip material is a PTFE-based compound specifically developed for high-temperature and low-friction applications, and it can withstand up to 250 °C, a temperature where standard elastomeric seals would degrade.

Due to the properties of the lip material, this sealing solution is suitable for high temperature and low lubrication applications, allowing smooth axial motion of the shaft while maintaining effective sealing performance.

Even if the primary sealing requirement is the prevention of air inlet, a bidirectional sealing would ensure redundancy to limit flow paths in both inward and outward directions. To assure this, two identical seals are installed in a back-to-back configuration, allowed by the bi-directionality of the lip.

Overall this solution provides an optimal compromise between thermal resistance, durability, small friction and sealing efficacy.

5.5.2 Integration of the sealing into the process connection

The sealing system needs to be appropriately integrated inside the process connection that hosts the probe shaft. A sectional view of this integration is shown in Figure 5.21, where all the components constituting the assembly are indicated and enumerated following the assembly order.

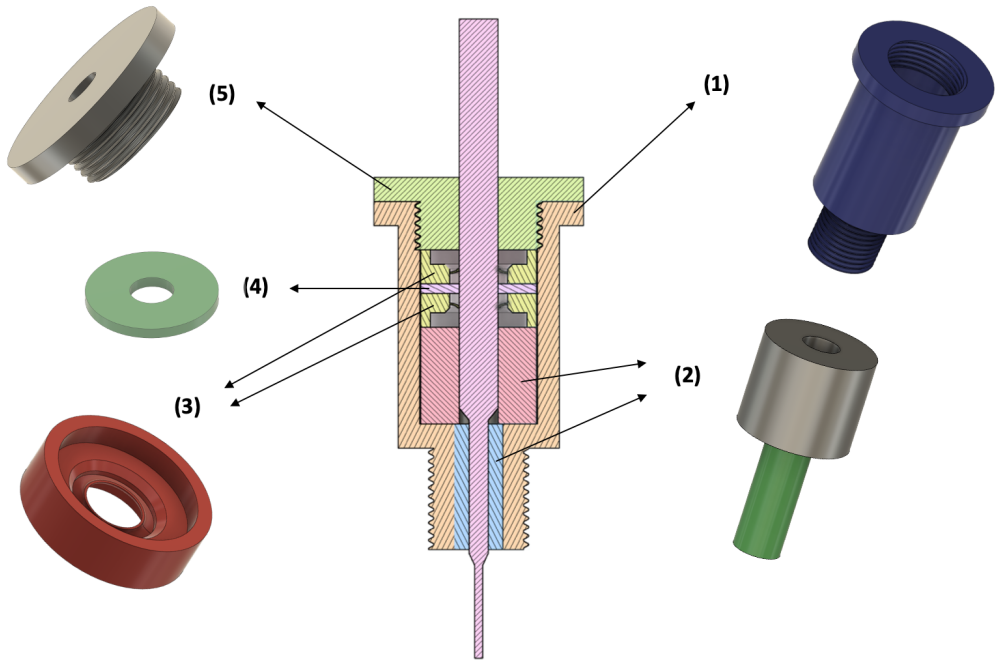

Figure 5.21: Exploded sectional view of the sealing assembly integrated into the process connection.

Their function and role within the assembly are summarized below:

- **Process connection adapter (1)**: this component is required to extend both axially and radially the process connection, in order to create sufficient space to house the sealings. It interfaces with the original G 1/2 process connection and provides an internal G 3/4 threaded bore for the locking ring nut.
- **Guide bushings (2)**: two bushings are installed inside the adapter, the first one with internal diameter of 4 mm and the second one of 8 mm. Their first function is to act as axial spacers, in order to place the sealings at the correct height and ensure that they grip the 8 mm shaft for all positions assumed by the probe during traversing. The secondary function is to provide radial guidance to the probe shaft even if it's deflection is limited. However, if reduced guidance is acceptable, the two bushings may be omitted and replaced by a simple spacer located in place of the top bushing. In this way, the spacer accomplishes the first function without constraining the probe motion.
- **Lip seals (3)**: two lip seals are installed in a back-to-back configuration as previously discussed.

- **Spacer washer (4)**: the washer is placed above the first sealing element to ensure correct axial positioning and distance them.
- **Locking ring nut (5)**: the assembly is secured by a locking ring nut with a G 3/4 male thread which keeps the sealing stack in place and allows disassembly for maintenance.

This integration strategy allows the sealing system to be compatible with the already existing process connection without changing it with permanent modifications.

Chapter 6

Conclusions and Outlook

This thesis focuses on analyizing the flow field downstream of the ORCHID turbine rotor, using numerical evidence as a guideline for designing a custom-built experimental measurement system. The purpose of a future measurement campaign performed with this system is to analyze the performance of the turbine and validate the numerical results. The work was structured and carried out along two parallel and closely interconnected lines: a numerical investigation aimed at understanding the main flow characteristics, and the design of a measurement system compatible with the facility constraints.

The numerical analyses were instrumental to answer the research questions:

Q1 What is the spatial distribution of total pressure at the rotor outlet and how does it evolve up to the measurement plane?

The total pressure field immediately downstream of the rotor is characterized by wakes generated by the rotor blades. Because of this, the total pressure field is non-uniform. Further downstream, these structures mix out so the total pressure can be considered uniform in the pitch-wise direction.

Looking at the measurement plane, the total pressure varies in the radial direction.

This variation dictated the necessity of moving the probe to sample the entire cross-section and reconstruct the pressure profile. For this purpose a traversing mechanism is required.

Q2 To what extent do circumferential flow non-uniformities persist downstream of the rotor and how do they affect the pressure probe selection?

The flow circumferential non-uniformity, calculated for total pressure and entropy, decreases rapidly in the axial direction, demonstrating that the strongest distortions are confined to the proximity of the rotor. At the measurement section, located 60 mm downstream of the rotor, the non-uniformity is already largely attenuated.

In the radial direction, non-uniformity decreases from the wall to the center.

From this result it was possible to state that pneumatic probes are preferred over fast response pressure probes, since a constant averaged value is expected to be recorded.

It should be noted that this conclusion is based only on spatial non-uniformities, since a steady analysis was performed. This means that possible unsteady effects due to temporal variations of the measured quantities could be observed if a non-stationary analysis is performed.

Q3 Are residual swirl and flow angle variations still significant at the measurement plane and what implications do they have for probe type and orientation?

The CFD results show a residual swirl and a strong radial variation of the flow angle that persists along the outlet duct. The velocity field remains highly three-dimensional, suggesting the adoption of a probe less affected by flow angular misalignment.

This led to the choice of a miniaturized Kiel pneumatic probe, whose tip geometry ensures extended angle insensitivity ranges.

The quantified radial distribution of pitch and yaw angles allowed the definition of an optimal probe orientation to not exceed the insensitivity limits of the selected probe.

Answering the research questions allowed to address the overall objective of the work: design a complete total pressure measurement system for the ORCHID turbine rotor outlet.

The proposed solution employs a Kiel-type pneumatic probe mounted together with a suitable pressure transducer, a pneumatic traversing mechanism and a dedicated sealing system, forming a modular system customized to the spatial and safety requirements of the facility.

6.1 Limitations and Recommendations for Future Work

The analyses conducted in this work are based on steady-state CFD simulations with a frozen-rotor interface. At this preliminary stage, this approach has proven to be effective and rapid in identifying mean flow characteristics and relevant spatial trends. However, future work should include the validation of these results by also performing non-steady-state simulations. In particular, unsteady and fully transient RANS simulations would also allow for the temporal aspect of the rotor-stator interaction effects, providing further insight into the dynamics of the propagation of non-uniformities.

Currently, design decisions are based on the assumption that the steady-state simulations performed provide a sufficient initial representation to preliminarily understand the mean flow characteristics.

6.2 Outlook and Future Directions

Before the system can be employed for the experimental campaign, further next steps are required. These include the procurement and assembly of components, the integration of the probe with the pressure transducer and the installation of the probe assembly on the pneumatic traversing mechanism together with the sealings.

The assembled setup will then undergo all the necessary preliminary checks and, in parallel, the traversing system will be programmed and validated to ensure correct probe positioning and movement.

Once operational, this measurement system will enable the acquisition of total pressure in the turbine outlet channel.

Beyond the measurement section addressed here, the proposed setup could also serve for further experimental developments. In particular, additional measurement planes could be introduced both at the diffuser outlet and at positions closer to the rotor exit. Measurements at the diffuser outlet would allow the investigation of how the flow evolves after the diffusion process, while measurements closer to the rotor would provide access to a highly non-uniform flow field dominated by intense wakes.

In particular, in the region close to the rotor outlet, advanced techniques such as fast response aerodynamic pressure probes, discussed in Appendix A, could be adopted in order to investigate the unsteady pressure field and capture the fluctuating components associated with the wake structures.

Concerning the numerical analysis, a possible future development would be the inclusion of the downstream diffuser cone in the computational domain.

The presence of an exhaust diffuser downstream of the rotor improves the performance of the turbine by providing a greater expansion ratio, thus allowing a higher work extraction and efficiency.

A deeper numerical investigation of this component would be instrumental in characterizing the evolution of flow properties throughout the diffusion process and its influence on pressure recovery.

This analysis would open several research questions concerning the diffuser performance, which could also be validated experimentally using the measurement system proposed in this work.

Furthermore, a numerical investigation of the probe head geometry would represent a valuable future development, since the angular insensitivity range and the total pressure recovery of Kiel probes are generally determined in uniform flow conditions.

At present, the behavior of these probes in non-uniform flows with significant flow angle variations is poorly analyzed in the literature.

Therefore, as explained in more detail in Appendix B, a dedicated study would verify whether the nominal angular insensitivity range and the total pressure measurement accuracy of the selected Kiel probe remain valid even under conditions in which flow angle varies within a length scale comparable to the probe head diameter, as expected in the present application.

Overall, this work provides a methodological and experimental framework for the characterization of the flow field downstream of ORC radial-inflow turbines.

By using CFD analyses to guide the design of a dedicated measurement system, the present study establishes the basis for the first experimental investigation of total pressure at the rotor outlet of the ORCHID turbine.

Such measurements would be essential for validating the numerical results and for supporting the evaluation of the turbine performance. The proposed setup could also serve as a reference for future experimental investigations of turbomachinery operating in ORC systems.

Appendix A

Fast-Response Aerodynamic Pressure Probes

A.1 Introduction and Scope

As briefly introduced in Chapter 5, Fast-Response Aerodynamic Pressure Probes (FRAPs) are advanced measurement devices capable to resolve unsteady pressure fluctuations with high frequency response. For this reason they are widely adopted in turbomachinery experimental analysis, since in these applications the flow is often characterized by periodic and high-frequency fluctuations. This technology utilizes miniature piezo-resistive or piezo-electric sensors integrated directly in the probe head, allowing for time resolved measurements of pressure and of three-dimensional flow field.

Looking at the literature, several FRAP configurations have been developed in the past years, starting from the classic design based on multiple pressure sensors mounted on the probe tip. While the multi-hole approach allows for the reconstruction of several flow features such as flow angles, total pressure and static pressure, this solution also involves increased probe head size, manufacturing complexity and blockage effects.

In order to overcome these drawbacks, in the last two decades the research focuses on finding an alternative to reduce the number of sensors while maintaining all the information. The new approach relies on the virtual mode method, through which the information previously provided by a multi-sensor probe is here reconstructed in a post processing phase by combining multiple non-simultaneous measurements taken at different probe orientations. This allows for the reduction of the probe head by employing only one or two sensors, making them suitable for measurements in confined regions. However, this comes with a disadvantage: the post processing reconstruction relies on phase-locked averaging which implies the absence of simultaneous measurements and the loss of part of the turbulent fluctuation.

As discussed in Chapter 5, for the present experimental setup a miniaturized probe is preferred, so the initial investigation among FRAP was focused on virtual mode ones.

Particular attention was devoted to probes developed at Politecnico di Milano and at ETH Zurich, since they carried out two of the most mature and documented research in this field.

The following sections presents a more detailed discussion on:

- the virtual-mode FRAP developed at Politecnico di Milano, particularly referred to the CYL–2b configuration;
- the high-temperature virtual FRAP (FRAP-HT) developed at ETH Zurich and already on market;
- the ETH Zurich virtual FRAP in both V4S and V5S mode.

As pointed out by the CFD results and in particular by the non-uniformity study discussed in Chapter 4, the use of FRAPs is not needed for the selected measurement section since there the flow is sufficiently mixed especially in terms of wakes. Nevertheless, the FRAP technology presented in the following sections can be relevant for future developments where access to a measurement section closer to the rotor can be achieved or modifications to the stem can allow the probe to reach this closer plane.

A.2 Cylindrical Virtual-Mode FRAP (Politecnico di Milano)

Among FRAP technologies, the virtual-mode FRAP in the CYL–2b configuration developed at Politecnico di Milano is one of the most suitable for the present application since it meets the requirements of miniaturization, bandwidth in agreement with blade passing frequency and temperature range. The design of the probe and its use are widely discussed in [33, 36, 48, 49], while its drawing and picture are shown in Figure A.1 .

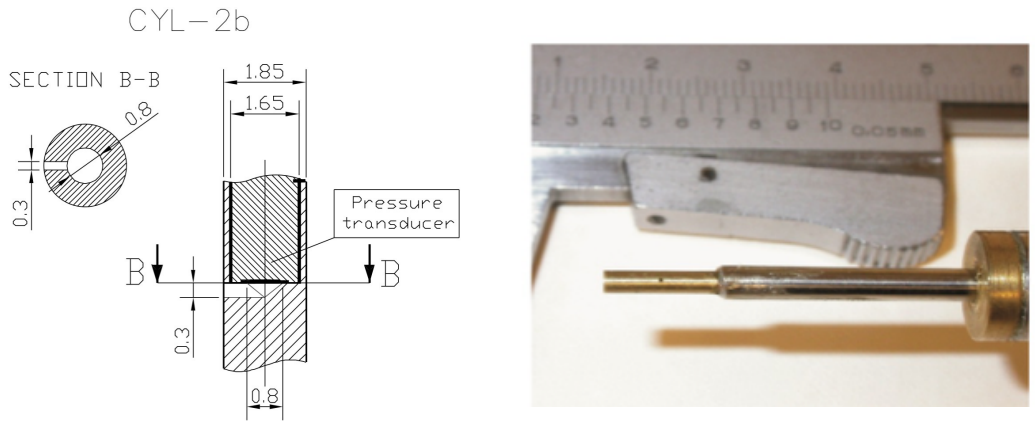

Figure A.1: Cylindrical virtual-mode FRAP (CYL–2b) developed at the Politecnico di Milano. Drawing (left) adapted from [48] and picture (right) adapted from [49]

The CYL–2b configuration presents a cylindric head with a pressure sensor mounted on the lateral surface of the internal probe cavity, rather than in a frontal position. This allows for the reduction of the occupied space and for a further tip miniaturization while maintaining good accuracy. The probe blockage is also reduced by adopting a conical internal cavity instead of a cylindrical one. The tip diameter achieved is only 1.85 mm, making it one of the smallest FRAPs conceived.

Operating in virtual mode, it is capable of resolving two-dimensional flow quantities with only one sensor, giving information about total pressure, static pressure, and yaw angle.

The transducer mounted inside the head is a miniaturized piezoresistive pressure sensor, encapsulated and protected by a RTV coating for high temperature resistance (up to 550 K). The frequency response is on the order of 80 –100 kHz, which is sufficient to resolve unsteadiness associated with blade passing frequencies around 30 kHz, as expected from the ORCHID turbine rotor.

The probe is also quite insensitive to flow angles with yaw angle insensitivity range of $\pm 22.5°$ and pitch angle one of $\pm 10°$.

However, the application of this technology to the present measurement system also finds some limitations. The first one regards the fact that the selected transducer, and all other sufficiently miniaturized, cannot be ATEX certified [16]. In addition, the compatibility of the selected transducer with Siloxane MM has to be verified.

Moreover, since the CYL–2b FRAP application can be useful in a measurement section closer to the rotor outlet, achieving the access to it represents a further limit to overcome.

A.2.1 Virtual Mode Operation: Phase-Locked Averaging and flow reconstruction

The virtual-mode operation allows the CYL–2b FRAP to reconstruct 2D field information by combining measurements acquired at different probe orientations around its longitudinal axis.

The reconstruction of the quantities in post processing is based on the phase-locked averaging concept. Through a key phasor signal, which provides an indication of a complete rotor revolution, it is possible to recognize the time domain and convert it into the phase domain, scaled from $\phi = 0$ to $\phi = 1$.

Then the phase domain is subdivided into several bins and, for each of them, pressure measurements acquired for multiple revolutions are collected and averaged.

In order to obtain the two-dimensional flow reconstruction, the aforementioned process is repeated for three different yaw orientations of the probe. By doing so, for each bin, averaged pressures p_L, p_C, and p_R, corresponding to left, center, and right yaw are collected.

From these three values an initial estimate of static and total pressure can obtained as:

$$p_S^{(0)} = \frac{p_L + p_R}{2}, \qquad p_T^{(0)} = p_C. \tag{A.1}$$

The yaw coefficient defined as

$$K_{\text{yaw}} = \frac{p_L - p_R}{p_T - p_S} \tag{A.2}$$

can be then calculated and referring to the calibration curve of K_{yaw}, shown in Figure A.2, it is possible to extract the local yaw angle. Entering the other two calibrations map in Figure A.2 with the yaw value, also the other two coefficients, defined as follows, can be found:

$$K_{P_T} = \frac{p_T - p_C}{p_T - p_S}, \qquad K_{P_S} = \frac{p_S - \frac{p_R + p_L}{2}}{p_T - p_S}. \tag{A.3}$$

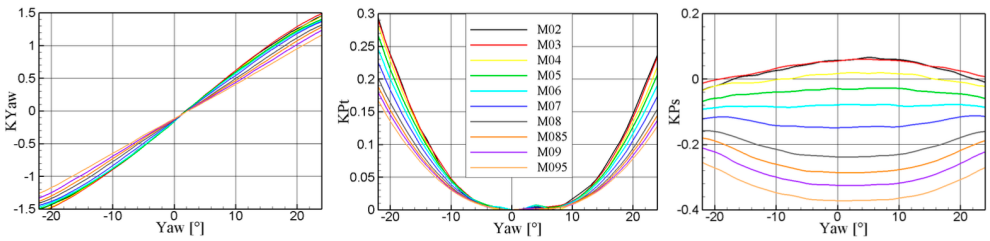

Figure A.2: Calibration curves for the CYL–2b FRAP showing K_{yaw}, K_{P_T}, and K_{P_S} coefficients. Adapted from [36].

By knowing these two values it is then possible to update the first esteems of total and static pressure by solving the system of equations shown in (A.3).

The explained procedure is iterated by recomputing K_{yaw} with the updated values until convergence, as described in detail in [36].

A.3 High-Temperature FRAP (ETH Zurich)

Another interesting solution among FRAPs operating in virtual mode is the High-Temperature Fast Response Aerodynamic Probe developed at ETH Zurich and discussed in [34]. This probe is conceived to operate in harsh environments, characterized by high temperatures, since it is capable to withstand up to 533 K. This is possible due to coating strategy of the transducer and dedicated thermal management.

The FRAP-HT has a head diameter of 2.5 mm, slightly larger than the CYL–2b one discussed before but still categorizable as miniaturized. The angular insensitivity range for this probe is approximately ±24° for the yaw and ±20° for the pitch, while the bandwidth is around 25 kHz, which can be sufficient to resolve unsteady pressure in many turbomachinery applications.

The sensing part of this FRAP is made up of two miniaturized piezoresistive silicon pressure transducers mounted in the the probe shaft and capable of measuring both steady and unsteady pressure. An additional temperature sensor is integrated in the shaft in order to control temperature level and correct the heat flux, ensuring an improved thermic management.

This FRAP operates in virtual-mode allowing the reconstruction of flow angles, total and static pressure, Mach number and static temperature.

The three dimensional flow reconstruction is enabled by two pressure taps sensitive to flow angles. The yaw-sensitive pressure tap is located on the stem, while the pitch-sensitive one is on the probe tip, on a surface tilted of 45°.

In Figure A.3 it is possible to see the probe geometry and the location of the two taps.

Figure A.3: High-temperature FRAP developed at ETH Zurich [34].

A.3.1 Virtual four-sensor (4VS) operating principle

During the measurement phase the probe stem is sequentially rotated around its axis in three different positions, at 0°, +42°, and −42°. The yaw pressure tap measures the pressure in each position, while the pitch tap is used only at the central position. Figure A.4 shows the virtual-mode strategy employed by this probe.

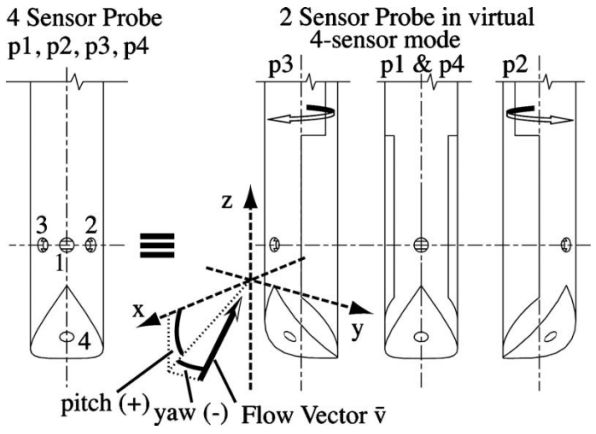

Figure A.4: FRAP-HT Virtual four-sensor operating strategy: rotation at 0°, +42° and −42° [34].

By doing this, four pressure signals are detected and then used in the post processing phase to reconstruct three-dimensional flow information, similarly to what discussed in the previous paragraph. According to it, the reconstruction starts from an initial estimate of total and static pressure and then iterates until convergence is reached, calculating all the other quantities referring to the calibration coefficients.

These coefficients are here defined as [34]:

$$K_\phi = \frac{p_2 - p_3}{p_1 - p_m}, \quad K_\gamma = \frac{p_1 - p_4}{p_1 - p_m}, \tag{A.4}$$

$$K_T = \frac{p_{tot} - p_1}{p_1 - p_m}, \quad K_S = \frac{p_1 - p_{stat}}{p_1 - p_m}, \tag{A.5}$$

with

$$p_m = \frac{p_2 + p_3}{2}.$$

This FRAP-HT technology is already on market, representing a practical advantage with respect to university prototypes.

A.4 Virtual Four Sensor FRAP (ETH Zurich)

A similar FRAP technology developed at ETH Zurich is the Virtual Four Sensor (V4S) probe, described in [37]. The working principle is similar to that of the HT-FRAP but the two sensors are mounted on two separate probes that work in tandem, as shown in Figure A.5. In order to emulate a real four-sensor probe, the first probe is yaw-sensitive and is rotated into three positions about the stem axis, while the second one is pitch-sensitive and acquires only one measurement in a fixed position.

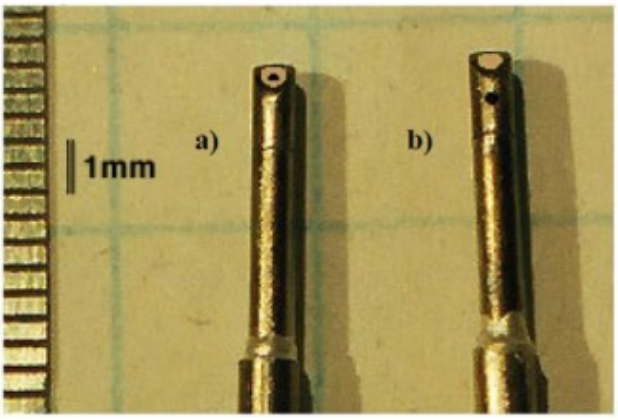

Figure A.5: a) pitch angle sensitive probe and b) yaw angle sensitive probe forming the Virtual Four Sensor (V4S) configuration developed at ETH Zurich [37].

All four pressure signals are phase-locked and post processed in order to obtain yaw and pitch angles, total pressure and static pressure.

A relevant feature of these probes is the miniaturization of the tip, which has an outer diameter of 0.84 mm. The cylindrical head has been optimized to reduce blockage at the cost of an increased manufacturing complexity. Around 40 different mechanical and micro-mechanical steps of several hours each are necessary to build one probe for an amount of 500 hours per probe [37].

The frequency response is up to 25kHz, covering flow angles ranges of $\pm 30°$ for yaw and $-30°$ to $+21°$ for pitch. The accuracy level for flow angles and pressure measurements is acceptable especially at moderate Mach numbers.

A.5 Virtual Five Sensor FRAP (ETH Zurich)

An alternative development from ETH Zurich is the single pressure transducer probe described in [38] and shown in Figure A.6. Only one pressure transducer is mounted inside the probe shaft and, by rotating the probe around its stem axis in five consecutive positions, the 3D flow vector can be reconstructed.

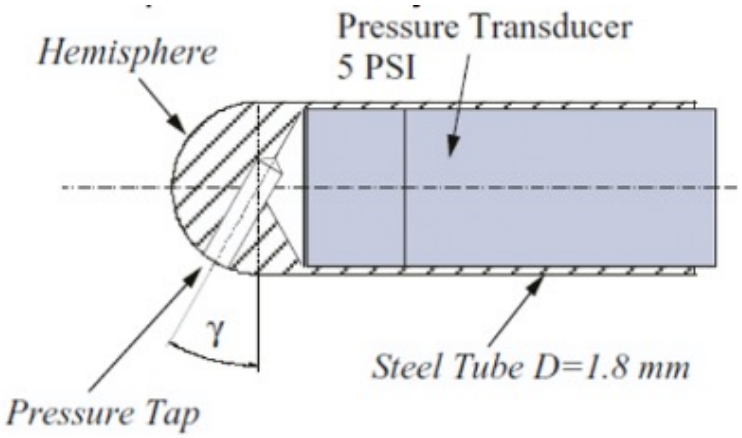

Figure A.6: Single pressure transducer probe operating in Virtual Five-Sensor (V5S) mode developed at ETH Zurich. Adapted from [38].

During data post-processing, the five measured pressures are plotted relative to the corresponding probe angle, as shown in Figure A.7. An interpolation curve of fourth-degree is fitted to the data set in order to find the peak pressure. This estimated value is used to define yaw and pitch calibration coefficients, useful to define yaw and pitch angles, total pressure, static pressure and Mach number [38].

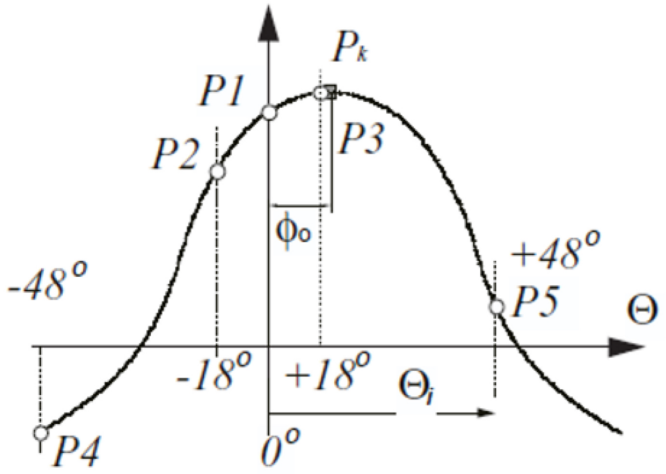

Figure A.7: Interpolation procedure used to estimate the peak pressure from five angularly distributed measurements. Adapted from [38].

Different head geometries (hemispherical and ellipsoidal) and pressure tap inclinations were analyzed to optimize pitch sensitivity and revealed that the model accuracy for the pitch angle is 3-4 times less than one would expect from a cylindrical

multi-hole. However, one of the main advantages of this solution is the simplicity and miniaturization of the geometry, compared to multi-hole or multi-sensor probes.

The simple design of the probe leads to a large internal cavity between pressure tap and transducer membrane, causing a resonance frequency limited to 13 kHz.

Appendix B

CFD Analysis of Kiel Probes in Non-Uniform Flow Conditions

B.1 Motivation and Problem Definition

In the present work, the total pressure is planned to be measured through a Kiel probe, selected for its wide insensitivity range to flow angle. As deducted from CFD results reported in Chapter 5, the analyzed flow presents steep gradients of yaw angle in the radial direction at the measurement section.

The insensitivity range of Kiel probes is assessed and verified in uniform flow conditions where the flow angle remains the same for all the extent. This means that their performance is not well known in highly non-uniform flows as that of the case presented here, where the flow angle varies even over a length comparable to the probe head diameter. For this reason, a preliminary literature review was conducted to investigate previous studies addressing the behavior of Kiel probes, in order to find out if any analysis in these flow conditions already exists. Another aim is also that of identifying the usual strategies for CFD analysis of Kiel probes.

In this appendix the findings of this literature review are summarized and a possible numerical approach for future investigations is presented.

B.2 RANS Modeling of Kiel Probes

The first work considered is presented in [50] where a numerical investigation of a complex Kiel probe has been pursued. In particular, this study is focused on the application of RANS models to accurately predict the flow behavior inside the probe head.

B.2.1 Geometrical Modeling and Mesh Requirements

The first thing to model in order to numerically analyze the probe is its geometry, which is often simplified to limit computational cost and mesh complexity. This simplification regards in particular the inner pipe which is actually hollow but is

represented by a plenum region where the flow is brought to stagnation. This approach allows the total pressure to be evaluated as the static pressure recorded in the stagnation region, without the need for modeling the inner channel.

The geometry considered in [50] is more complex than the one employed for the ORCHID turbine Kiel probe, as it includes bleed holes and a non-axisymmetric plenum. Nevertheless, it's still possible to adapt the modeling philosophy to the present case.

After modeling the geometry, the second step is that of the mesh definition. Here is fundamental to accurately resolve the boundary layers and near-wall regions, particularly inside the probe head where the sensing zone is placed. From the results obtained in [50] it is possible to deduce that a resolution of the boundary layer with $\Delta y^+ \approx 1$ is recommended for a better accuracy, conversely the use of wall functions is discouraged even if it is a faster and simpler approach.

In Figure B.1 the mesh strategy adopted in this study is reported. A strong refinement near the probe walls and within the internal region and holes is clearly visible.

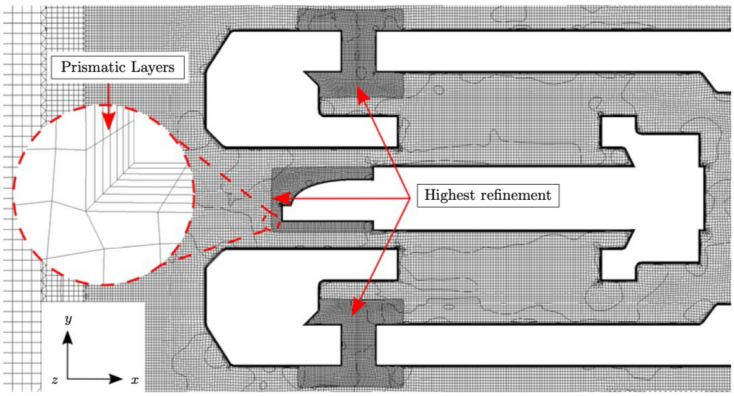

Figure B.1: Example of near-wall mesh refinement for a Kiel probe, adapted from [50].

B.2.2 Turbulence Modeling and Corrections

Always referring to [50], among the turbulence models, the RNG k–ε model seems to give most similar results to the experimental data, after applying some corrections.

The first correction applied is to consider the strong streamline curvature that the flow undergoes due to the probe geometry. This causes the overestimation of the production term of turbulent kinetic energy which needs to be limited through the application of a curvature correction.

The second correction is needed to counteract the overestimation of turbulent kinetic energy in stagnation regions, where specific limiters are required. These limiters can be found in the Kato–Launder correction or in the Menter limiter.

By applying these corrections, the velocity at the stagnation point approaches zero more accurately, allowing for a more realistic estimation of total pressure.

B.3 CFD Studies on Realistic Kiel Probe Geometries

Another perspective on Kiel probes numerical analysis is given by the study reported in [51], focused on the numerical simulation of a Kiel probe installed upstream of a high-pressure compressor.

In this work, the internal geometry of the probe is more similar to that of our case, with the inner tube modeled as a plenum as well. As in the previous study, in this numerical set-up, similar mesh structure and model corrections are adopted.

Figure B.2 illustrates the mesh approach for the probe head, similar to that of the study discussed in the previous paragraph.

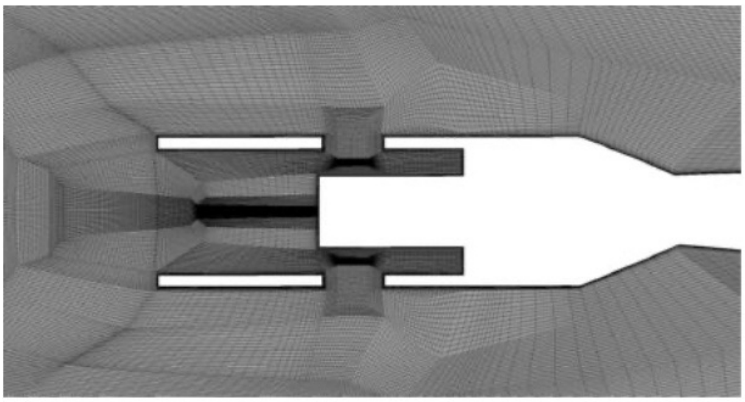

Figure B.2: Mesh example for a Kiel probe head, adapted from [51].

Although the primary objective of this study is to quantify the influence of increasing head dimensions on induced losses, it provides important insights on geometry modeling, meshing strategy and turbulence corrections for Kiel probe CFD simulations.

Further numerical investigations, such as those presented in [52] and [53], are focused on the interactions in Kiel probe rakes using k–ω SST turbulence model. These studies address probe interference effects so their objectives are different from the present application. Nevertheless, they are mentioned since their approach is in line with the previously discussed modeling trend.

B.4 Implications for the ORCHID Application and Future Work

The literature review confirms that existing CFD studies of Kiel probes are almost exclusively limited to uniform flow conditions, with constant flow angle over the probe head.

This means that for our application, where yaw angle varies over scales comparable to the probe diameter, the angle insensitivity range provided by the probe manufacturer and derived from calibration in uniform flow may be slightly different than the actual one.

To further analyze this aspect, a CFD analysis of the Kiel probe head immersed in a non-uniform flow field, could be meaningful. The numerical model should follow the guidelines presented in literature but it can be performed only once the detailed internal geometry of the selected probe's head becomes available.

In order to reproduce the right flow conditions and catch the local flow-angle gradients, a subdomain should be extracted from the existing outlet duct domain. Then, simulations with and without the probe could be performed and compared in order to calculate an index called recovery factor.

This index is equal to the ratio between the stagnation pressure measured at the probe head and the total pressure obtained at the same point in the simulation without the probe. It indicates the entity of the flow distortion induced by the probe interference, since the more this factor is close to unity, the higher is the accuracy of the Kiel probe measurement.

This analysis can be repeated for different yaw orientations of the probe, with the aim of verifying whether the nominal angle insensitivity remains unchanged even in strongly non-uniform flows. This study would provide further insight on the reliability of Kiel probe measurements under ORC turbine outlet conditions and would validate the accuracy of the experimental design proposed in this thesis.

Appendix C

Traversing System: Alternative Solution

The solution most commonly adopted by facilities implementing a probe traversing mechanism is the one based on linear actuators driven by electric motors. Indeed, these systems offer positioning accuracy and control flexibility, making them the first option considered in this study.

However, despite these advantages, the availability of ATEX-certified electrical components is limited to devices oversized for the force and speed required for the selected probe movement.

Therefore, the electric translation system was retained as a secondary option and is discussed in the following sections for completeness, analyzing its individual components in more detail.

C.1 Electric Motor and Servo-Drive

One of the smallest ATEX-certified electric motors currently available on the market is the MRSH064A-105 servo motor manufactured by *WITTENSTEIN cyber motor GmbH* [54], shown in Figure C.1. This motor has a built-in resolver for closed-loop position control and must be interfaced with a suitable servo-drive, individuated in the SINAMICS S120 model manufactured by *Siemens* [55]. One of the downsides is that the certified electric cables for power supply, connection to the drive, and temperature monitoring are not included with the motor and must be selected separately, increasing the complexity of the system and its integration.

As already mentioned, another important disadvantage of this solution is the significant over-sizing of the motor compared to the requirements for the probe's movement. In fact, the nominal torque delivered by this motor is on the order of several Newton-meters and exceeds by two orders of magnitude the torque required by the traversing mechanism, if a reasonably sized actuator was considered. The major problem is that, while the rotational speed can be limited via servo-drive, the torque delivered cannot be reduced below a certain threshold, represented by the cogging torque. Indeed, if the torque falls below this limit, it might not be sufficient

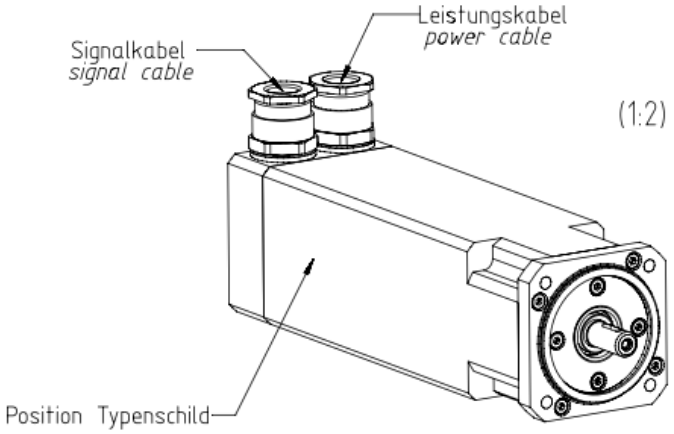

Figure C.1: ATEX-certified electric motor Wittenstein MRSH064A-105

to compensate the internal friction and bearing losses. Complicating matters is the fact that all linear guide actuators sized to fit our system require a maximum torque below the cogging torque in order to avoid damaging of the structure, which also results in an oversize actuator.

The electric motor and the actuator are manufactured by different companies so the system would also require a tailored joint to adapt the motor shaft to the linear slide shaft. This additional component would add potential risk of misalignment and lower reliability.

For as regards dimensions, the motor exhibits a relatively high mass (4.1 kg) and a frame size significantly larger than what would be expected for an actuator correctly dimensioned for this application. In particular this motor would be approximately six times larger than one matched to the required force and torque.

C.2 Motor-Driven Linear Slide Actuator

After careful research to select a suitable solution in terms of both size and robustness, a valid candidate was identified in the PSD80 screw-driven linear actuator produced by *HepcoMotion Ltd.* [56] and shown in Fig. C.2. Among commercially available guided slides, this one offers a good compromise between mechanical robustness and compactness with the capability of withstanding both the rated torque and the mass of the selected motor.

The selected configuration (part number PSD80 L257 TCD 15) features a closed-body design with a trapezoidal screw drive of 15 mm pitch. This pitch was chosen among the various available screw pitches (4, 15, 25, and 70 mm) since it was the best tailored for the motor coupling. Although the smaller 4 mm pitch provides finer positioning resolution, it generates a high linear force for small motor torques. Consequently, for the linear force needed for the application, the torque required by the motor would fall below the cogging torque. For this reason, a 15 mm pitch was selected, allowing operation at higher torques while maintaining adequate accuracy.

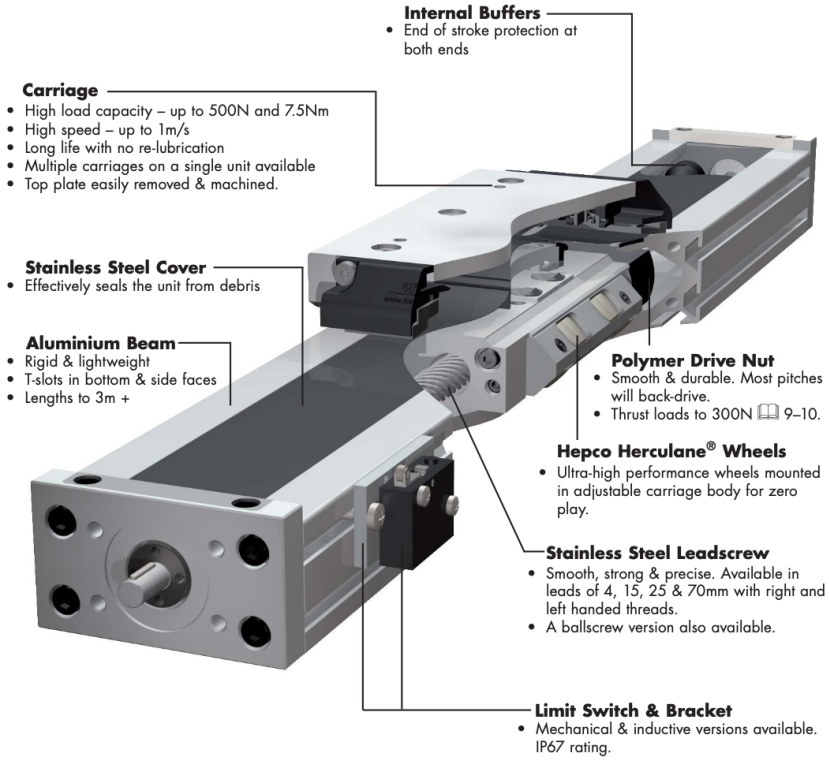

Figure C.2: Schematic overview of the HepcoMotion PSD80 screw-driven linear actuator, highlighting the main components and integrated features [56].

As shown in figure, the PSD80 features a robust carriage suitable for mounting the probe, mechanical limit stops, and selectable inductive limit switches. The option of choosing non-contact inductive limit switches over electric ones is a significant advantage in terms of ATEX certification, as they are intrinsically compatible with operation in hazardous environments.

Since the actuator has no electrical or ignition-risk parts, it does not require additional safety certifications.

By choosing this actuator, there is also the possibility to include on request a connection kit for the chosen motor. This kit includes the motor flange and the coupling joint that connects the motor shaft to the actuator screw. The big advantage of this option is the increase in mechanical reliability and precision of the assembly, where an incorrect coupling would have caused misalignment and lateral loads.

Compared to the pneumatic solution, the electric solution's linear slide alone occupies a volume comparable to the whole pneumatic actuator. Combined with the electric motor, the assembly is significantly bulkier and heavier, further justifying the selection of the pneumatic actuation option for the final design.

Bibliography

[1] M. Astolfi et al. *Thermal Energy Harvesting: the Path to Tapping into a Large CO2-free European Power Source*. Technical White Paper. Version 2.0. KCORC Knowledge Center on Organic Rankine Cycle Technology, 2025. DOI: https://doi.org/10.17185/duepublico/82887 (cit. on p. 1).

[2] M. Majer. "Supersonic Organic Rankine Cycle Radial–Inflow Turbines for On-board Thermal Energy Harvesting". PhD thesis. Delft University of Technology, 2025 (cit. on pp. 1, 3, 7, 12, 14, 16, 41, 42, 47, 48).

[3] P. Colonna, E. Casati, C. Trapp, T. Mathijssen, J. Larjola, T. Turunen-Saaresti, and A. Uusitalo. "Organic Rankine Cycle Power Systems: From the Concept to Current Technology, Applications, and an Outlook to the Future". In: *Journal of Engineering for Gas Turbines and Power* 137.10 (2015), p. 100801. DOI: https://doi.org/10.1115/1.4029884 (cit. on pp. 1, 3–5).

[4] A. Perdichizzi and G. Lozza. "Design Criteria and Efficiency Prediction for Radial Inflow Turbines". In: *Proceedings of the ASME Turbo Expo*. Anaheim, California: American Society of Mechanical Engineers, 1987. DOI: https://doi.org/10.1115/87-GT-231 (cit. on p. 1).

[5] H. E. Rohlik. *Analytical determination of radial inflow turbine design geometry for maximum efficiency*. National Aeronautics and Space Administration, 1968 (cit. on p. 1).

[6] C. De Servi, M. Burigana M. Pini, and P. Colonna. "Design Method and Performance Prediction for Radial-Inflow Turbines of High-Temperature Mini-Organic Rankine Cycle Power Systems". In: *Journal of Engineering for Gas Turbines and Power* 141.9 (2019), p. 091021. DOI: https://doi.org/10.1115/1.4043973 (cit. on pp. 1, 7).

[7] M. Manfredi, A. Spinelli, and M. Astolfi. "Definition of a general performance map for single stage radial inflow turbines and analysis of the impact of expander performance on the optimal ORC design in on-board waste heat recovery applications". In: *Applied Thermal Engineering* 224 (2023), p. 119857. DOI: https://doi.org/10.1016/j.applthermaleng.2022.119857 (cit. on p. 1).

[8] E. Macchi and M. Astolfi. *Organic Rankine Cycle (ORC) Power Systems: Technologies and Applications*. Woodhead Publishing, 2016 (cit. on p. 3).

[9] A. Guardone, P. Colonna, M. Pini, and A. Spinelli. "Nonideal Compressible Fluid Dynamics of Dense Vapors and Supercritical Fluids". In: *Annual Review of Fluid Mechanics* 56 (2024), pp. 241–269. DOI: https://doi.org/10.1146/annurev-fluid-120720-033342 (cit. on pp. 5, 6).

[10] P. A. Thompson. "A Fundamental Derivative in Gasdynamics". In: *The Physics of Fluids* 14.9 (1971), pp. 1843–1849. DOI: https://doi.org/10.1063/1.1693693 (cit. on p. 5).

[11] A. Whitfield and N. C. Baines. *Design of Radial Turbomachines*. Longman Scientific & Technical, 1990 (cit. on p. 6).

[12] M. V. Casey. "Radial Turbomachinery Design". In: *Journal of Turbomachinery* (2012) (cit. on p. 6).

[13] O. Balje and D. Japikse. "Turbomachines—a guide to design selection and theory". In: *ASME Journal of Fluids Engineering* 103.4 (1981), pp. 644–644 (cit. on p. 8).

[14] C. De Servi, E. Casati, A. J. Head, M. Pini, and P. Colonna. "Preliminary Design of the ORCHID: A Facility for Studying Non-Ideal Compressible Fluid Dynamics and Testing ORC Expanders". In: *Turbo Expo: Power for Land, Sea, and Air*. Vol. 49743. American Society of Mechanical Engineers. 2016, V003T25A001. DOI: https://doi.org/10.1115/GT2016-56103 (cit. on p. 7).

[15] Adam Joseph. Head. "Novel Experiments for the Investigation of Non-Ideal Compressible Fluid Dynamics". PhD thesis. Delft University of Technology, 2021 (cit. on pp. 9, 10).

[16] *Directive 2014/34/EU of the European Parliament and of the Council of 26 February 2014 on the harmonisation of the laws of the Member States relating to equipment and protective systems intended for use in potentially explosive atmospheres*. Official Journal of the European Union, L 96. 2014 (cit. on pp. 9, 63, 89).

[17] T. Jespen. *ATEX—Explosive Atmospheres. Risk Assessment, Control and Compliance*. 1st ed. Springer Series in Reliability Engineering. According to the ATEX Directive 2014/34/EU, Zone 2 denotes an area in which an explosive atmosphere is not likely to occur in normal operation and, if it does occur, will persist for a short period only. Temperature class T2 specifies a maximum permissible surface temperature of 300°C, ensuring safe operation in the presence of flammable gases or vapours with auto-ignition temperatures above this limit. Cham: Springer, 2016. ISBN: 978-3-319-31367-2. DOI: 10.1007/978-3-319-31367-2 (cit. on pp. 9, 65).

[18] ANSYS Inc. *Ansys® TurboGrid*. Academic Research, Release 2024 R2. ANSYS Inc., Canonsburg, PA, USA. 2024 (cit. on p. 16).

[19] T. J. Barth and D. C. Jespersen. "The Design and Application of Upwind Schemes on Unstructured Meshes". In: *Proceedings of the 27th AIAA Aerospace Sciences Meeting*. Reno, NV, USA: American Institute of Aeronautics and Astronautics, 1989. DOI: https://doi.org/10.2514/6.1989-366 (cit. on p. 16).

[20] ANSYS Inc. *Ansys® CFX*. Academic Research, Release 2024 R2. ANSYS Inc., Canonsburg, PA, USA. 2024 (cit. on p. 16).

[21] ANSYS Inc. *ANSYS® CFX Solver Modeling Guide*. 2025 (cit. on pp. 17, 27).

[22] ANSYS Inc. *ANSYS® BladeGen*. Academic Research, Release 2024 R2. 2024 (cit. on p. 22).

[23] T. S. Phillips and C. J. Roy. "Richardson extrapolation-based discretization error estimation for computational fluid dynamics". In: *Journal of Fluids Engineering* 136.12 (2014), p. 121401. DOI: https://doi.org/10.1115/1.4027353 (cit. on pp. 31–33).

[24] A. Cappiello and R. Tuccillo. "Design Parameter Influence on Losses and Downstream Flow Field Uniformity in Supersonic ORC Radial-Inflow Turbine Stators". In: *International Journal of Turbomachinery, Propulsion and Power* 6.3 (2021), p. 38. DOI: https://doi.org/10.3390/ijtpp6030038 (cit. on p. 36).

[25] The MathWorks, Inc. *MATLAB*. Release R2024b. 2024 (cit. on p. 37).

[26] R. W. Armentrout and J. C. Kicks. "Pressure Instrumentation for Gas Turbine Engines - a Review of Measurement Technology". In: *American Society of Mechanical Engineers* (1979) (cit. on pp. 49–52).

[27] *Pressure Measurement – Instruments and Apparatus*. Section 4: Pressure probes and measurement techniques. American Society of Mechanical Engineers. 1988 (cit. on pp. 49–51, 54).

[28] S. H. Chue. "Pressure probes for fluid measurement". In: *Progress in Aerospace Sciences* 16 (1975), pp. 147–223. DOI: https://doi.org/10.1016/0376-0421(75)90014-7 (cit. on pp. 49–52).

[29] C. H. Sieverding, T. Arts, J. F. Brouckaert, and R. Van den Braembussche. *Measurement Techniques for Unsteady Flows in Turbomachines*. Vol. 28. 4. Springer, 2000, pp. 285–321. DOI: https://doi.org/10.1007/s003480050390 (cit. on pp. 49, 52).

[30] O. K. Redinotis. *Novel, Miniature Multi-Hole Probes and High Accuracy Calibration Algorithms for Their Use in Compressible Flowfields*. Tech. rep. NASA/TM–1999-209643. NASA, 1999 (cit. on p. 52).

[31] I. Jonsson and B. Legrady. "Multi-hole probe: A review and a new take to improve accuracy". In: (2024). DOI: https://doi.org/10.21203/rs.3.rs-4801492/v1 (cit. on p. 52).

[32] R. Jangir, N. Sitaram, and C. Ganjanan. “A Miniature Four-Hole Probe for Measurement of Three-Dimensional Flow with Large Gradients”. In: *International Journal of Rotating Machinery* 2014.1 (2014), p. 297861. DOI: https://doi.org/10.1155/2014/297861 (cit. on p. 52).

[33] A. Notaristefano, P. Gaetani, and G. Persico. “Turbulence Measurements in Axial Turbines Using Fast Response Aerodynamic Pressure Probes”. In: *Journal of Turbomachinery* 147.8 (2025), p. 081012. DOI: https://doi.org/10.1115/1.4067440 (cit. on pp. 52, 53, 88).

[34] C. Lenherr, A. I. Kalfas, and R. S. Abhari. “High-Temperature Fast-Response Aerodynamic Probe”. In: *Journal of Engineering for Gas Turbines and Power* 133.3 (2011), p. 011603. DOI: https://doi.org/10.1115/1.4001824 (cit. on pp. 52, 90–92).

[35] P. Kupferschmied, C. Gossweiler, and G. Gyarmathy. “Aerodynamic Fast-Response Probe Measurement Systems: State of Development, Limitations and Future Trends”. In: *Proceedings of the 12th Symposium on Measuring Techniques for Transonic and Supersonic Flows in Cascades and Turbomachines*. Prague, Czech Republic, 1994, pp. 12–13 (cit. on p. 53).

[36] G. Persico and P. Gaetani. “Technology Development of Fast-Response Aerodynamic Pressure Probes”. In: *International Journal of Turbomachinery, Propulsion and Power* 5.2 (2020), p. 6. DOI: https://doi.org/10.3390/ijtpp5020006 (cit. on pp. 53, 88, 90).

[37] A. Pfau, J. Schlienger, A. I. Kalfas, and R. S. Abhari. “Virtual Four-Sensor Fast-Response Aerodynamic Probe”. In: *E3S Web of Conferences* 345 (2022), p. 041006. DOI: https://doi.org/10.1051/e3sconf/202234501014north_east (cit. on pp. 53, 92).

[38] J. Schlienger, A. Pfau, A. I. Kalfas, and R. S. Abhari. “Single Pressure Transducer Probe for 3D Flow Measurements”. In: *E3S Web of Conferences* 345.8 (2022), p. 01012. DOI: https://doi.org/10.1051/e3sconf/202234501012 (cit. on pp. 53, 93).

[39] S. D. Grimshaw and J. V. Taylor. “Fast Settling Millimitre-scale Five Hole Probes”. In: *Turbo Expo: Power for Land, Sea, and Air*. Vol. 49828. American Society of Mechanical Engineers. 2016, V006T05A014. DOI: https://doi.org/10.1115/GT2016-56628 (cit. on p. 55).

[40] Aero Sensor Ltd. *KP12 Micro-Kiel Probe — Manufacturer Technical Documentation*. https://aerosensor.tech/pages/micro-kiel-probes. Manufacturer technical documentation, accessed February 2026. 2024 (cit. on pp. 57, 59).

[41] WIKA Alexander Wiegand SE & Co. KG. *Pressure Transmitter, Model IS-3*. https://www.wika.com/en-ca/is_3.WIKA. Manufacturer technical documentation, accessed February 2026. 2024 (cit. on pp. 63, 64).

[42] Festo BV. *Technical Documentation and Product Specifications*. https://www.festo.com. Manufacturer technical documentation, accessed February 2026. 2024 (cit. on pp. 66–71).

[43] National Instruments. *CompactRIO Embedded Control and Acquisition Systems — Hardware Specifications and User Documentation*. https://www.ni.com. Manufacturer technical documentation, accessed February 2026. 2024 (cit. on p. 72).

[44] B. W. Richards. *Propagation of Sound Waves in Tubes of Noncircular Cross Section*. Tech. rep. NASA TP-2601. NASA, 1986 (cit. on p. 76).

[45] M. Kovarek, L. Amatucci, K. A. Gillis, F. A. Potra, J. Ratino, M. Levitan, and D. Yeo. "Calibration of Dynamic Pressure in a Tubing System and Optimized Design of Tube Configuration: A Numerical and Experimental Study". In: *National Institute of Standards and Technology NIST* (1994). DOI: https://doi.org/10.6028/NIST.TN.1994 (cit. on p. 76).

[46] D. Kim, N. C. Chesler, and D. J. Beebe. "A Method for Dynamic System Characterization Using Hydraulic Series Resistance". In: *Lab on a Chip* 6.5 (2006), pp. 639–644. DOI: 10.1039/B517054K (cit. on pp. 77, 78).

[47] Trelleborg Sealing Solutions. *Technical Documentation and Product Specifications*. https://www.trelleborg.com. Manufacturer technical documentation, accessed February 2026. 2024 (cit. on p. 80).

[48] G. Persico, P. Gaetani, and A. Guardone. "Design and analysis of new concept fast-response pressure probes". In: *Measurement Science and Technology* 16.9 (2005), pp. 1741–1750. DOI: 10.1088/0957-0233/16/9/005 (cit. on p. 88).

[49] L. Toni, V. Ballarini, P. Gaetani, and G. Persico. "Unsteady Flow Field Measurements in an Industrial Centrifugal Compressor". In: *Proceedings of the thirty-ninth turbomachinery symposium* (2010) (cit. on p. 88).

[50] B. N. Ubald, P. G. Tucker, and S. Shahpar. "Assessment of RANS Modelling for a Complex Stagnation Probe Case". In: *55th AIAA Aerospace Sciences Meeting*. 2017, p. 1229 (cit. on pp. 95, 96).

[51] L. Schäflein, D. Jung, S. Henninger, P. Jeschke, and R. Wunderer. "Impact Of Leading-Edge Probes on the Loss of s High Pressure Compressor Vane in a Linear Cascade". In: *Proceedings of Global Power and Propulsion Society*. GPPS, 2025 (cit. on p. 97).

[52] A. Lahalle, F. Fontaneto, and T. Arts. "CFD Driven Analysis of a Multi-Port Pressure Probe for Real Engine Testing". In: *Turbo Expo: Power for Land, Sea, and Air*. Vol. 50794. American Society of Mechanical Engineers. 2017, V02BT41A030 (cit. on p. 97).

[53] L. Bhatnagar, G. Paniagua, D. G. Cuadrado, P. N. A. Aye-Addo, A. Castillo Sauca, F. Lozano, and M. Bloxham. "Uncertainty in High-Pressure Stator Performance Measurement in an Annular Cascade at Engine Representative Reynolds and Mach". In: *Journal of Engineering for Gas Turbines and Power* 144.2 (2022), p. 021001. DOI: https://doi.org/10.1115/1.4052385 (cit. on p. 97).

[54] WITTENSTEIN cyber motor GmbH. *MRSH064A-105 Servo Motor — MRSH Series, ATEX-Certified*. https://cyber-motor.wittenstein.de. Manufacturer technical documentation, accessed February 2026. 2024 (cit. on p. 99).

[55] Siemens AG. *SINAMICS S120 Modular Drive System — Motion Control and Safety Documentation*. https://www.siemens.com. Manufacturer technical documentation, accessed February 2026. 2024 (cit. on p. 99).

[56] HepcoMotion Ltd. *PSD80 Heavy Duty Linear Actuator — Technical Catalogue and Product Documentation*. https://www.hepcomotion.com/. Manufacturer technical documentation, accessed February 2026. 2024 (cit. on pp. 100, 101).

Acknowledgments

I would like to sincerely thank Prof. Piero Colonna for the trust he placed in me and for giving me the opportunity to contribute to the research at the ORCHID Facility here at TU Delft. Being part of this research group has been an enriching experience that greatly contributed to my academic and personal growth.

I am particularly grateful to Dr. Matteo Majer for his constant guidance and support throughout this path. His careful supervision was essential in shaping the direction of this research and bringing it to the present state.

I would also thank Prof. Emanuele Martelli, my supervisor at Politecnico di Torino, for supporting me in undertaking this research in collaboration with TU Delft.

Finally, I would like to express my deepest gratitude to my family and friends for their constant encouragement and support throughout my studies.